

# **Lead Oxide (PbO) for Direct Conversion Detectors**

by

Oleksii Semeniuk

Faculty of Science & Environmental Studies

Lakehead University, Thunder Bay, Ontario

July 2017

A dissertation submitted in partial fulfillment  
of the requirements of the degree of Doctor of Philosophy  
Chemistry and Materials Science Program

Thunder Bay, Ontario, Canada 2017

Oleksii Semeniuk 2017 ©

# Lead Oxide (PbO) for Direct Conversion Detectors

Oleksii Semeniuk

Doctor of Philosophy, 2017

Chemistry and Materials Science Program

Lakehead University

## Abstract

There is great interest in the utilization of non-crystalline photoconductors for direct conversion medical X-ray imaging detectors. Lead Oxide (PbO) is one of the most promising candidates for application in general radiography and fluoroscopy since it possesses high theoretical X-ray-to-charge conversion gain and high X-ray stopping power due to the high  $Z$  of Pb ( $Z = 82$ ). A further advantage of PbO compared with other photoconductors (like polycrystalline layers of HgI<sub>2</sub>, PbI<sub>2</sub>, CZT) is the absence of heavy absorption edges up to 88 keV, which inherently offers higher spatial resolution. Therefore, PbO exhibits many of the requirements for an effective detector material. However, although very promising, poly-PbO layers are known to exhibit a relatively high dark current, an incomplete charge collection and a residual signal after the end of X-ray exposure, called signal *lag*. The reported lag was the main obstacle of this poly-PbO-based detector prototype, since this restricts applications to static imaging only and obscures the full potential of PbO in medical imaging. Another disadvantage is the high porosity of poly-PbO and its structural instability in air, which makes this material challenging for practical utilization in X-ray detectors.

To combat the above problems (i.e. lag, porosity and structural degradation in air) we have advanced PbO deposition technology and developed a novel type of *amorphous* lead oxide (a-PbO). The obtained a-PbO layers have near single-crystal bulk densities and are stable in air. In addition, the layers are capable of withstanding higher electric fields, while at the same time

exhibiting lower dark currents than previously achieved. Also, the temporal response and charge yield were significantly improved and compare favorably with published results on conventional films of polycrystalline PbO and even a-Se – the only photoconductor currently utilized in direct conversion detectors. Our measured X-ray response show almost complete elimination of signal lag to a level sufficient for the high-speed operations. Our advances in PbO technology allow us to utilize the full potential of PbO for medical X-ray imaging applications.

## Acknowledgements

I would like to express my sincere gratefulness to my supervisor Dr. Alla Reznik for her support and methodological guidance during my studies. Her inspiration and help over the last years encouraged me to pursue a doctor of philosophy degree at Lakehead University on the first place and pushed me to perform above my limits. In the time of a doubt, Dr. Reznik was always there to cheer me up and to remind me that only those who don't give up and continue to work patiently and rigorously achieve deserved success.

I am very grateful to Lakehead University for being a home for me and to my supervisory committee, Dr. Mark Gallagher and Dr. Dimiter Alexandrov who have been a blessing. Their doors were always opened for discussions and solving any questions, which made process of going through the graduate studies more comprehensible and pleasant.

I would also like to thank all members of Dr. Reznik group with special acknowledgment of Giovanni Decrescenzo and Sergey Reznik for helping and directing me with experiments and their interpretation. Their discussions on my project helped me to progress faster and more efficiently. I would also like to express my appreciation to Dr. John A. Rowlands, who maybe even not realizing it, had a great impact on me as a person and as a scientist. I cannot be grateful enough to Dr. Rowlands working with me from dawn till dusk and over the weekend-it was all my pleasure.

Also, I would like to thank a special person, who helped me a great deal in my research: Prof. Gytis Juska. His brilliant mind and years of experience provided invaluable input for PbO characterization. In addition, special thank you belongs to Dr. Kai Wang from Sun Yat-sen University, Miguel Pereira and Dino Deligiannis from Intlvac Inc. for their advices on deposition process and guidance on technology optimization.

Finally, I would like to thank my family for their love and support. You are the best! With such love and support that you give me – I believe everything is possible.

# List of figures

The scheme of a FPD .....	2
The indirect conversion scheme .....	3
Light dispersion in scintillators .....	4
Operation principle of the direct conversion detector .....	5
Spatial resolution for different detector thicknesses .....	5
Attenuation length as a function of X-ray energy .....	7
Crystal structure of $\alpha$ -PbO.....	26
Crystal structure of $\beta$ -PbO.....	27
The band diagram of single layer and the bulk of $\alpha$ -PbO .....	30
The electron density of states in conduction and valence bands of $\alpha$ -PbO .....	31
Density of states of $\alpha$ -PbO .....	32
Formation energy of Lead and Oxygen defects in poly-PbO.....	32
Cross section of the End-Hall ion source .....	40
TOF and CELIV signals in poly-PbO .....	53
Dependence of $t_{peak}$ on voltage ramp $A$ for different temperatures .....	58
Dependence of hole mobility on electric field for different temperatures .....	59
Dependence of the total current $i$ and the photocurrent $\Delta i$ on the delay time.....	60
Photogenerated carrier density as a function of delay time .....	61
The SEM picture of the grown PbO layer.....	66

Schematic representation of the TOF and photo-CELIV apparatuses .....	67
The scanning electron micrograph of the of the poly-PbO layer .....	78
Schematic representation of the photo-CELIV .....	80
Photo-CELIV signal corresponding to extraction of photo-generated charge carriers .....	81
Dependence of $t_{peak}$ on voltage ramp $A$ for different temperatures $T$ .....	83
Electron mobility as a function of electric field .....	83
Mobility of electrons as a function of inverse temperature .....	85
Schematic description of the conventional deposition process. ....	97
SEM of surface and cross-sectional views of the poly-PbO and a-PbO .....	100
Raman spectra of as deposited poly- and a-PbO .....	102
The XRD spectra of as-grown poly- and a-PbO films .....	104
XPS spectra of poly- and a-PbO .....	107
Typcal X-ray signal of poly-PbO. ....	121
Response of PbO detector to the modulated X-ray exposure at $F = 2 \text{ V}/\mu\text{m}$ .....	122
Influence of injection as a function of the chopper frequency $f$ for $F = 2 \text{ V}/\mu\text{m}$ .....	124
The lag as the function of a frame number.....	125
Pulse height spectrum measured with poly-PbO.....	127
$W_{\pm}$ as a function of $F$ in poly-PbO .....	128
The response of poly-PbO detector to subsequent 100 ms X-ray pulses .....	131
Schematic representation of the XPM apparatus .....	139

Schematic representation of the PbO-based pulse height spectrometer.....	139
Response of a-PbO at $F = 10 \text{ V}/\mu\text{m}$ to 4 s X-ray exposure.....	150
The lag of a-PbO for different X-ray pulses .....	152
The normalized response of a-PbO to 100 ms X-ray pulse.....	152
$W_{\pm}$ as a function of $F$ in a-PbO.....	153
Morphological analysis of a-PbO samples.....	156
Schematic diagram of experimental apparatus for X-ray performance evaluation.....	157

## List of tables

Table 2.1. Structure and properties of different lead oxides .....	23
Table 2.2. Theoretically predicted Raman phonon frequencies in $\text{Pb}_x\text{O}_y$ .....	26
Table 2.3. Overview of known PbO deposition techniques .....	34

## List of acronyms

FPD	Flat panel detector
LCAMD	Liquid crystal active matrix display
TFT	Thin film transistor
XRII	X-ray image intensifier
CsI	Cesium iodide
ehp	Electron-hole pair
PbI <sub>2</sub>	Lead iodide
HgI <sub>2</sub>	Mercuric iodide
CdTe	Cadmium telluride
CdZnTe	Cadmium zinc telluride
PbO	Lead oxide
Se	Selenium
Si	Silicon
XRD	X-ray diffraction
XPS	X-ray photoelectron spectroscopy
SEM	Scanning electron microscope
EDS	Energy dispersive X-ray spectroscopy
TOF	Time-of-flight
CELIV	Charge extraction by linearly increasing voltage
DOS	Density of states
SNMS	Secondary neutral mass spectrometry
MT	Multiple trapping

MTF

Modulation transfer function

NPS

Noise power spectrum

DQE

Detective quantum efficiency

# Table of contents

Abstract .....	ii
Acknowledgements .....	iv
List of figures .....	vi
List of tables .....	ix
List of acronyms .....	x
Chapter 1: Introduction .....	1
1.1. Flat panel detector technology for medical imaging applications .....	1
1.1.1. Indirect conversion scheme.....	2
1.1.2. Direct conversion scheme .....	4
1.2. Materials for direct conversion X-ray detectors .....	6
1.3. Previous utilization and challenges of lead oxide in modern medical imaging .....	10
Chapter 2: Lead Oxide as material of choice for direct conversion detectors .....	22
2.1. Introduction .....	22
2.2. Crystal structure and electronic properties of PbO.....	23
2.2.1. Crystal structure of tetragonal PbO ( $\alpha$ -PbO).....	25
2.2.2. Crystal structure of orthorhombic PbO ( $\beta$ -PbO) .....	27
2.2.3. Electronic properties of $\alpha$ - and $\beta$ -PbO.....	28
2.3. Deposition process of PbO layers.....	33
2.3.1. Selection of the PbO deposition technique .....	33

2.3.2. Background of PbO deposition .....	36
2.3.3. Principle of operation of the ion source .....	39
2.3.4. Calculation of the ion source parameters .....	40
Chapter 3: Charge transport in poly-PbO.....	47
3.1. Hole transport in poly-PbO.....	47
Charge transport mechanism in lead oxide revealed by CELIV technique.....	48
3. 2. Electron transport in poly-PbO.....	74
Transport of electrons in Lead Oxide studied by CELIV technique .....	75
Chapter 4: Investigation of structural properties of PbO layers.....	91
Ion-Assisted Deposition of Amorphous PbO Layers .....	92
Chapter 5: Investigation of X-ray performance of PbO.....	115
5.1. X-ray performance of poly-PbO.....	115
Characterization of polycrystalline lead oxide for application in direct conversion X-ray detectors.....	116
5.2. X-ray performance of a-PbO .....	146
Amorphous lead oxide (a-PbO): suppression of signal lag via engineering of the layer structure .....	147
Chapter 6: Conclusions and future work.....	164
6.1. Conclusions .....	164
6.2. Future work.....	166

6.2.1. Investigation of charge transport in a-PbO .....	166
6.2.2. Reduction of the dark current .....	167
6.2.3. Development of a-PbO detector prototype .....	167
References .....	168

# Chapter 1: Introduction

## 1.1. Flat panel detector technology for medical imaging applications

Direct conversion flat panel X-ray detectors (FPDs) are now widely used in various areas of digital X-ray imaging, including: security, astronomy and industrial imaging. However, their most important application is probably in medical imaging such as mammography, chest radiology, angiography, fluoroscopy, computed tomography, etc. Furthermore, FPDs allow for the merging of X-ray acquisition and magnetic resonance imaging for advanced medical diagnostics and treatment. Flat panel detectors uniquely offer rapid acquisition of high quality digital images of large area objects, i.e. the human body, and therefore are more advantageous compared with other types of X-ray sensors [1-3].

FPDs owe their success to advances in the liquid crystal active matrix displays (LCAMD), since they are based on the same technology. Indeed, similarly to LCAMD, FPD consists of a two-dimensional array of cells, called pixels, which contain a storage capacitor and a thin film transistor (TFT) (Fig. 1.1). However, additionally, each FPD pixel has an X-ray sensor element. Thus, the electronic signal is accumulated on the pixel capacitor, until the pixel is communicated via TFT. The TFT gate is connected to a certain address line, while the TFT source is connected to a particular data line. These address and data lines run through the whole detector, connecting pixels into an active matrix array. During operation, the gate lines are addressed one by one, setting TFTs into open position and thus facilitating the charge drainage from the storage capacitors via data lines.

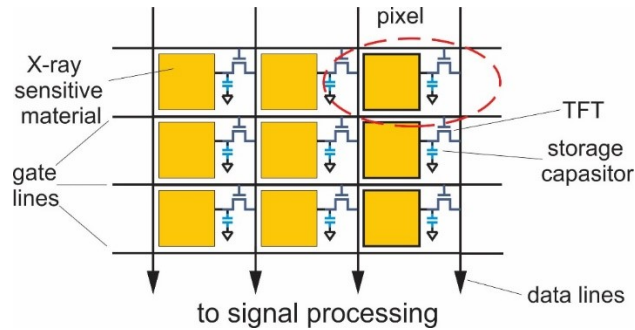


Figure 1.1. The scheme of a FPD is shown. Gate line connects the whole row of pixels, while each data line connects pixels along the same column. FPDs are designed in such a way that X-ray signal from the sensor element is stored in the pixel capacitor until it is addressed via the TFT.

Active matrices of integrated circuits are mass produced and commercially available in large sizes, therefore all that is required is a suitable way of converting X-rays into electric signal. Currently, there are two major approaches to this process, namely indirect and direct conversion, which will be discussed next.

### 1.1.1. Indirect conversion scheme

The majority of the state-of-the-art X-ray FPDs are based on *multi-step indirect* conversion. During the first conversion step, a phosphor layer, similar to that used in X-ray image intensifiers (XRII) (usually a Cesium Iodine (CsI) scintillator) converts X-ray quanta into optical photons. These photons diffuse through the phosphor until they are converted into electric charge by an array of Si photodiodes, which constitutes the second conversion step [4,5] (see Fig.1.2).

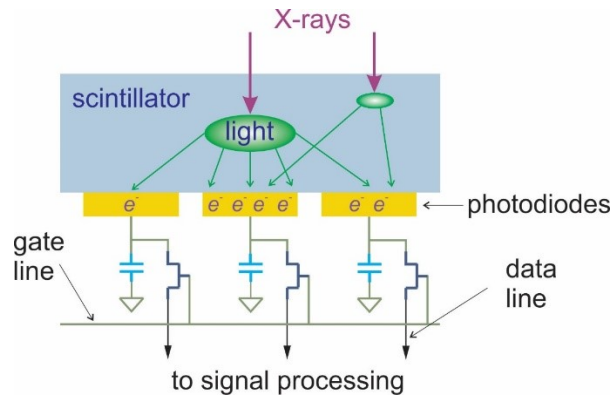


Figure 1.2: The indirect conversion scheme is shown. The absorbed X-rays generate light that disperses in a scintillator. An array of photodiodes is required to convert the light photons to electric signal.

CsI based detectors are compact and they have proven to be very successful for medical imaging (mammography, radiology and fluoroscopy). However, indirect FPDs possess an inherent disadvantage – a multi-step conversion process (i.e. X-rays to light and light to electric signal), which involves signal loss at every conversion step. This makes CsI detectors electronic noise rather than quantum noise limited, which results in compromised visibility of low contrast objects at the lowest exposure levels typically used in fluoroscopy (0.1 – 1  $\mu\text{R}/\text{frame}$ ) [6]. Another disadvantage of the indirect conversion approach is light dispersion inside of the scintillator, which reduces the spatial resolution of the detector. Indeed, once the scintillator converts an X-ray into light, this light starts to spread in all directions and will be co-registered by several neighboring pixels, instead of being registered by the one pixel above which X-ray was absorbed (Fig. 1.2). The sensitivity of the indirect conversion system is largely governed by the phosphor thickness: the thicker the phosphor – the more X-rays will be absorbed thus improving the quantum efficiency of the detector. However, higher X-ray sensitivity comes at the sacrifice of spatial resolution, as light spread becomes more pronounced (see Figs. 1.3 **a**, **b**). This issue can be addressed with the use of an alternative scintillator design, where the monolithic (uniform) structure of the scintillator is

replaced with pillar-like structures, shown in Fig. 1.3 c. This helps to improve spatial resolution, since light will be scattered from the pillar walls and therefore will be mostly contained within the column in which it was created. Utilization of structured scintillators allows one to double the thickness of phosphor layer (required for higher X-ray absorption), while maintaining the same spatial resolution as an unstructured scintillator of half the thickness. However, it was shown that even with pillar-like structures, significant light dispersion still occurs thus providing only partial improvement [7]. As a result, there is an inevitable tradeoff between X-ray absorption efficiency and spatial resolution. In addition, the complexity of the conversion process makes fabrication of indirect conversion detectors extraordinary expensive, and limits utilization to large hospitals. The above issues can be overcome by using a direct conversion scheme as discussed below.

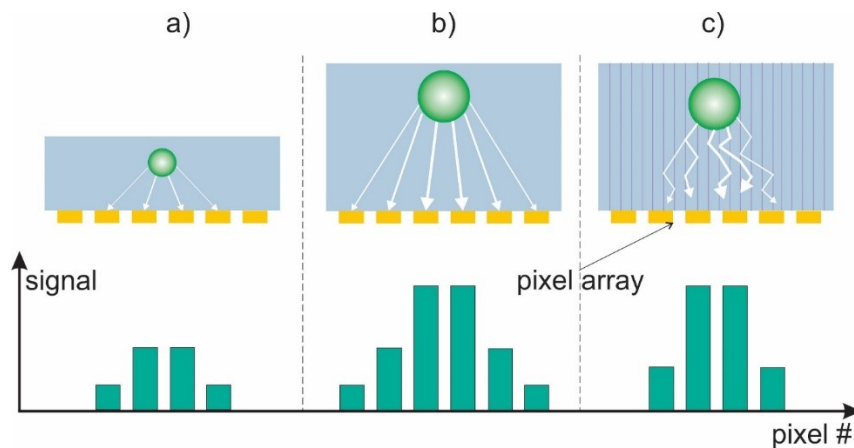


Figure 1.3: Light dispersion is shown for different scintillators. Spatial resolution inevitably degrades with the scintillator thickness.

### 1.1.2. Direct conversion scheme

In the direct conversion approach, a thick layer of a photoconductor is deposited directly onto an imaging matrix and acts as X-ray-to-charge transducer. X-rays are absorbed and generate a large number of electron hole pairs (ehp) within one conversion step. The created charge is then extracted from the photoconductor by an applied electric field (Fig.1.4). In this case the spatial resolution is

defined by the pixel size only and the thickness of the detector can be safely increased without the sacrifice of spatial resolution, since created charge is guided by the electric field (see Fig. 1.5). Moreover, by reducing the number of conversion steps, the sensitivity of the detector is defined by the amount of ehp generated by the X-ray photon and can be up to ten times more efficient than for a scintillator [8,9]. This makes the direct conversion scheme more sensitive at the lowest exposure rates, provided the right photoconductor is used.

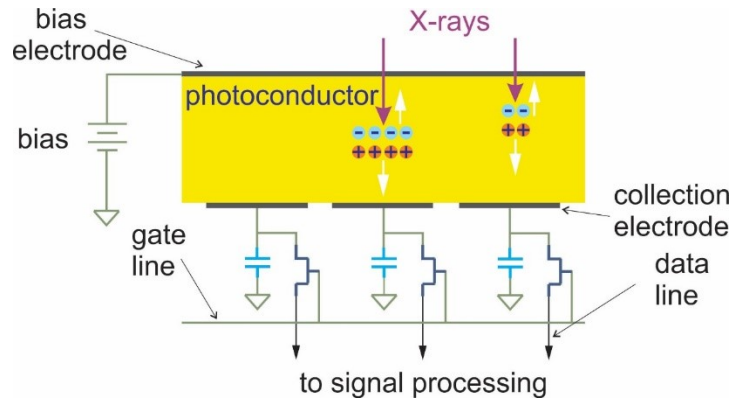


Figure 1.4: Scheme shows the operating principle of a direct conversion detector. When incident radiation is absorbed in the photoconductor, it generates charge carriers that move along the lines of an applied electric field.

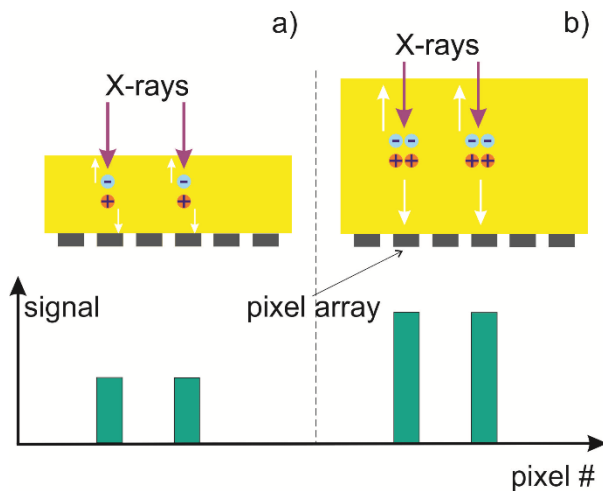


Figure 1.5: The spatial resolution for different detector thicknesses is shown. Direct conversion approach allows an increase in the detector thickness for higher X-ray sensitivity, without a sacrifice in spatial resolution.

## 1.2. Materials for direct conversion X-ray detectors

The ideal photoconductor for direct conversion X-ray imaging detectors should satisfy the requirements of the clinical application, which vary with procedure. However, listed below are the four most important properties of potential X-ray photoconductors:

- ❖ High absorption efficiency– to be able to stop X-rays efficiently to avoid unnecessary patient exposure;

- ❖ High X-ray-to-charge conversion gain is needed to generate as much signal as possible out of a single absorbed X-ray photon. X-ray-to-charge conversion efficiency is frequently expressed in terms of the average energy required to create a single electron-hole pair in the detector material,  $W_{\pm}$ ;

- ❖ Good photoconductive properties to ensure that the created image charge is efficiently collected on the electrodes and is not lost (via trapping or recombination) during transit through the layer;

- ❖ Compatibility with large area detector technology to allow direct deposition on the a-Si imaging matrix. Thus, the substrate temperature during deposition should not exceed 200-240 °C [10].

Currently, the only commercially viable X-ray photoconductor for direct conversion X-ray detectors is a-Se. a-Se detectors marketed by Analogic Canada utilize a 200  $\mu\text{m}$  thick layer of a-Se deposited directly on the active matrix of flat panel detectors with the 85  $\mu\text{m}$  pixel pitch and  $\sim 24\text{ cm} \times 30\text{ cm}$  field of view [11]. Such detectors normally operate under a constant electric field of 10 V/ $\mu\text{m}$  applied to the a-Se detector to collect the X-ray generated charge. a-Se properties perfectly fit the requirements of high dose, low energy ( $\sim 20\text{ keV}$ ) applications like those used in mammography [12]. Indeed, a-Se detectors offer high spatial resolution, primarily governed by

the pixel size [8]. In addition, in the mammographic energy range a-Se has adequate X-ray absorption as shown in Fig. 1.6, where the attenuation lengths,  $l$  of several materials (currently used or under active research for medical imaging applications) is plotted as a function of X-ray photon energy. Attenuation length is the thickness of material needed to absorb ~63% of incident radiation.

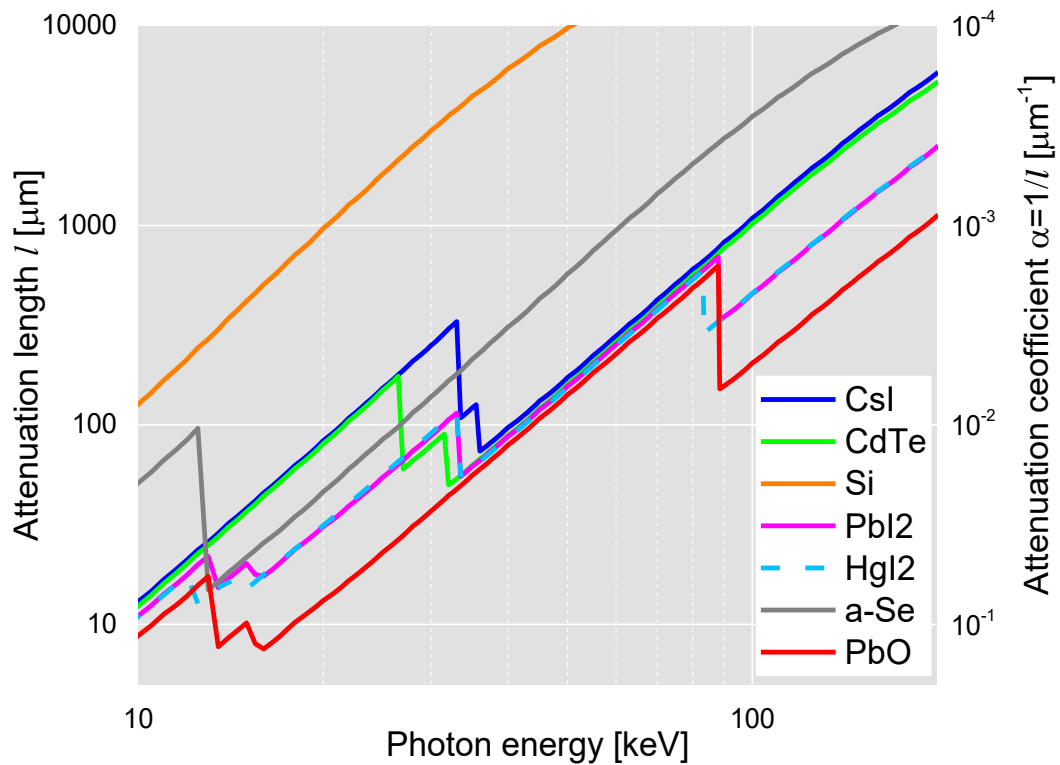


Figure 1.6. Attenuation length  $l$  is plotted as a function of X-ray energy.

As seen in Fig.1.6  $l$  depends the X-ray energy and in order to absorb most of the incident 20 keV radiation, ~ 50  $\mu\text{m}$  of a-Se is needed, while normally the thickness of the detector is tuned to absorb more than 90% of radiation. Since X-ray attenuation has an exponential dependence on material thickness ( $N_{abs} = N_{inc}(1 - e^{-d/l})$ , where  $N_{inc}$  is the number of incident and  $N_{abs}$  is

number of absorbed photons in the thickness  $d$  of material. 200  $\mu\text{m}$  a-Se layer absorbs  $\sim 98\%$  of incident X-rays, hence a-Se probably offers unbeatable performance for low energy applications, and demonstrates the enormous potential of direct conversion detectors for X-ray imaging.

Unfortunately, a-Se is a low atomic number ( $Z$ ) material which only has adequate attenuation for low energy X-rays, whereas the attenuation of X-rays in the diagnostic energy range ( $\sim 60\text{-}120$  kVp) is suboptimal. This is due to the fact that the attenuation depth is directly correlated to the X-ray energy  $\varepsilon$  ( $l \sim \varepsilon^n$ , where  $n \approx 3$ ) and inversely correlated with the atomic number ( $l \sim Z^{-m}$ , where  $m = 3 - 4$ ) [8] i.e. attenuation depth increases with increase of X-ray energy and decreases with increase of atomic number of material. Thus, 200  $\mu\text{m}$  of a-Se absorbs only  $\sim 60\%$  of incident X-rays at fluoroscopic energy ranges ( $\sim 60\text{-}70$  kVp), while CsI based detectors absorb  $\sim 90\%$  of the same energy X-rays. Therefore, for the higher X-ray energies, used in radiology and fluoroscopy, X-ray absorption of direct conversion detectors should be significantly improved. There are two ways to overcome this problem: deposit a thicker layer of a-Se or utilize an alternative high- $Z$  material with better X-ray absorption.

Numerous studies have indicated that 1 mm of a-Se is sufficient for adequate radiographic and fluoroscopic imaging [12,13]. Indeed, 1 mm of a-Se absorbs  $\sim 92\%$  of 70 kVp X-rays, thus providing efficient utilization of the exposure to the patient. However, since a-Se detectors are operated at  $10\text{ V}/\mu\text{m}$ , it requires a very high total applied voltage to the detector, which is risky for the TFT electronics [14]. In addition, a-Se possesses relatively low X-ray-to-charge conversion efficiency that depends on applied field. At  $10\text{ V}/\mu\text{m}$ , the  $W_{\pm} \approx 45\text{ eV}/\text{ehp}$  [15], which is comparable to CsI indirect conversion detectors [16]. As a result, at the lowest fluoroscopic doses a-Se direct FPDs suffer from the same problem as CsI indirect detectors: they are not quantum noise limited. Therefore, for high X-ray energy applications (radiography, fluoroscopy) a-Se has

to be replaced by a high- $Z$  material, which has higher X-ray sensitivity and can be used in smaller thicknesses. Since X-ray image detectors need to cover a large area, the use of single crystalline photoconductors in direct conversion detectors has to be ruled out, since it would be very expensive. Therefore, one has to concentrate on non-crystalline (amorphous and polycrystalline) modifications of high- $Z$  materials that can be directly deposited onto the imaging array and produce large area coatings.

In the last twenty years, several photoconductors have been investigated for applications in medical imaging, including polycrystalline layers of  $\text{PbI}_2$ ,  $\text{HgI}_2$ ,  $\text{CdTe}$ , and  $\text{PbO}$  [1,17]. As shown in Fig. 1.6 all these materials have a high attenuation coefficient (inverse of attenuation length  $l$ ), which indicates their superior X-ray sensitivity in comparison with a-Se. In addition, the theoretical conversion gain of these materials is 3-8 times higher than that of a-Se [17]. This suggests a potential for the quantum noise limited imaging performance at low exposures since the X-ray quantum noise can overcome the electronic noise. Polycrystalline lead oxide ( $\text{PbO}$ ) possesses a special place in this list due to absence of heavy absorption edges up to 89 keV (see Fig 1.6), which inherently offers higher spatial resolution (since this limits blurring from K-fluorescence). In addition,  $\text{PbO}$  was already successfully used for both optical and X-ray imaging. Indeed, in 1954, Philips manufactured the first lead oxide based vidicon tube, called the Plumbicon (after the Latin *plumbum* for lead) [18]. Plumbicons tubes were 2-3 cm in diameter, 19 cm long and utilized a relatively thin layer of  $\text{PbO}$   $\sim 20$   $\mu\text{m}$ , which was enough for the absorption of optical photons [19]. During operation, the  $\text{PbO}$  layer was typically biased to 1-2 V/ $\mu\text{m}$  [20]. Shortly afterwards, X-ray Plumbicons were also put into production. They were  $\sim 20$  cm in diameter and utilized a thicker 150  $\mu\text{m}$   $\text{PbO}$  layer, needed for adequate X-ray absorption [21], although it was shown that basic optical and X-ray images could be obtained with as little as 5  $\mu\text{m}$  of  $\text{PbO}$  [18].

Overall, commercial Plumbicons had rapid response and high-quality images were obtained even at low light or X-rays levels, due to the high sensitivity and good photoconductive properties of PbO. High performance Plumbicons defined their extensive (almost exclusive) utilization in many areas, including broadcasting, radiography, fluoroscopy and digital subtraction angiography in conjunction with image intensifiers [22-24]. Indeed, although thick PbO layers were feasible, at the time of this research, an electron beam read-out was used in vacuum tubes, which limited the coating area. Therefore, for large viewing area, optical Plumbicons were bundled with intensifier screens [22-24].

### **1.3. Previous utilization and challenges of lead oxide in modern medical imaging**

Recent advances with LCAMD gave a new spin on PbO technology and in 2004 researchers from Phillips, motivated by the success of PbO in Plumbicons, developed the first prototype of a PbO-based large area direct conversion flat panel detector [25,26]. For this, a 340  $\mu\text{m}$  layer poly-PbO was thermally evaporated in a molecular oxygen atmosphere onto a “cardio”-sized TFT substrate with an effective area of  $18 \times 20 \text{ cm}^2$  and a 184  $\mu\text{m}$  pixel pitch. Evaluation of the imaging performance of the PbO detector showed very encouraging results: charge yield was high enough for low dose imaging ( $W_{\pm} \approx 10 \text{ eV/ehp}$  was achieved at  $F = 3.5 \text{ V}/\mu\text{m}$ ), while the modulation transfer function (MTF) was limited only by the pixel size indicating very high spatial resolution [25,26]. The combination of high spatial resolution with comparatively low electron-hole pair creation energy (4 times lower than that of a-Se at lower electric field), and compatibility with large area detector technology makes PbO the most promising material for direct conversion detectors for a variety of both static (radiographic) and real time (fluoroscopic) applications.

Although poly-PbO has many of the requirements for an effective X-ray detector material, Philipps research group revealed the following issues with it:

1. Conventional poly-PbO layers, have a very peculiar structure: they consist of small platelets and possess a high porosity [25,26]. Thus, the density of as-grown poly-PbO layers is much lower than that of a crystalline material (up to 50 % of single crystal density). This significantly decreases the X-ray attenuation of the grown film – one of the major factors for PbO to be used in X-ray imaging.

2. Poly-PbO films are *unstable in air* and degrade in the ambient environment, making this material challenging for practical utilization in X-ray detectors.

3. The grown layers may be non-stoichiometric with depth-dependent oxygen deficiency [27]. The sites of oxygen voids might act as trapping and/or recombination centers for the X-ray generated charge, thus hindering performance of the detector [28].

4. PbO detectors exhibit a relatively *high dark current* that grows with applied electric field and at  $F = 3.5 \text{ V}/\mu\text{m}$  reaches  $\sim 250 \text{ pA}/\text{mm}^2$ , whereas for medical imaging applications, the detector dark current preferably should not exceed  $\sim 10\text{-}100 \text{ pA}/\text{mm}^2$  at operating bias [8]. The dark current was found to depend on the bias electrode material, which suggests that the dark current in poly-PbO is largely governed by a Schottky barrier formed at the PbO/metal contact interface, which sets an upper limit on the applied electric field [25,26,28].

5. In addition, while the X-ray to charge *conversion gain* of PbO, is theoretically higher than that of a-Se, it did not achieve theoretical predicted value ( $W_{\pm} \approx 6 \text{ eV}/\text{ehp}$ ). It should be noted that the charge yield was found to increase with applied electric field reaching value of  $\sim 100$  electrons per 1 keV of deposited X-ray energy (corresponds to  $W_{\pm} \approx 10 \text{ eV}/\text{ehp}$ ) at  $F = 3.5 \text{ V}/\mu\text{m}$ . Suboptimal values of charge yield and its dependence on applied field were linked to insufficient

carrier schubweg  $s$  – the mean carrier range, before it is trapped by deep traps or recombines. Schubweg is a product of carrier mobility  $\mu$ , lifetime  $\tau$  and electric field  $F$  i.e.  $s = \mu\tau F$ . For efficient charge collection, the carrier schubweg should be larger than the detector thickness, otherwise created carriers will be lost during their transit through the sample. However, it was shown that carrier schubweg in PbO is less than the photoconductor layer thickness in practical detectors. Indeed, from the dependence of charge yield on applied field, Simon et al. derived the  $\mu\tau$  product in poly-PbO to be  $4.4 \times 10^{-7} \text{ cm}^2/\text{V}$ . For such a  $\mu\tau$  value and maximal applied electric field  $F = 3.5 \text{ V}/\mu\text{m}$ , the carrier schubweg  $s = 154 \mu\text{m}$ , which is less than half the detector thickness  $d = 340 \mu\text{m}$ , resulting in suboptimal and depth dependent charge collection efficiency. Application of a higher electric field  $\sim 10 \text{ V}/\mu\text{m}$  could help to improve the charge yield, since the schubweg would be larger than the sample thickness however the range of  $F$  was limited to  $3.5 \text{ V}/\mu\text{m}$  [26], due to the dramatic increase of the dark current.

6. Finally, the poly-PbO detector exhibited *signal lag* – a residual current that continues to flow after X-ray exposure. The lag was found to depend a great deal on the material of the positively biased electrode: signal lag (and the shape of the X-ray response of PbO) was smaller when the positive electrode was made of aluminum (Al) rather than gold (Au). The material of the negatively biased electrode had a minimal effect on lag. In addition, lag was found to depend on applied electric field, decaying from 9 % to 4% in 1 s after termination of exposure for  $0.5$  and  $3.5 \text{ V}/\mu\text{m}$ , respectively. Such peculiar behavior was explained by the accumulation of X-ray generated electrons near Au electrode that triggers *injection* of holes from Au electrode into the PbO. After exposure, the accumulation layer dissolves and injection decreases as lag [26].

The presence of this residual signal has a detrimental effect on real time procedures, since part of the signal from previous exposures combines with the next one. The resulting image can be

inaccurate and misleading and, as such, might compromise the whole visualization advantage of real time (fluoroscopic) imaging. For practical fluoroscopic applications, the residual signal should promptly decay to <10% in less than 33 ms [12, 29-32]. Reported signal lag is probably the major constraint for the application of PbO in real time imaging and restricts its application to static imaging only (radiology). Thus, the full potential of PbO remains unexploited.

It should be noted that significant signal lag ( $\sim 70\%$  in 33 ms) and incomplete charge collection are common problems for other candidate materials for direct conversion detectors, like HgI<sub>2</sub>, PbI<sub>2</sub>, CZT or CdTe [33,34]. Similar to PbO these materials also have a polycrystalline layered structure, although different mechanisms were reported to be responsible for lag. In particular, *charge trapping* to deep traps on the grain boundaries of these materials, instead of injection as suggested for poly-PbO, was reported to be the dominant mechanism behind the signal lag [33,34]. Indeed, once X-ray generated charge carriers are trapped in defects or structural imperfections, they will not contribute to the signal and lead to incomplete charge collection. Eventually, these trapped carriers can be released later after the radiation is terminated resulting the transient decaying current, known as signal lag.

Another example is a-Se, for which small schubweg, incomplete charge collection and signal lag were also intrinsic at the early stages of its development [35]. In the case of a-Se, *charge trapping* was also reported to be the root cause of these problems. However, in contrast to the polycrystalline layers of HgI<sub>2</sub>, PbI<sub>2</sub> and CdTe mentioned earlier, a-Se has a uniform layer structure without grain boundaries, and charge trapping originates from the significant energy disorder in its electronic structure rather than from spatial disorder due to material inhomogeneity [36,37]. The signal lag in a-Se arises not as much from the release of the previously trapped charge itself (as in the case of HgI<sub>2</sub>, PbI<sub>2</sub> and CdTe), but rather from injection, triggered by this trapped charge. Indeed, multiple studies have indicated that X-ray generated charge carriers trapped at the a-Se/bias

electrode interface create an enhancement of the local electric field, which causes injection of charge carriers from the bias electrodes into the a-Se layer [38-41]. Overall, charge trapping can govern signal lag via several mechanisms including both the *release of previously trapped charge* or *injection*.

Initial approaches to improve PbO temporal performance focused on improvement of the layer stoichiometry (by means of layer deposition in various gas atmospheres) since it was suggested that oxygen vacancies in non-stoichiometric layers may act as deep trapping centers and cause signal lag (the problem of oxygen deficiency is well-known in oxides). However, efficacy of this approach was not confirmed [26,28,42,43]. This indicates that combating signal lag is a complex task which requires a comprehensive approach, including:

- (1) revealing the fundamental cause of the residual current;
- (2) development of the necessary deposition conditions, which will provide optimal material composition, free of the physical parameters causing lag.

Since presence of traps affects both signal duration and carrier transport (i.e. carrier mobility), the methodology used here is to study the lag mechanism through investigation of temperature and field dependencies of charge carrier mobility. This allows us to (1) characterize the effect of traps on carrier transport; (2) use the obtained knowledge on carrier transport to find a root cause for the lag and; (3) determine the fabrication-property relationship and apply established materials science concepts to obtain a lag-free material.

Interestingly, despite continuous interest in polycrystalline PbO since 1960's, the transport mechanisms in this material remain unknown. The only available data are on the mobility-lifetime product ( $\mu\tau$ ) in poly-PbO, which vary significantly. The wide scatter of the reported values is not surprising since the lifetime  $\tau$  depends on the carrier concentration, which makes evaluation of this parameter very sensitive to the measurement technique used. In contrast to the mobility-lifetime

product, the carrier drift mobility  $\mu$  is an objective parameter to evaluate transport in any semiconductor [44]. However, no direct measurements of carrier mobility in polycrystalline PbO have been reported. This is not surprising, since the time-of-flight (TOF) technique, which is the major tool for direct measurements of carrier mobility in low-mobility photoconductors [45] was determined to be inefficient [46] to study the transport properties in poly-PbO. The dispersive nature of charge transport [46,47] blurs a packet of photo-generated carriers so much that the transit time (the basis for the mobility measurement in the TOF technique) cannot be measured. Therefore, we have found an alternative experimental method for the investigation of charge transport in poly-PbO. This technique is Charge Extraction by Linearly Increasing Voltage (CELIV) [48]. CELIV is insensitive to the limitations of TOF and allows accurate investigation of the field and temperature dependence of charge carrier mobility in disordered materials. However, CELIV was never applied to measure the properties of materials with dispersive charge transport, like poly-PbO. To date, the theoretical support of the CELIV technique has been developed only for the case of a non-dispersive charge transport. Therefore, we have extended CELIV theory to account for dispersive charge transport, thus providing a theoretically substantiated technique for charge transport characterization in PbO and many other materials, for which standard techniques are not informative due to the peculiarities of charge transport.

The CELIV technique allowed us to measure electron and hole mobility in poly-PbO for the first time ever. This subject is described in detail in Chapter 3. As indicated in Chapter 3, electrons conduct electrical current in poly-PbO in a dispersive regime, in which the carrier mobility is time-dependent and therefore does not have a universal value that can be treated as a characteristic for the material. In addition, electron mobility was found to depend on both electric field and temperature with a relatively high activation energy ( $\sim 0.5$  eV), thus pointing to a multiple-trapping (MT) mechanism as responsible for transport of electrons in poly-PbO.

The established MT transport mechanism for electrons in poly-PbO is drastically different from the transport mechanism for holes in the same material as revealed in Chapter 3. While transport of holes also has a dispersive nature, the characteristic features of hole transport in poly-PbO are essentially temperature-independent. This means that the mobility dispersion for holes is not related to energy disorder, and rather is caused by spatial disorder in the material. Indeed, polycrystalline PbO layer is a porous network of separate single-crystal PbO platelets. It was suggested that the very unusual structural configuration of poly-PbO provides the spatial inhomogeneity responsible for the unusual hole transport. This finding suggests a new direction towards the optimization of PbO technology that had previously focused on the improvement of the layer stoichiometry to increase mobility and  $\mu\tau$ : the PbO layer structure must be modified to eliminate spatial inhomogeneities by amorphization of the PbO structure. This objective was successfully achieved by advancing conventional PbO fabrication technology with ion assisted deposition – a well-established technique for addressing issues related to the layer structure. Our advancement of the deposition process, described in Chapter 4, resulted in a new polymorphic form of the grown material, namely, amorphous Lead Oxide (a-PbO), which was not synthesized before [49]. In contrast to poly-PbO, a-PbO is uniform, free of voids and possesses a significantly higher packing density, compared with poly-PbO. In addition, a-PbO layers possess perfect structural stoichiometry without oxygen vacancies, which are prone to its polycrystalline counterpart.

Moreover, the ion assisted deposition process also resulted in dramatic lag suppression in a-PbO. Investigation of the X-ray performance of poly-and a-PbO layers, elaborated in Chapter 5, revealed the superior temporal performance of the a-PbO layers over poly-PbO. The obtained values of residual signal were found to compare favorably to those obtained on a-Se direct conversion, and even to CsI indirect conversion detectors, which are currently used for fluoroscopic imaging. Chapter 5 also contains an investigation of the charge creation energy  $W_{\pm}$  in a-PbO which

was found to be less than half that in a-Se photoconductors, thus offering superior X-ray sensitivity for a-PbO-based detectors. Such X-ray performance in combination with recent advances in structural properties, make amorphous PbO a serious candidate for practical radiographic and fluoroscopic detectors.

Before proceeding to experimental sections (Chapters 3-5), a literature overview of the data available on the crystal and electronic structure of PbO will be elaborated in Chapter 2, in order to provide a reader with the solid background knowledge, required to undertake this study.

## References

1. Kasap, S. et al. Amorphous and polycrystalline photoconductors for direct conversion flat panel X-ray image sensors. *Sensors* **11**, 5112–5157 (2011).
2. Semeniuk, O. et al. Characterization of polycrystalline lead oxide for application in direct conversion X-ray detectors. Submitted to *Sci. Rep.*
3. Fahrig, R. et al. Design, performance, and applications of a hybrid X-Ray/MR system for interventional guidance. *Proc. IEEE*. **96**, 468–480 (2008).
4. Granfors, P. R. et al. Performance of a flat panel cardiac detector. 2001, *Proc. SPIE*. **4320**, 77–86 (2001).
5. Busse, F. et al. Design and performance of a high-quality cardiac flat detector. *Proc SPIE*. **4682**, 819–827 (2002).
6. Seibert, J. A. Flat-panel detectors: how much better are they? *Pediatr Radiol*. **36**, 173–181 (2006).
7. Zhao, W., Ristic, G. & Rowlands, J. A. X-ray imaging performance of structured cesium iodide scintillators. *Med. Phys.* **31**, 2594 (2004).
8. Kasap, S. & Rowlands, J.A. Direct-conversion flat-panel X-ray image sensors for digital radiography. *Proc. IEEE*. **90**, 591-604 (2002).

9. Chabbal, J. et al. Amorphous silicon x-ray image sensor. *SPIE Proc.* **2708**, 499-510 (1996).
10. Zentai, G. Photoconductor-based (direct) large-area x-ray imagers. *JSID.* **17**, 543-550 (2009).
11. Hu, Y. H. & Zhao, W. The effect of amorphous selenium detector thickness on dual-energy digital breast imaging. *Med. Phys.* **41**, 111904 (2014).
12. Tousignant, O. et al. Spatial and temporal image characteristics of real time large area a-Se X-ray detector. *Proc. SPIE.* **5745**, 207-215 (2005).
13. S. Marcovici, Amorphous selenium based X-ray detectors. *Proc. ISA/IEEE Sensors for Industry Conference.* 193-196 (2001).
14. D. Pacella. Energy-resolved X-ray detectors: the future of diagnostic imaging. *RMI*, **8**, 1-13 (2014).
15. Blevis, I. M., Hunt, D. C. & Rowlands, J. A. Measurement of x-ray photogeneration in amorphous selenium. *J. Appl. Phys.* **85**, 7958-7963 (1999).
16. Beutel, J., Kundel, H. L. & Van Metter, R. L. *Handbook of medical imaging* Vol.1 (eds Rowlands, J. A., Yorkstone, J.) Ch. 4, 223-328 (SPIE, 2000).
17. Kabir, M., Kasap, S. & Rowlands, J. A. (2006) Photoconductors for x-ray image detectors. In: Kasap S, Capper P (eds) Springer Handbook of Electronic and Phonic Materials. Springer, New York, pp. 1125-1126
18. Heijne, L., Schagen, P. & Bruining, H. Television pick-up tube for both light and X-Ray pictures. *Nat.* **173**, 220 (1954).
19. Biberman, L. M. & Nudelman, S. *Photoelectronic imaging devices* Vol. 2 (eds Stupp, E. H., Levitt, R. S.) Ch. 14, 275-300 (Plenum, 1971).
20. Haan, E. F., Van der Drift, A. & Schampers, P. P. M. The "Plumbicon", a new television camera tube. *Philips Tech. Rev.* **25**, 133-180 (1964).

21. Jacobs, J. & Berger, H. Large-area photoconductive X-Ray pickup-tube performance. *Electr. Eng.* **75**, 158-161 (1956).
22. Van Lysel, M. S. Limitations of the lead oxide vidicon for dual-energy digital subtraction angiography. *IEEE Trans. Med. Imaging.* **10**, 530-537 (1991).
23. Kruger, R. A. et al. Real-Time Computerized Fluoroscopy and Radiography—A Progress Report. *Real-Time Radiologic Imaging: Medical and Industrial Applications.* **STP716**, 303-314 (1980).
24. Van Lysel, M. S. et al. Left ventricular dual-energy digital subtraction angiography: a motion immune digital subtraction technique. *Int. J. Cardiac. Imag.* **7**, 55-65 (1991).
25. Simon, M. et al. PbO as direct conversion x-ray detector material. *Proc. SPIE* **5368**, 188-199 (2004).
26. Simon, M. et al. Analysis of lead oxide (PbO) layers for direct conversion x-ray detection. *IEEE Trans. Nucl. Sci.* **52**, 2035-2040 (2005).
27. Semeniuk, O., Csik, A., Kokenyesi, S. & Reznik, A. Ion-assisted deposition of amorphous PbO layers. *J. Mater. Sci.* **52**, 7937-7946 (2017).
28. Berashevich, J., Semeniuk, O., Rubel, O., Rowlands, J. A. & Reznik, A. Lead monoxide a-PbO: electronic properties and point defect formation. *J. Phys.: Condens. Matter.* **25**, 075803 (2003).
29. Tsukamoto, A. et al. Development and evaluation of a large-area selenium-based flat-panel detector for real-time radiography and fluoroscopy. *Proc. SPIE.* **3659**, 14-23 (1999).
30. Tsukamoto, A. et al. Development of a selenium-based flat-panel detector for real-time radiography and fluoroscopy. *Proc. SPIE.* **3336**, 388-395 (1998).
31. Adachi, S. et al. Experimental evaluation of a-Se and CdTe flat-panel x-ray detectors for digital radiography and fluoroscopy. *Proc. SPIE.* **3977**, 38-47 (2000).

32. Hunt, D. C., Tuosignant, O. & Rowlands, J. A. Evaluation of the imaging properties of an amorphous selenium-based flat panel detector for digital fluoroscopy. *Med. Phys.* **31**, 1166-1175 (2004).
33. Zentai, G. et al. Comparison of mercuric iodide and lead iodide X-ray detectors for X-ray imaging applications. *IEEE Trans. Nucl. Sci.* **53**, 2506–2512 (2006).
34. Tokuda, S., Kishihara, H., Adachi, S. & Sato, T. Improvement of the temporal response and output uniformity of polycrystalline CdZnTe films for high-sensitivity X-ray imaging. *SPIE Proc.* **5030**, 861-870 (2003).
35. Kasap, S. et al. Amorphous selenium and its alloys from early xeroradiography to high resolution x-ray image detectors and ultrasensitive imaging tubes. *Phys. Status Solidi B* **246**, 1794-1805 (2009).
36. Mott, N. F. & Davis, E. A. *Electronic processes in non-crystalline materials* Ch. 6, 199-319 (Clarendon, 1979).
37. Baranovskii, S. D. & Rubel, O. *Charge Transport in Disordered Solids with Applications in Electronics* (ed. Baranovskii, S. D.) Ch. 2, 49-96 (John Wiley & Sons, 2006).
38. Zhao, B. & Zhao, W. Temporal performance of amorphous selenium mammography detectors. *Med. Phys.* **32**, 128-136 (2005).
39. Abbaszadeh, S. et al. Characterization of lag signal in amorphous selenium detectors. *IEEE Trans.* **63**, 704 – 709 (2016).
40. Abbaszadeh, S., Scott, C. C., Bubon, O., Reznik, A. & Karim, S. K. Enhanced detection efficiency of direct conversion x-ray detector using polyimide as hole-blocking layer. *Sci. Rep.* **3**, 3360 (2013).

41. Zhao, W., Decrescenzo, G. & Rowlands J. A. Investigation of lag and ghosting in amorphous selenium flat-panel x-ray detectors. *Proc. SPIE* **4682**, 9-20 (2002).
42. Simon, M., Wiechert, D. U., Feldmann, C. Lead oxide based photosensitive device and its manufacturing method. US Patent 7649179 B2 (2005).
43. Damon, R. W., Eshbach, J. R. Photoconductor of lead oxide and method of making. US 2888370 A (1956).
44. Privrikas, A., Philippa, B., White, R. D. & Juska, G. Photocarrier lifetime and recombination losses in photovoltaic systems. *Nature Photonics* **10**, 282-283 (2016).
45. Haber, K. S. & Albrecht, A. C. Time-of-flight technique for mobility measurements in the condensed phase. *J. Phys. Chem.* **88**, 6025-6030 (1984).
46. Semeniuk, O. et al. Charge transport mechanism in lead oxide revealed by CELIV technique. *Sci. Rep.* **6**, 33359 (2016).
47. Semeniuk, O. et al. Transport of electrons in lead oxide studied by CELIV technique. *J. Phys. D: Appl. Phys.* **50**, 035103 (2017).
48. Juska, G., Arlauskas, K. & Viliunas, M. Extraction Current Transients: New Method of Study of Charge Transport in Microcrystalline Silicon. *Phys. Rev. Lett.* **84**, 4946-4949 (2000).
49. Semeniuk, O., Sukhovatkin, V. & Reznik, A. Amorphous lead oxide based energy detection devices and methods of manufacture thereof. US Patent Application No. 15/427,247. Filed on February 7, 2017.

# Chapter 2: Lead Oxide as material of choice for direct conversion detectors

This chapter is devoted to the crystal structure and polymorphism of PbO. We will start from a literature review on the properties of different oxides of lead, followed by the scope of the experimental techniques that are used to study different crystal configurations of PbO. This information will provide a baseline for our research and will be used as a reference for characterization of our own samples.

## 2.1. Introduction

There exist a large number of possible oxides of lead (for instance PbO, PbO<sub>2</sub>, Pb<sub>2</sub>O<sub>3</sub>, Pb<sub>3</sub>O<sub>4</sub>, etc.) which can exist in more than 15 different crystal forms [ [1] and Ref. 13 within]. Such variety of lead oxides is possible due to the peculiarity of lead to have two valence states: a higher valence state of +4 (as expected for a group 14 element of the periodic table) and a lower valence state of +2 (due to stability of so called inert lone pair of 6s<sup>2</sup> electrons) [2,3]. Each oxide has its own rich color, which resulted in their wide utilization as paint pigments in ancient times. Table 2.1 represents the physical properties of selected configurations of lead oxides, which are most frequently encountered in nature.

It is worth mentioning one lead compound that is not listed in Table 2.1, called Hydro Cerussite (2PbCO<sub>3</sub>·Pb(OH)<sub>2</sub>). This material is frequently referred as a '*white lead*', because it was used to obtain the white color in paints. In nature, it forms from PbO in the presence of CO<sub>2</sub> and H<sub>2</sub>O molecules. This transformation occurs naturally even at ambient conditions. If this transformation occurs in a PbO layer employed in a practical direct conversion X-ray detector, the detector performance will degrade, as a result of an increased dark current and deteriorated X-ray response.

Storage of poly-PbO samples in vacuum or under a protective atmosphere of inert gas, such as nitrogen or argon prevents PbO from degradation. To avoid degradation, it is clear that a sealing technology still needs to be developed for practical material utilization [4,5].

Table 2.1. Structure and properties of different lead oxides [6].

Chemical formula	Name	Crystal structure	Color	Band gap [eV]
PbO	litharge	tetragonal	red	1.9
PbO	massicot	orthorhombic	yellow	2.7
PbO <sub>2</sub>	$\beta$ -plattnerite	tetragonal (rutile)	dark brown	1.5
PbO <sub>2</sub>	$\alpha$ -scrutinyite, PbO <sub>2</sub> -II	orthorhombic	dark reddish	1.4
Pb <sub>2</sub> O <sub>3</sub>	Pb sesquioxide	monoclinic	black	1.4
Pb <sub>3</sub> O <sub>4</sub>	minium	tetragonal	bright red	2.1
Pb <sub>12</sub> O <sub>19</sub>		monoclinic	dark brown/black	1.28

Out of the great number of possible oxides, only the monoxide of lead (PbO) was previously utilized in detector applications [4,7-10] and therefore will be discussed in details next.

## 2.2. Crystal structure and electronic properties of PbO

Lead monoxide exists in two polymorphic forms: a red tetragonal  $\alpha$ - modification and a yellow orthorhombic  $\beta$ -form. In the literature, these two forms of PbO are frequently called litharge and massicot, respectively.  $\alpha$ -PbO is stable at room temperature and  $\beta$ -PbO is stable above 490 °C [2]. Even though  $\beta$ -PbO is metastable with respect to  $\alpha$ -PbO at ambient conditions, the phase transformation from  $\beta$ - to  $\alpha$ - PbO is very slow and it can take tens of years at room temperature, however small stress can facilitate a prompt transformation. At the same time, transformation of tetragonal material into orthorhombic also has a very peculiar behavior and depends on the size

and quality of the PbO crystallites. Practically, it was found that oxygen deficit (or lead excess) during sample fabrication, decreases the  $\alpha$ - to  $\beta$ -PbO transition temperature to as low as  $\sim 350$  °C [11]. On the other hand, large single crystals of high quality  $\alpha$ -PbO were reported to persist well above the nominal transition temperature and even up to 600-700°C [11,12].

Thermally evaporated poly-PbO layers are composed of both phases: the layer growth starts with a *seeding* layer of yellow orthorhombic PbO, while the *bulk* of the layer is dominated by red tetragonal lead oxide [10]. The thickness of the orthorhombic seeding layer depends on the deposition parameters, such as deposition rate and substrate temperature. Higher deposition rates and lower substrate temperature facilitate the growth of the orthorhombic phase [4,8,10]. Such interesting dependence of material composition and the abundance of the high temperature phase at the beginning of the layer was linked to peculiarities of the deposition process and in particular to the supercooling effect of evaporated PbO particles [10,13]. Indeed, during the deposition process, the source temperature is very hot ( $\sim 1000$  °C) in comparison to the substrate temperature ( $\sim 100$  °C). Upon arrival at the substrate, condensing PbO particles will tend to transition from the high temperature orthorhombic to the low temperature tetragonal phase. However, the first deposited layers will experience rapid cooling. They will not have enough time to reach a state of thermodynamic equilibrium, i.e. tetragonal (defined by the substrate temperature) and will be frozen into the high temperature orthorhombic phase. However, once the seeding layer is formed, it decreases the temperature exchange between the hot condensing atoms and the cold substrate. This decreases the cooling rate and the arriving atoms have more time to reach the equilibrium low temperature tetragonal phase. Similar structural variations with thickness were observed on other materials, for instance Zirconia. Very thin zirconia layers have a high-temperature cubic structure, but after  $\sim 600$  nm, a low-temperature monoclinic crystal structure starts dominating the layer. In

both cases (PbO and Zirconia) this behavior can be explained by a reduced thermal conductivity in the thicker films. This results in a lower cooling rate, thus providing more time to reach the thermal equilibrium structure, appropriate to the substrate temperature [10,14].

At the beginning of research on Plumbicons, the orthorhombic phase of PbO was more desirable over the tetragonal one [15,16], while in relatively recent studies, Simon and colleagues suggested that the presence of an orthorhombic phase is undesirable since it might diminish detector performance [7,10]. Since optimal detector composition has not been unambiguously established yet, in the next section we will briefly review the crystal structure and electronic properties of both phases.

### *2.2.1. Crystal structure of tetragonal PbO ( $\alpha$ -PbO)*

$\alpha$ -PbO has a layered structure, with the layers parallel to  $ab$  plane (Fig. 2.1). The distance between lead atoms in adjacent planes is 0.386 nm, which is 10 % larger than the Pb-Pb distance of 0.35 nm in elemental lead. The atomic arrangement in the lattice looks like a square pyramid with oxygen atoms forming the base and a Pb atom at the apex, with Pb-O distances of 0.237 nm. At the same time, oxygen is bound to four equivalent Pb atoms, thus forming a tetrahedron, with O in the center. At room temperature, the axes of the unit cell are  $a = b = 0.3974$  nm and  $c = 0.5021$  nm with a  $129 P4/nmm$  space group [2] (see Fig. 2.1). The planar symmetry of the  $\alpha$ -PbO layers has been well characterized by X-ray diffraction (XRD). A XRD histogram of poly-PbO contains more than 20 peaks, out of which there are only 4 peaks with intensities of more than 20%. The strongest peak is at  $2\theta = 28.82^\circ$ , corresponding to the  $hkl$  line of the (011) plane and three smaller peaks at  $2\theta = 32.04^\circ$ ,  $48.93^\circ$ ,  $55.15^\circ$ , corresponding to the (110), (112) and (121) planes respectively. The relative intensity of most of the other peaks is not higher than 10% [17]. The

phonon frequencies of  $\alpha$ -PbO are evident in Raman spectroscopy by four peaks, listed in Table 2.2, which shows the Raman modes for the most frequently encountered oxides. The most intense peak is located at  $145\text{ cm}^{-1}$ , while the peak at  $306.4\text{ cm}^{-1}$  was not observed in the experimental spectra [10,18,19].

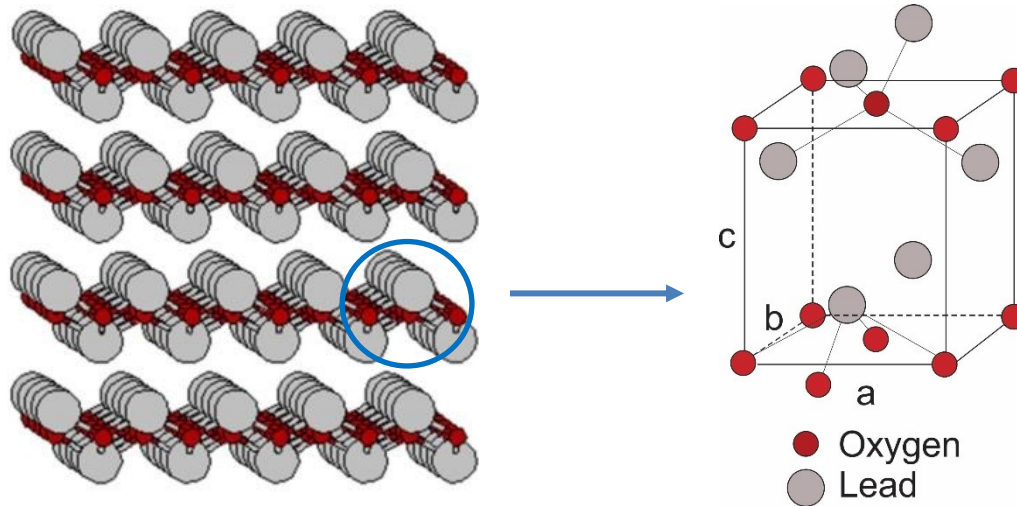


Figure 2.1. Crystal structure of  $\alpha$ -PbO. Data has been reproduced from Fig. 1 of Ref. [2] (right) and Ref. [20] (left).

Table 2.2. Theoretically predicted Raman phonon frequencies in  $\text{Pb}_x\text{O}_y$ .

Material	Crystal structure	Theoretically predicted frequency
$\alpha$ -PbO [18]	Tetragonal	80.1// 144.8// 306.4// 338.5
$\beta$ -PbO [18]	Orthorhombic	57// 71// 89// 91// 147// 167// 216// 217// 255// 288// 345// 390
PbO <sub>2</sub> [21]	Tetragonal (rutile)	222// 331// 390// 510// 648.5// 735.5
PbO <sub>2</sub> [22]	Orthorhombic	165// 226// 363// 430// 512.5// 619// 1239
Pb <sub>3</sub> O <sub>4</sub> [23,24]	Tetragonal	122// 149// 223// 313// 340// 390// 480// 548

### 2.2.2. Crystal structure of orthorhombic PbO ( $\beta$ -PbO)

$\beta$ -PbO also has a layered structure, but unlike  $\alpha$ -PbO (see Fig. 2.2): the layers are parallel to  $cb$  plane and the Pb-O bonds look like zigzag chains with distances of 0.2221 nm and 0.2249 nm within the chain and  $2 \times 0.2481$  nm between the chains. At 300 K, the lattice parameters are  $a = 0.58931$  nm,  $b = 0.47528$  nm and  $c = 0.54904$  nm with the  $57$  Pbcm space group. The distance between lead atoms in adjacent layers is 0.3977 nm, which is larger than in  $\alpha$ -phase [2].

The XRD spectrum of  $\beta$ -PbO is dominated by  $2\theta = 29.03^\circ$ , corresponding to  $hkl$  line of the (111) planes, and three smaller peaks at  $2\theta = 30.32^\circ$ ,  $32.6^\circ$ ,  $53.073^\circ$ , corresponding to (200), (020) and (311) planes, respectively. The relative intensity of most of the other peaks is not higher than 10%. The location of the peaks and their relative intensities are very close to  $\alpha$ -PbO, however they are separated enough to be distinguishable during spectrum processing [25].

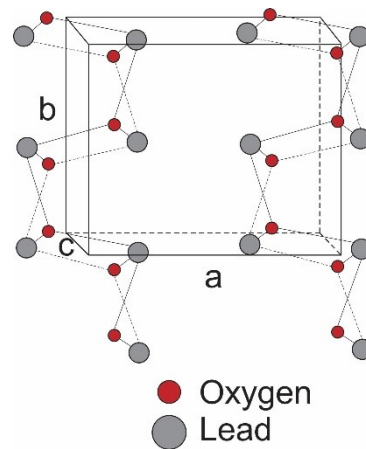


Fig. 2.2. Crystal structure of  $\beta$ -PbO. Data has been reproduced from Fig. 2 of Ref. [2].

The Raman spectrum of  $\beta$ -PbO contains overall 12 peaks (see Table 2.2).  $\beta$ -PbO has a greater number of phonon modes than  $\alpha$ -phase due to the lower symmetry of the  $\beta$ - phase (the higher the symmetry the lower number of vibrational modes). The most intense Raman peak observed

experimentally on a powder sample appears at  $143\text{ cm}^{-1}$  while another 5 peaks were observed at  $52.5, 71.5, 87.5, 289.5$  and  $384.5\text{ cm}^{-1}$ . Therefore, the most intense and narrow Raman peak of  $\beta$ -PbO at  $143\text{ cm}^{-1}$  is very close to  $\alpha$ -PbO peak at  $145.5\text{ cm}^{-1}$  and usually these two peaks merge into a single one, making it difficult to recognize the phase [10]. On the other hand, Raman peaks at  $288\text{ cm}^{-1}$  for the orthorhombic and at  $338\text{ cm}^{-1}$  for tetragonal PbO are well separated and can be clearly differentiated from the Raman spectrum. Therefore, their ratio of intensities  $I_{\beta/\alpha} = \frac{I_{\beta(288)}}{I_{\alpha(338)}}$  is used to perform the qualitative analysis of the grown films. This ratio is not constant and changes with the depth profile: the initial, seeding layer, is reported to be composed mostly of the orthorhombic phase with an intensity ratio  $I_{\beta/\alpha} \approx 0.8-2$ . After the seed layer is formed, the concentration of orthorhombic phase decreases towards the free surface of the sample, where tetragonal phase becomes dominant with  $I_{\beta/\alpha} = 0.1 - 0.5$  [10].

### 2.2.3. Electronic properties of $\alpha$ - and $\beta$ -PbO

$\alpha$ -PbO and  $\beta$ -PbO are indirect band gap semiconductors with band gap energies of 1.9 and 2.7 eV for  $\alpha$ -PbO and  $\beta$ -PbO, respectively. Several researchers have measured the binding energies of the Pb  $4f_{7/2}$  and O 1s electrons with X-ray photoelectron spectroscopy. The obtained values were found to differ slightly, depending on the supplier of the PbO. Terpstra et al. reported Pb  $4f_{7/2}$ /O 1s energies to be 138.6 eV/529.7 eV and 138.2 eV/529.4 eV for  $\alpha$ -PbO and  $\beta$ -PbO, respectively [2]. Kim et al. reported almost the same energies for the two phases: 137.9eV/527.8 eV for  $\alpha$ -PbO and 137.9eV/527.7 eV for  $\beta$ -PbO [26]. Dai and Xu reported values of 137.4eV for the Pb  $4f_{7/2}$  peak and 530.3 eV for the O 1s, although the phase of PbO was not specified [27].

In both materials, the bands are formed in very similar way: the valence bands are mainly formed as a result of hybridization of the O: $2p$  and Pb: $6p$  states, while its bottom is formed by

mixing of O:2*p* and Pb:6*s* electrons [2]. Within the same  $\alpha$ -PbO layer, the atoms are bonded by strong covalent bonds, while the interlayer interaction formed by the overlap of the Pb:6*s* electrons [2] is very weak: 0.013eV/atom, which is lower than the graphite interlayer interaction of 0.052 eV/atom [28]. Although  $\alpha$ -PbO layers are held together by relatively weak forces, they do significantly affect the band diagram of the bulk material and are responsible for the distinct anisotropy of the electronic properties of electrons and holes (see Fig. 2.3) [20]. Indeed, as shown in Fig. 2.3 the interaction between separate PbO layers converts  $\alpha$ -PbO from a direct band gap semiconductor with the band gap of  $\sim 2.44$  eV into an indirect band gap semiconductor with band gap of  $\sim 1.8$  eV. Furthermore, it helps disperse the top of the valence band, while the bottom of the conduction band is well dispersed in both cases. Since band dispersion is related to carrier effective mass, the relatively flat valence band at the  $\Gamma$  point suggests the presence of the heavy holes, while the dispersed conduction band suggests a low effective mass for electrons.

Thus, Berashevich et al. reported hole ( $m_h^*$ ) and electron ( $m_e^*$ ) effective masses in a single  $\alpha$ -PbO layer to be  $38 m_0$  and  $0.46m_0$ , respectively (where  $m_0$  is free electron rest mass). Stacking layers together reduces the effective mass of the carriers (especially for holes) and makes their values anisotropic, i.e. the hole effective mass along the *ab* plane (see Fig. 2.1) was found to be  $m_{h(a)}^* = m_{h(b)}^* = 5.91m_0$  and out-of-plane  $m_{h(c)}^* = 1.12m_0$ . The electron effective mass is less anisotropic:  $m_{e(a)}^* = m_{e(b)}^* = 0.41m_0$  and out-of-plane  $m_{e(c)}^* = 0.47m_0$  [20].

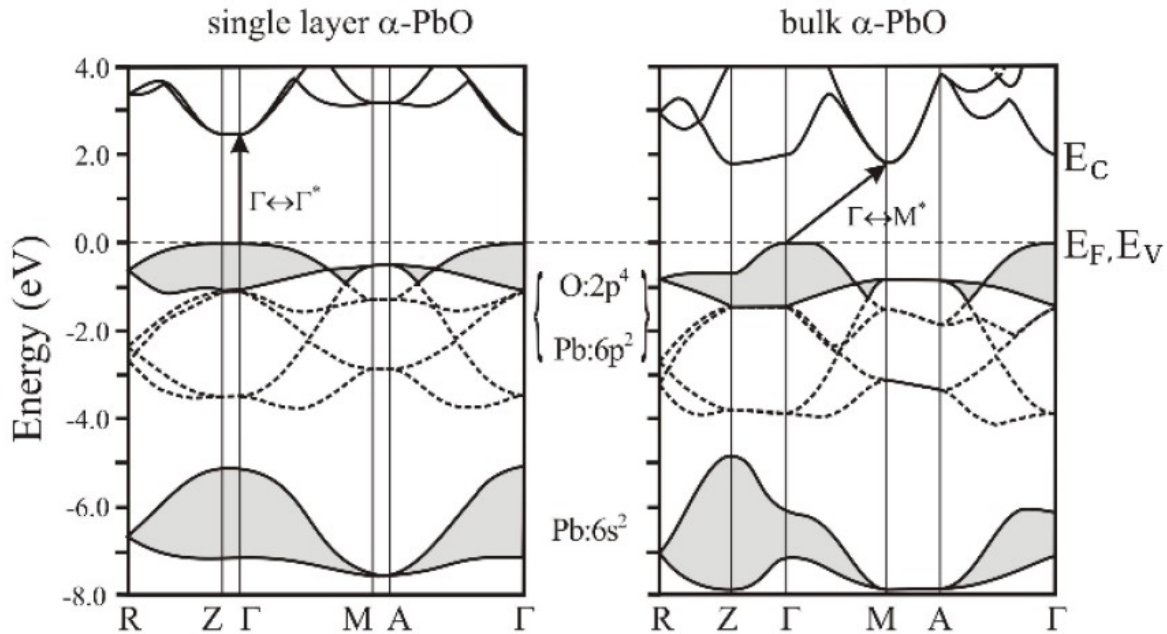


Figure 2.3. The band diagram of single layer and the bulk of  $\alpha$ -PbO is shown. The solid lines are used for the bands significantly affected by the interlayer interactions. The shaded areas are applied to highlight the band splitting. The Fermi energy  $E_F$  is referred to the top of the valence band. Arrows indicate the lowest-energy inter-band transitions for which “\*” in the symmetry point notation denotes the conduction band. The figure and captions were taken from Ref. [20].

The heavy holes were shown to be a reflection of the strong localization of the electron density on the oxygen atoms. Such electron localization was linked to the domination of lone pair O:2p electrons at the  $\Gamma$ -point, as strong localization is a feature of the lone pair electrons. In contrast, the electron density in the conduction band was found to be delocalized, forming a continuous “channel” between the atoms (see Fig. 2.4). Since the carrier mobility is inversely correlated to the effective mass, electrons are expected to have a larger microscopic mobility than that of holes [20].

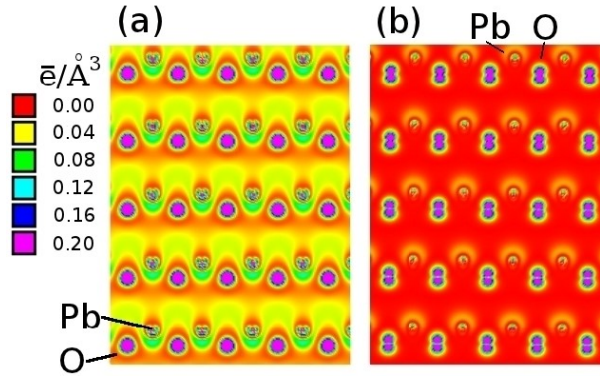


Figure 2.4. The electron density of states in conduction band (a) and valence band (b) is shown for  $\alpha$ -PbO in  $bc$ -plane (see Fig. 2.1). The figure and captions were taken from Ref. [20].

The density of states calculations for stoichiometric  $\alpha$ -PbO show sharp band edges with an *empty* forbidden gap of poly-PbO. However, conventional vapor deposited PbO layers are known to suffer from oxygen deficiency [15,29,30] and this changes the situation dramatically. Oxygen vacancies create a deep energy level near the middle of the band gap (1.03 eV above the top of the valence band) while lead vacancies create a shallow energy level in close proximity to the valence band maximum (0.1 eV above the top of the valence band) [31] (see Fig. 2.5). Moreover, it was reported that that oxygen vacancies have significantly lower formation energy than lead vacancies, which suggests a higher concentration of oxygen vacancies. In addition, the formation energy of oxygen vacancies depends on their charge state. Thus, an oxygen vacancy in its neutral state appears occupied with two electrons and has a formation energy  $V^O \sim 0.85\text{eV}$ . If the oxygen vacancy donates one electron, its formation energy is cut in half. In contrast, lead vacancies are initially neutral, but can accept an electron to lower their formation energy  $V^{\text{Pb}}$ , although not significantly: the formation energy drops from  $\sim 6.6$  eV to  $\sim 6.4$  eV (see Fig. 2.6).

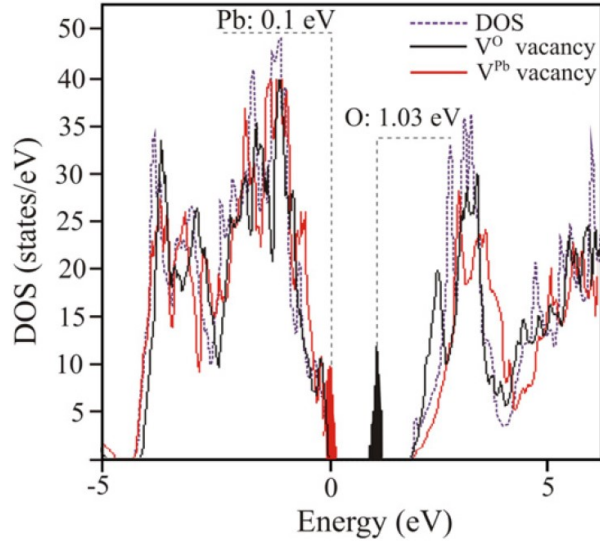


Figure 2.5. Density of states (DOS) is shown for several systems: dashed line represents a defect-free PbO, solid black line represents the same system with O vacancies, while the red line represents the system with Pb vacancies. The top of valence band was used as a reference point with 0 energy. The figure and captions were taken from Ref. [31].

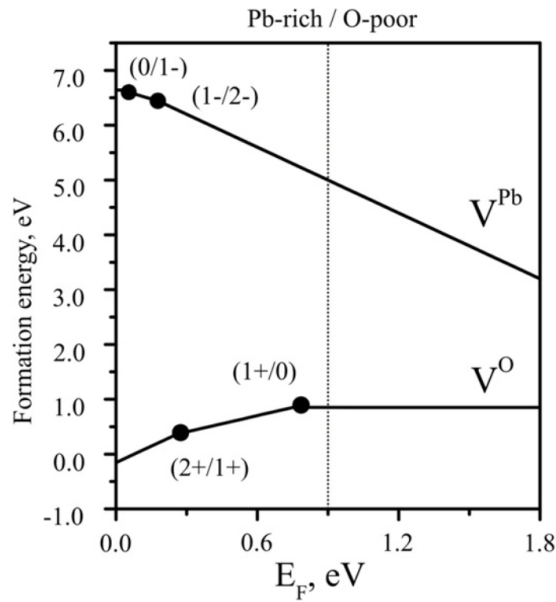


Figure 2.6. The formation energies of the defects for  $V^O$  and  $V^{Pb}$  in the Pb-rich/O-poor limit. The charge states, for which the added electron or hole remains localized on the vacancy site, are shown ( $1+/2+$  states for the  $V^O$  vacancy and  $2-/1-$  states for the  $V^{Pb}$  vacancy). The figure and captions were taken from Ref. [31].

The low formation energy of oxygen vacancies and their deep localization in the forbidden gap suggests that oxygen vacancies may significantly influence the charge transport and thus the whole performance of PbO. Indeed, deep traps reduce carrier mobility more significantly than shallow traps and exhibit longer release times. Therefore, the concentration of oxygen vacancies must be minimized in any practical PbO detector. The suggested modifications to the deposition process including ion bombardment of the growing layers (see Chapter 3) are aimed at improving layer stoichiometry and reducing oxygen vacancies. However, first, the basic deposition process of PbO layers will be reviewed in the next section.

## **2.3. Deposition process of PbO layers**

### *2.3.1. Selection of the PbO deposition technique*

There is a wide variety of methods and techniques for growing PbO as well as any other material. Based on the structure of the grown layer, they can be split in two groups, namely crystalline and non-crystalline deposition techniques. Table 2.3 below summarizes the major features of these techniques.

Table 2.3. Overview of known PbO deposition techniques.

Deposition techniques	Crystal structure	Deposition rate [ $\mu\text{m}/\text{min}$ ]	Substrate temperature [ $^{\circ}\text{C}$ ]	Crystal size/ coating area
Czochralski method [12]	Single crystal	33-83	$\sim 870$	$\sim 2 \times 2 \times 2 \text{ cm}^3$
Hydrothermal method [32]	Single crystal	Not indicated	400	$1 \times 1 \times 0.1 \text{ mm}^3$
Electrochemical method [33,34]	Microcrystalline film	$\sim 10$	80	Coating area depends on the anode size
Chemical vapor deposition (CVD) [1,27]	Poly-crystalline film	0.015	400-800	10 inch in diameter
Spray pyrolysis [35]	PbO film *	$\sim 0.004$	300	$2.5 \times 7.5 \text{ cm}^2$
Laser assisted deposition (LAD) [36]	Poly-crystalline film	5-20	150-300	Not specified
Sputter deposition [19,37]	PbO film *	0.01-0.1	Not indicated	Not specified
Thermal vacuum evaporation [4,8]	Poly-crystalline film	$\sim 1$	100	$18 \times 20 \text{ cm}^2$

\* the grown PbO sample is a not a single crystal, however further details of the sample structure were not specified.

Out of the extensive pool of available techniques, one is chosen to fit the requirements of the detector fabrication technology. The major criteria are:

1. The deposition process should allow direct deposition onto the a-Si electronics of the TFT imager and thus should not require substrate temperatures higher than  $\sim 200\text{-}240$  °C [38].
2. The deposition process should provide uniform coating over a large area  $\sim 18\text{ cm} \times 20\text{ cm}$  [8].
3. In order to make the process cost efficient, the deposition rate should be not less than  $\sim 0.5\text{ }\mu\text{m}/\text{min}$ .

These requirements significantly limit the choice of the deposition method. Particularly, they rule out crystalline deposition methods, which in general require high substrate temperatures and therefore do not allow direct deposition on an imaging matrix. In addition, the grown crystals are small in size (only  $\sim 2\text{ cm}$  in diameter) and therefore special crystal slicing with consequent bump bonding procedures are required to cover large detector areas [39,40]. This makes the detector fabrication very expensive and therefore less practical.

On the other hand, most of non-crystalline deposition techniques allow direct deposition on large substrates, however there are several limitations. CVD, spray pyrolysis and sputtering techniques suffer from small deposition rates (CVD and spray pyrolysis also require high substrate temperatures), with LAD it is difficult to obtain a uniform coating over large areas. Fabrication of a PbO detector with the electrochemical method would require submerging a TFT substrate into an aqueous solution which is not feasible. Alternatively, Cho et al. investigated the structure and X-

ray performance of PbO prepared with a particle-in-binder method [41]. For this purpose, PbO particles are first synthesized using a solution combustion method and mixed with a special binder that keeps the particles together. This PbO gel paste is then deposited onto the substrate. Such a deposition process might also not be practical, since it is hard to control the layer thickness and quality over the large area of the imager. Thus, all the deposition techniques discussed above had one or the more limitations and were not suitable for practical fabrication of the detector material. That said, there is still one technique which is known to satisfy all the deposition criteria. This technique is thermal vacuum evaporation. Thermal deposition of PbO layers was pioneered by the Philips research group in the early sixties [9,16]. At that time, they had started development of deposition technology for relatively thin  $\sim 10\text{-}20\ \mu\text{m}$  PbO films, which were used as the light sensitive target of “Plumbicon”- vacuum video tubes. More recently in 2004, this technique was scaled up for the fabrication of the first large area PbO flat panel detector prototype with  $340\ \mu\text{m}$  of PbO, required for the efficient absorption of diagnostic X-rays [8,42].

Thermal vacuum evaporation was shown to uniquely allow deposition at a high rate over a large detector area, compatible with a-Si imaging temperatures and therefore became the method of choice for the production of electronics-grade photosensitive PbO layers [4,7-9,15,43]. The details of the thermal deposition of PbO layers will be discussed in the next section.

### *2.3.2. Background of PbO deposition*

In the deposition process developed by Philips, high purity PbO powder is evaporated from a crucible at  $\sim 1000\ \text{°C}$  (melting point of PbO is  $890\ \text{°C}$ ) onto the substrate held at  $\sim 100\ \text{°C}$ , which yields a relatively high deposition rate of  $2\ \mu\text{m}/\text{min}$ . The deposition takes place in a background atmosphere of molecular oxygen at  $\sim 3\ \text{mTorr}$ , which is required for desired layer stoichiometry. PbO layers deposited under these conditions are very porous and composed of randomly oriented

platelets several microns in diameter and a few hundred nanometers thick. High porosity significantly reduces the packing density of the grown layers (up to 50 % of single crystal density), while the platelet structure that runs throughout the sample results in a rough surface morphology. The deposited films are unstable at ambient conditions and tend to degrade in several hours (the details of the PbO degradation will be elaborated in the next chapter) [4]. In addition, it was shown, that although samples are grown in a molecular oxygen atmosphere, the poly-PbO films suffer from suboptimal stoichiometry, exhibiting oxygen deficiency. The effect of oxygen deficiency in poly-PbO films is not completely understood, although it has been suggested that oxygen vacancies can act as trapping/recombination centers, and deteriorate charge transport in the material.

The features listed above for poly-PbO films make it challenging for practical utilization and need to be appropriately addressed. Fortunately, low packing density, poor sample stability and suboptimal stoichiometry of the grown film are common features of many materials (especially those prepared using the thermal evaporation method) and were shown to be a reflection of the same root cause, namely dramatic temperature mismatch between the substrate and the melting point of the material. Indeed, Thornton [44,45] and Anders [46] have shown that in order to achieve a highly packed structure during evaporative deposition, the temperature ratio between the substrate and the melting point of the material  $T^*$  should be higher than 0.5 – 0.6 (the closer this ratio is to unity, the more a refined structure is obtained). A good example is a-Se which has a melting temperature of 220 °C and it is conventionally evaporated onto a substrate at temperatures close to room temperature (e.g. ~ 60 °C). Such a substrate temperature provides a ratio of  $T^* = 0.67$ , which is well above 0.5. As a result, a-Se layers have a dense and uniform structure. However, if the ratio  $T^*$  is less than ~ 0.6 the more porous structure will be developed due to the limited mobility of the material on the surface of the growing film. Condensing atoms will attempt to diffuse over the

surface of the film, searching for an energetically preferred location, until they thermalize and buried by arriving material. During this process, the diffusion of material in the bulk of the film is insignificant which results in the development of a porous structure [47-49]. Thus, lower substrate temperatures and higher deposition rates lead to a more pronounced *pillar-like* structures, running along the whole layer with reduced density. This is exactly what is observed with conventional PbO deposition: the film is composed of platelets and it is very porous (about 50% porosity). The melting temperature of PbO is 890 °C, and even if the substrate temperature is increased to 100 °C, the ratio  $T^*$  is only slightly higher than 0.3, which is therefore not sufficiently high to create a densely packed structure.

Thus, it is the nature of the conventional deposition process, particularly the great thermal mismatch between the PbO vapor and the substrate that determines the crystalline order and causes the formation of the porous microstructure. In order to obtain a dense and more homogeneous film, the thermal mismatch between the PbO vapor and the substrate must be reduced. One way of doing this is by increasing the substrate temperature. In order to achieve temperature ratio  $T^* > 0.6$ , a substrate temperature must be around 600 °C. This constraint produces a significant dilemma, because such a high substrate temperature is not compatible with the a-Si electronics that are commonly employed in TFT detector substrates. Therefore, this approach is not practical for the fabrication of PbO flat panel X-ray imaging detectors.

Alternatively,  $T^*$  might be significantly improved by supplying additional energy to the growing film by means of ion assisted bombardment with gas ions [46-49]. Indeed, multiple studies have shown that when energetic ions arrive at the surface of the growing layer they transfer their energy to the atoms on the surface via collisions. This compresses the atoms within the film into a more dense structure, whereby the deposited energy facilitates surface atom mobility. Such a

process virtually increases the  $T^*$  ratio, and a packing density close to or equal to unity is normally obtained, without significantly overheating the substrate, and makes ion assisted deposition compatible with the imaging electronics. In addition, ion assisted deposition was shown to improve layer stoichiometry and make device performance insensitive to ambient conditions.

Therefore, inspired by the vast range of benefits of ion assisted deposition, we applied it to PbO. In general, the ion assisted deposition process is very close to the conventional deposition process of PbO: high purity PbO powder is the evaporated at  $\sim 1000$  °C on the substrate at  $\sim 20$ - $100$  °C. The major difference is that oxygen is not supplied directly to the chamber, but rather through an ion source. The results of an ion assisted deposition will be discussed in the next chapter, but first the principle of operation and merits of the ion source will be discussed in the next section.

### *2.3.3. Principle of operation of the ion source*

Fig. 3.1 illustrates the basic principle of operation of the end-Hall ion source, that was used for sample preparation. The gas, to be ionized, is admitted to the ion source between the magnet and the small base of the conical anode at a controlled flow rate. The hot filament cathode is located above the ion source and serves as a source of electrons. As voltage is applied between anode and cathode, electrons from the hot filament bombard the gas and ionization occurs. Most ion sources provide singly charged ions, for instance  $N_2^+$  and  $O_2^+$  for nitrogen and oxygen, respectively [50]. The magnet provides a divergent DC magnetic field that impedes the mobility of electrons as they drift to the anode, thus increasing their lifetime in the plasma. This results in a spatially distributed plasma potential field that accelerates ions away from the source. The energy of the accelerated ions depends on where they were created along the spatial potential field, but on average, the ion energy is  $\sim 60$ – $70\%$  of the anode voltage. The fraction of electrons that do not participate in gas ionization, serves as the neutralization for the ion beam [51,52].

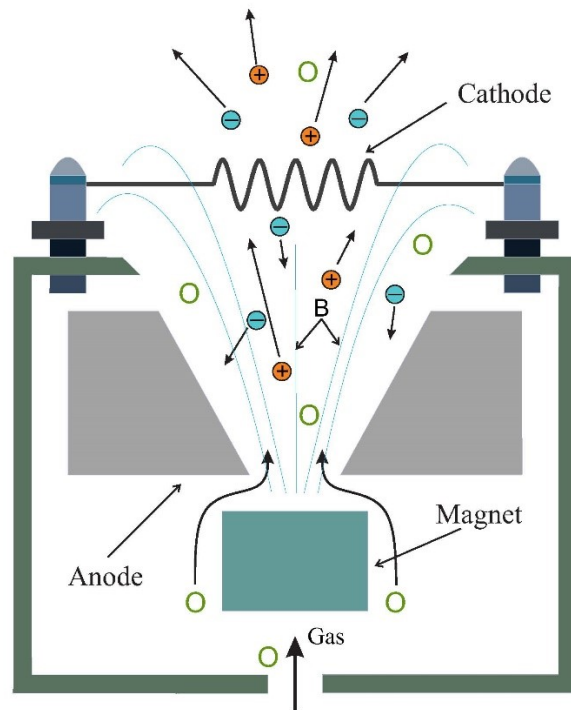


Figure 2.1 shows the cross section of the End-Hall ion source.

#### 2.3.4. Calculation of the ion source parameters

According to the Ref. [50], for  $T^* \approx 0.3$ , as for PbO, an additional energy of  $\sim 3\text{--}10$  eV per atom must be delivered to the growing film. If the energy is lower than 3 eV/atom, only partial (if any) modification of the structure is obtained, while higher than 10 eV/atom should not result in any further changes, and could rather cause undesirable compressive stress in the film.

In order to deliver the required energy dose to the growing film, three major deposition parameters must be considered. They are: the ion energy, ion current density (ion flux) and the deposition rate of the material. They are related as follows:

$$\text{Energy Dose per Atom} = (\text{Ion energy} \times \text{Flux}) / \text{Deposition rate}.$$

For example, if the energy of a single 100 eV ion is delivered to 10 deposited atoms, then each atom will get the dose of 10 eV/atom. While the same dose could be delivered by 10 ions of 10 eV each, both will have not the same effect on the growing layer. Indeed, it has been shown, that the best results during ion assisted deposition are achieved if the required *energy dose is delivered by 25-100 eV ions*. This is because ions of ~0–25 eV do not have enough momentum to disturb the bulk lattice atoms. Even if the ion flux is high the process is confined primarily to the surface cleaning of the physisorbed atoms, rather than modifying the structure of the layer. In order to affect the crystal lattice, the ion energy should be at least ~25–30 eV. With increasing ion energy, an enhancement of the surface atom mobility takes place. However, in the high-energy range ( $\geq 200$  eV), ions might cause significant damage to the grown film, by sputtering the film or undesirable gas implantation. Therefore, ions in energy range 25-100 eV is the golden mean (for Ar, N<sub>2</sub>, O<sub>2</sub>) and thus the most favorable for the ion assisted deposition process. In this case, ions have enough energy to modify the lattice structure without causing film damage.

Finally, according to the Ref. [53], the required ion current density can be calculated as follows:

$$i_i = \frac{R_a e \epsilon}{\epsilon_{ion}} \quad (2.1)$$

where  $e$  is the elementary charge in Coulombs,  $\epsilon$ - is the energy dose in eV/atom,  $\epsilon_{ion}$ - is the gas ion energy and  $R_a$ -is evaporated atom arrival rate on the substrate in atoms/cm<sup>2</sup> s. Atom arrival rate is related to the deposition rate  $R_d$  in Å/s by:

$$R_a = \frac{10^{-8} R_d \rho N}{1.6 * 10^{-24} w} \quad (2.2)$$

where  $\rho$ - is the film density in g/cm<sup>3</sup>,  $N$ -number of atoms in the deposited molecule,  $w$ - is the atomic weight of the molecule in a.m.u.

In the case of lead oxide  $N=2$  (PbO molecule consists of two atoms: one lead and one oxygen) and  $w=223$ . Thus, substituting the required energy dose 1–10 eV/ atom and the deposition rate 20–150 Å/s into equations (3.1), (3.2), the ion current density should be in the range of  $\sim 0.3\text{--}3$  mA/cm<sup>2</sup>, provided the ion energy is in the range 25-100 eV.

## References

1. Madsen, L. D., Weaver, L. Characterization of lead oxide thin films produced by chemical vapor deposition. *J. Am. Ceram. Soc.* **81**, 988–996 (1998).
2. Terpstra, H. J., de Groot, R. A. and Haas, C. Electronic structure of the lead monoxides: bond structure calculations and photoelectron spectra. *Phys. Rev. B.* **52**, 11690-11697 (1995).
3. Watson, G. W., Parker, S. C. and Kresse, G. Ab initio calculation of the origin of the distortion of a-PbO. *Phys. Rev. B.* **59**, 8481-8486 (1999).
4. Simon, M. et al. PbO as direct conversion x-ray detector material. *Proc. SPIE* **5368**, 188-199 (2004).
5. Kasap, S. & Rowlands, J. A. Direct-conversion flat-panel X-ray image sensors for digital radiography. *Proc. IEEE.* **90**, 591-604 (2002).
6. Droessler, L.M., Assender, H.E. & Watt, A.A.R. Thermally deposited lead oxides for thin film photovoltaics. *Mater. Lett.* **71**, 51-53 (2012).
7. Simon, M., Wiechert, D. U. & Feldmann, C. Lead oxide based photosensitive device and its manufacturing method. US Patent 7649179 B2 2005.
8. Simon, M. et al. Analysis of lead oxide (PbO) layers for direct conversion x-ray detection. *IEEE Trans. Nucl. Sci.* **52**, 2035-2040 (2005).

9. Haan, E. F., Van der Drift, A. & Schampers, P. P. M. The “Plumbicon”, a new television camera tube. *Philips Tech. Rev.* **25**, 133-180 (1964).
10. Wiechert, D.U., Grabowski, S. P. & Simon, M. Raman spectroscopic investigation of evaporated PbO layers. *Thin Solid Films.* **484**, 73-82 (2005).
11. Schottmiller, J. C. Photoconductivity in tetragonal and orthorhombic Lead Monoxide layers. *J. Appl. Phys.* **37**, 3505-3510 (1966).
12. Oka, K., Unoki, H. & Sakudo, T. Growth of single crystals of lead monoxide. *J. Cryst. Growth.* **47**, 568-572 (1979).
13. Baleva, M. I., Bozukov, L. N. & Tuncheva, V. D. Crystal structure and growth mechanism of lead monoxide thin films produced by pulsed laser deposition. *J. Phys. Chem.* **98**, 13308-13313 (1994).
14. Klinger, R. E. & Carniglia, C. K. Optical and crystalline inhomogeneity in evaporated zirconia films. *Appl. Opt.* **24**, 3184-3187 (1985).
15. Bigelow, J.E. & Haq, K. E. Significance of fatigue in lead oxide vidicon target. *J. Appl. Phys.* **33**, 2980-2982 (1962).
16. Damon, R. W. & Eshbach, J. R. Photoconductor of lead oxide and method of making. US Patent 2888370 A 1956.
17. Pauling, L. & Moore, W. J. Golden Book of Phase Transitions. Wroclaw. vol. 1 (2002).
18. Baleva, M. I. & Tuncheva, V. D. Optical characterization of lead monoxide films grown by laser-assisted deposition. *J. Solid. State. Chem.* **110**, 36-42 (1994).
19. Venkataraj, S. et al. Structural and optical properties of thin lead oxide films produced by reactive direct current magnetron sputtering *J. Vac. Sci. Technol. A* **19**, 2870-2878 (2001).
20. Berashevich, J., Semeniuk, O., Rowlands, J. A. & Reznik, A. Anisotropy of the carrier effective masses in bulk  $\alpha$ -PbO. *EPL* **99**, 47005 (2012).

21. <http://rruff.info/chem=Pb,O/notchem=all/display=default/R080019>. Accessed 14 June 2017.
22. <http://rruff.info/chem=Pb,O/notchem=all/display=default/R080018>. Accessed 14 June 2017.
23. <http://www.chem.ucl.ac.uk/resources/raman/pigfiles/redlead.html>. Accessed 14 June 2017.
24. <http://rruff.info/chem=Pb,O/notchem=all/display=default/R050426>. Accessed 14 June 2017.
25. Kay, M. I. Golden Book of Phase Transitions. Wroclaw. vol. 1 (2002).
26. Kim, K. S., O'Leary, T. J. & Winograd, N. X-ray photoelectron spectra of lead oxides. *Anal. Chem.* **45**, 2214–2218 (1973).
27. Dai, G. & Xu, J. Low pressure chemical vapor deposition of PbO thin film from lead dichloride. *J. Mater. Sci. Lett.* **17**, 969-971 (1998).
28. Zacharia, R., Ulbricht, H. & Hertel, T. Interlayer cohesive energy of graphite from thermal desorption of polyaromatic hydrocarbons. *Phys. Rev. B.* **69**, 155406 (2004).
29. Hwang, O. H. et al. Effect of thermal annealing of lead oxide film. *Nucl. Instrum. Methods Phys. Res. A.* **633**, S69-S71(2011).
30. Scanlon, D. O., Kehoe, A. B. & Watson, G. W. Nature of the band gap and origin of the conductivity of PbO<sub>2</sub> revealed by theory and experiment. *Phys. Rev. Lett.* **107**, 246402 (2011).
31. Berashevich, J., Semeniuk, O., Rubel, O., Rowlands, J. A. & Reznik, A. Lead monoxide a-PbO: electronic properties and point defect formation. *J. Phys.: Condens. Matter.* **25**, 075803 (2013).
32. Keezer, R. C., Bowman, D. L. & Becker, J. H. Electrical and Optical Properties of Lead Oxide Single Crystals. *J. Appl. Phys.* **39**, 2062-2066 (1968).

33. Veluchamy, P. & Minoura, H. Simple electrochemical method for the preparation of a highly oriented and highly photoactive  $\alpha$ -PbO film. *Appl. Phys. Lett.* **65**, 2431-2433 (1994).
34. Zhitomirsky, I. et al. Electrochemical preparation of PbO films. *J Mater Sci Lett* **14**:807-810 (1995).
35. Thangaraju, B. & Kaliannan, P. Optical and structural studies on spray deposited  $\alpha$ -PbO thin films. *Semicond. Sci. Technol.* **15**, 542–545 (2000).
36. Baleva, M. & Tuncheva, V. Laser-assisted deposition of PbO films. *J. Mater. Sci. Lett.* **13**, 3-5 (1994).
37. Pauleau, Y. & Harry, E. Reactive sputter-deposition and characterization of lead oxide films. *J. Vac. Sci. Technol. A.* **14**, 2207 (1996).
38. G. Zentai. Photoconductor-based (direct) large-area x-ray imagers. *JSID.* **17**, 543-550 (2009).
39. D. Pacella. Energy-resolved X-ray detectors: the future of diagnostic imaging. *RMI*, **8**, 1-13 (2014).
40. Krüger, H. et al. CIX - a detector for spectral enhanced X-ray imaging by simultaneous counting and integrating. *Proc. SPIE.* **6913**, 69130P (2008).
41. Cho, S. et al. Effect of annealing on the x-ray detection properties of nano-sized polycrystalline lead oxide films. *Jpn. J. Appl. Phys.* **47**, 7393-7397 (2008).
42. Beutel, J., Kundel, H. L. & Van Metter, R. L. *Handbook of medical imaging* Vol.1 (eds Rowlands, J. A., Yorkstone, J.) Ch. 4, 223-328 (SPIE, 2000).
43. van der Drift, A. Texture of a vapor-deposited lead-monoxide layer. *Philips Res. Rep.* **21**, 289 (1966).
44. Thornton, J. A. Influence of apparatus geometry and deposition conditions on the structure and topography of thick sputtered coatings. *J. Vac. Sci. Technol.* **11**, 666 (1974).

45. Thornton, J. A. Influence of substrate temperature and deposition rate on structure of thick sputtered Cu coatings. *J. Vac. Sci. Technol.* **12**, 830 (1975).
46. Anders, A. A structure zone diagram including plasma-based deposition and ion etching. *Thin Solid Films.* **518**, 4087-4090 (2010).
47. Müller, K. H. Model for ion-assisted thin-film densification. *J. Appl. Phys.* **59**, 2803-2807 (1986).
48. Müller, K. H. Models for microstructure evolution during optical thin film growth. *Proc. Soc. Photo-Opt. Instrum. Eng.* **821**, 36-44 (1988).
49. Sargent, R. B. Effects of surface diffusion on thin-film morphology: a computer study. *Proc. Soc. Photo-Opt. Instrum. Eng.* **1324**, 13-31 (1990).
50. Kaufman, H.R. Applications of broad-beam ion sources: an introduction. Fort Collins, 2011.
51. Oudini, N., Hagelaar, G. J. M., Boeuf, J.-P. & Garrigues, L. Physics and modeling of an end-Hall (gridless) ion source. *J. Appl. Phys.* **109**, 073310 (2011).
52. Mahoney, L., Burtner, D. & Siegfried, D. A new end-hall ion source with improved performance. *Soc. Vac. Coaters, 49th Annual Tech. Conf. Proc.* **505**, pp. 706-711 (2006).
53. Kaufman, H. R. & Harper, J.M.E. Ion-assist applications of broad-beam ion sources. *Proc. SPIE.* **5527**, 50-68.

## **Chapter 3: Charge transport in poly-PbO**

### **3.1. Hole transport in poly-PbO**

This topic has been elaborated in the following publication: [O. Semeniuk](#), G. Juska, J. -O. Oelerich, M. Wiemer, S. D. Baranovskii & A. Reznik “Charge transport mechanism in lead oxide revealed by CELIV technique”, published in *Scientific Reports*, Volume 6, Article number: 33359 (2016). The full text of the publication is listed below.

# **Charge transport mechanism in lead oxide revealed by CELIV technique**

O. Semeniuk<sup>1\*</sup>, G. Juska<sup>2</sup>, J. -O. Oelerich<sup>3</sup>, M. Wiemer<sup>3</sup>, S. D. Baranovskii<sup>3</sup> and A. Reznik<sup>4</sup>

1. Chemistry and Material Science Program, Lakehead University, 955 Oliver Road, Thunder Bay, ON, P7B 5E1
2. Department of Solid State Electronics, Vilnius University, Saulėtekio 9 III k., 10222 Vilnius, Lithuania
3. Faculty of Physics, Philipps University Marburg, Renthof 6, 35032 Marburg, Germany
4. Department of Physics, Lakehead University, 955 Oliver Road, Thunder Bay, ON, P7B 5E1

\*e-mail: [osemeniu@lakeheadu.ca](mailto:osemeniu@lakeheadu.ca)

## **Abstract**

Although polycrystalline lead oxide (PbO) belongs to the most promising photoconductors for optoelectronic and large area detectors applications, the charge transport mechanism in this material still remains unclear. Combining the conventional time-of-flight and the photo-generated charge extraction by linear increasing voltage (photo-CELIV) techniques, we investigate the transport of holes which are shown to be the faster carriers in poly-PbO. Experimentally measured temperature and electric field dependences of the hole mobility suggest a highly dispersive transport. In order to analyze the transport features quantitatively, the theory of the photo-CELIV is extended to account for the dispersive nature of charge transport. While in other materials with dispersive transport the amount of dispersion usually depends on temperature, this is not the case in poly-PbO, which evidences that dispersive transport is caused by the spatial inhomogeneity of the material and not by the energy disorder.

## **Introduction**

Non-crystalline materials are of great significance to a variety of applications since they offer a low cost reliable technology combined with reproducible outcomes. This is, of course, true if these materials achieve the desirable performance. Therefore, thorough study of material properties as an input to technology optimizations is crucially needed and frequently opens new technological horizons. One example is a-Si:H: by revealing a way to passivate dangling bonds in a-Si with hydrogen, it opened a new era in large area electronics based on a-Si:H. Another example is amorphous selenium (a-Se): inventing ways to stabilize a-Se against crystallization and improve charge transport gave rise to a broad range of applications; from the first Xerox photocopiers, to Vidicon pick-up tubes, and finally to the ultra-sensitive High-gain Avalanche Rushing (HARP) TV cameras [1]. A natural transition to thick a-Se layers for adequate X-ray absorption resulted in a

new generation of high-resolution direct conversion mammography detectors with a-Se layer as the X-ray-to-charge transducer [2]. a-Se based detectors revolutionized X-ray medical imaging, offering diagnostic capabilities in the mammographic energy range (around 20 keV), which was not achievable by other commercial mammographic detectors [3].

Besides a-Se, there have been a number of other non-crystalline photoconductors, which have been investigated for use as X-ray-to-charge converters in X-ray detectors [4-18], although they are not yet mature enough for commercial use [19]. Polycrystalline Lead Oxide (PbO) holds a special place in this list since, similar to a-Se, it has been used previously in optical imaging, in so-called Plumbicon video pick-up tubes. Due to the good photoconductive properties of PbO, Plumbicons were used extensively in broadcast, fluoroscopy and digital subtraction angiography in conjunction with an image intensifier. The wide band gap of PbO in combination with the high X-ray absorption, low electron-hole pair creation energy [17, 18], and the absence of K absorption edges up to 88 keV X-rays [19] makes polycrystalline PbO a good candidate to expand the advantages of the direct conversion X-ray detection scheme over the fluoroscopic (around 70 keV) energy range due to its much higher atomic number than in a-Se.

In 2005, Simon *et al.* evaluated the imaging performance of the first prototype of a direct conversion flat panel imager with a thick ( $\sim 300 \mu\text{m}$ ) layer of poly-PbO [18], which showed high spatial resolution with an effective fill factor close to unity. However, it did not show the expected high conversion efficiency and adequate temporal behavior for fluoroscopic applications. Thus, optimization of PbO technology is required to make “detector grade” thick layers. This, in turn, needs a comprehensive analysis of the electronic characteristics of the material in order to understand the interplay between X-ray performance and material properties.

Despite continuous interest in polycrystalline PbO since 1960's, the mechanisms of charge carrier transport and recombination – two major features to be used as a feedback for technology optimization, have not yet been clarified. The data on charge carrier mobility has mostly been obtained from single crystal materials. For example, Keezer *et al.* measured electron mobility,  $\mu_e$ , and mobility-lifetime product,  $\mu_e\tau_e$ , (where  $\tau_e$  is the electron lifetime) of single crystals produced by the hydrothermal technique. The corresponding values were reported to be:  $\mu_e = 100 \text{ cm}^2/\text{Vs}$ ,  $\mu_e\tau_e = 10 \text{ cm}^2/\text{V}$  for tetragonal and  $\mu_e = 50 \text{ cm}^2/\text{Vs}$ ,  $\mu_e\tau_e = 4 \times 10^{-4} \text{ cm}^2/\text{V}$  for orthorhombic single crystal PbO [20]. At the same time, Broek reported  $\mu\tau = 2 \times 10^{-9} \text{ cm}^2/\text{V}$  for a tetragonal PbO crystal, though the type of carrier was not specified [21]. For polycrystalline material, the reported data are on the mobility-lifetime product only. Schottmiller measured  $\mu\tau$  to be  $\sim 10^{-7} \text{ cm}^2/\text{V}$  and  $\sim 10^{-9} \text{ cm}^2/\text{V}$  for tetragonal and orthorhombic phases of poly-PbO, respectively (the type of charge carrier was not specified) [22]. Simon *et al.* reported  $\mu\tau = 4.4 \times 10^{-7} \text{ cm}^2/\text{V}$  for evaporated layers containing fractions of both phases [18]. Although the type of charge carrier in Ref [18] was not specified, the experimental results presented there were later treated by Kabir, allowing him to derive the mobility-lifetime products for electrons and holes,  $\mu_e\tau_e = 3.5 \times 10^{-7} \text{ cm}^2/\text{V}$  and  $\mu_h\tau_h \approx 10^{-8} \text{ cm}^2/\text{V}$ , respectively [23]. The wide scatter of the reported values is not surprising since the lifetime  $\tau$  depends on the carrier concentration, which makes evaluation of this parameter very sensitive to the measurement technique used. In contrast to the mobility-lifetime product, the carrier drift mobility  $\mu$  is an objective parameter to evaluate transport in any semiconductor. However, no direct measurements of carrier mobility in polycrystalline PbO have been reported yet.

In the current manuscript, we provide a comprehensive analysis of the temperature and field dependencies of the mobility of the most mobile charge carriers (holes) in polycrystalline PbO using the conventional time-of-flight (TOF) [24] and photo- charge extraction by linear increasing

voltage (photo-CELIV) [25] techniques. It appears that holes in poly-PbO conduct electrical current in a dispersive regime, in which the carrier mobility is time-dependent and therefore it does not have a universal value that could be treated as a characteristic one for the material. In order to apply the CELIV technique in the case of the dispersive regime, it was necessary to extend the CELIV theory to account for the dispersive nature of charge transport.

## Results

### Experimental data on charge transport by TOF

The typical TOF current transient for holes in the polycrystalline PbO is shown in Fig. 1a. A featureless drop in the photocurrent indicates that transport occurs in the so-called dispersive mode, for which the carrier mobility decreases in the course of time. Generally, the time dependencies of the photocurrent ( $\Delta i$ ) for the dispersive transport mode are given by the following expression [26]:

$$\begin{cases} \Delta i(t) \sim t^{-(1-\alpha)}, t < t_{tr} \\ \Delta i(t) \sim t^{-(1+\alpha)}, t > t_{tr} \end{cases}, \quad (1)$$

where  $t_{tr}$  is the transit time of the carriers through the sample and  $\alpha$  – is the so-called dispersion parameter. The values of  $\alpha$  usually vary for different materials between zero (the extreme case of dispersion) and unity (non-dispersive transport). In order to determine  $\alpha$ , we plot in the inset to Fig. 1a the current transient in the double logarithmic scale:  $\alpha = 0.2$  is found from the initial slope of the signal indicating a very high degree of dispersion for transport of holes in PbO. It is, however, not possible to check the  $\alpha$  value from the current decay at  $t > t_{tr}$  since the exact inflection point and the transit time  $t_{tr}$  is hard to determine even in the double logarithmic plot. Therefore, we have chosen the photo-CELIV technique as an alternative to the TOF in order to check the value of  $\alpha$ . The theoretical support of the photo-CELIV technique has been developed so far only for the case of a non-dispersive charge transport [25]. In the next section, we present our experimental results

obtained by the photo-CELIV technique and in the subsequent section we develop a theory for the photo-CELIV in the case of dispersive transport.

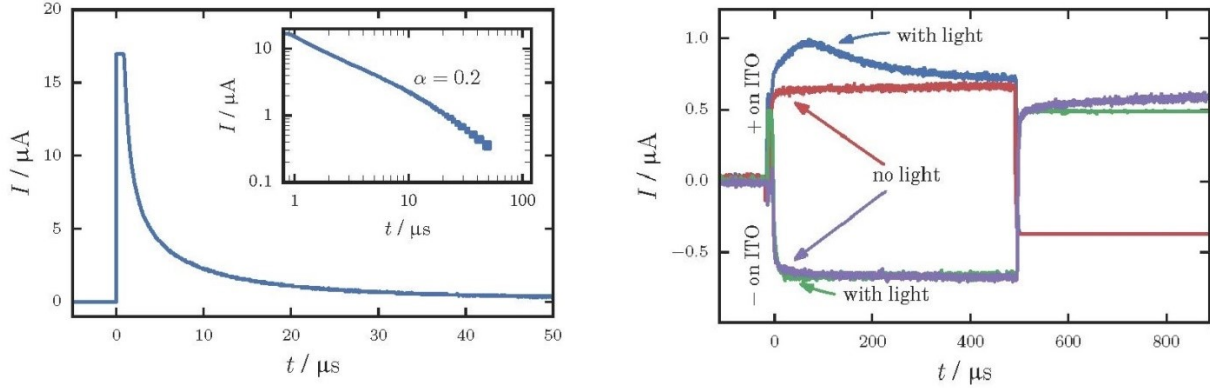


Figure 1. (a) TOF current transient measured at  $F=1 \text{ V}/\mu\text{m}$  is plotted in linear scale. The inset shows the current transient in double logarithmic scale. The TOF measurements were performed with excitation wavelength of 355 nm. (b) CELIV current transients with and without illumination for different polarities of applied voltage. Note: for both TOF and CELIV measurements an excitation wavelength of 355 nm was used for near-surface photogeneration.

### Experimental data on charge transport by photo-CELIV

The typical photo-CELIV signal measured with a strongly absorbed 355 nm light pulse is shown in Fig. 1b. When positive polarity is applied to the illuminated electrode, a clear photo-peak is seen on the CELIV trace and a photocurrent is attributed to the drift of photogenerated holes. The photocurrent rises rapidly until the majority of mobile carriers have been extracted at  $t_{peak}$ , and then drops precipitously. Please, note that the splash of a signal of reverse polarity after the carrier extraction is due to the shape of the applied voltage pulse, which consists of a positive voltage ramp (needed for carrier extraction) followed by symmetrical negative ramp that drives the signal below the initial value.

When negative polarity is applied to the same illuminated electrode, only minor deviation from the capacitive signal with no pronounced photo-peak is observed, suggesting that the duration of the

experiment was insufficient to observe extraction of slow electrons at the applied electric fields. Previously, it was shown that photo-CELIV with uniform volume absorption provides the most accurate measurements of the mobility [27]. Therefore, strongly absorbed light (355 nm) was used to determine the type of carriers, while a wavelength of 532 nm was used for mobility measurements.

### **Analysis of photo-CELIV for dispersive transport**

If charge carriers are generated in the entire volume of a sample, the total current is given by [25]:

$$i(t) = i_0 + \Delta i = \frac{\varepsilon\varepsilon_0 A}{d} + epv_{dr}(t)\left(1 - \frac{l(t)}{d}\right) \quad (2)$$

where  $i_0$  is the capacitive component of the total current (equation (2) is applicable when  $\Delta i < i_0$ ),  $\varepsilon\varepsilon_0$  is the dielectric permittivity of the material,  $e$  is the elementary charge,  $p$  is the concentration of carriers,  $v_{dr}$  is the drift velocity,  $A = dU/dt$  is the slope of the voltage ramp and  $l(t)$  is the extraction depth that equals to:

$$l(t) = \int_0^t v_{dr}(t)dt \quad (3)$$

In the case of dispersive transport, the motion of the drifting packet of the photo-generated charge slows down with time, resulting in the time dependent drift mobility:

$$\mu(t) = Ct^{-(1-\alpha)},$$

where  $C$  is the time-independent coefficient. For a voltage that is linearly increasing with time, drift velocity is given by:

$$v_{dr}(t) = C \frac{At^\alpha}{d} \quad (4)$$

According to equations (3) and (4), the extraction depth becomes dependent on  $\alpha$  as:

$$l(t) = \frac{cA}{d} \frac{t^{\alpha+1}}{(\alpha+1)}. \quad (5)$$

Concomitantly, the time needed to reach the peak of the photocurrent,  $t_{peak}$ , also becomes dependent on  $\alpha$ . In order to find out this dependence, we substitute equations (4) and (5) into equation (2) and determine  $t_{peak}$  by differentiating equation (2) over time and equating the result to zero:

$$ep \frac{\alpha c A t_{peak}^{\alpha-1}}{d} - ep \frac{(2\alpha+1)C^2 A^2}{d^3} \frac{t_{peak}^{2\alpha}}{(\alpha+1)} = 0 \quad (6)$$

or:

$$t_{peak} \sim A^{-\frac{1}{1+\alpha}}. \quad (7)$$

The carrier mobility is related to the peak position as:

$$\mu(F) = \mu \left( \frac{A t_{peak}}{d} \right) = \frac{\alpha(\alpha+1)}{2\alpha+1} \frac{d^2}{t_{peak}^2 A} \quad (8)$$

In the case of a non-dispersive transport equation (8) is transformed into  $\mu(F) = \frac{2}{3} \frac{d^2}{t_{peak}^2 A}$  in full agreement with the previously suggested expression [25]. Equation (8) allowed us to calculate  $\mu_h(F)$  using the measured dependence in the technically achievable range of electric fields (limited by the system noise and the bandwidth of the signal generator).

In Fig. 2,  $t_{peak}$  is plotted as a function of  $A$  for different temperatures between 233 K and 333 K.

In accordance with equation (7), the slope of  $\log(t_{peak})$  vs  $\log(A)$  curve yields the dispersion parameter  $\alpha$  which is found to be 0.22. This is in perfect agreement with the value  $\alpha = 0.2$

determined above from the slope of the TOF signal. Remarkably, the slope in the  $t_{peak}(A)$  dependence shown in Fig. 2 is almost insensitive to the change in temperature, which evidently shows that  $\alpha$  is temperature-independent. As shown in Fig. 3, mobility also does not demonstrate any significant temperature dependence.

Numerous recent studies suggested that photo-CELIV and CELIV mobility calculations using equations are not necessarily reliable unless combined with numerical simulations [28-31]. In our work we do not implement numerical simulations so the question might arise on whether our theoretical analysis is sufficiently accurate. It should be noted that numerical simulations have been proven unavoidable when specific experimental conditions are not accounted for when using traditional CELIV equations. Such conditions are: (i) charge carriers are generated close to the surface by strongly absorbed light. This results in non-uniform charge carrier distribution through the sample; (ii) the photocurrent ( $\Delta i$ ) exceeds the  $i_0$ , which is a capacitive component of the total current  $i$ , thus redistributing the internal electric fields; (iii) the linearly increasing voltage is comparable to the built-in barrier voltage on the electrode/semiconductor interface. In this case, a fraction of applied voltage is used to overcome the built-in potential. An offset voltage must be then used to compensate for this phenomenon, otherwise incorrect mobility values would be obtained.

In our study, the charge carriers were generated by the uniform volume absorption, which was shown to provide the most accurate measurements of the mobility [27]. At the same time, the light intensity was carefully adjusted in such a way that the magnitude of the photocurrent  $\Delta i$  did not exceed the magnitude of the capacitive signal  $i_0$  (Fig. 1b), thus excluding the internal field modulation [25]. Fig. 1b also shows that only capacitive signal is observed when sample is not irradiated with light, indicating that the equilibrium carriers do not affect the photo peak

measurements [25]. The total applied voltage to the sample was about 20 V, which is significantly larger than the built-in barrier potential that is usually of the order of a volt. Therefore, only a minimal effect (if any) of the barrier is expected on the measured results.

By comparison with the results of numerical simulations, Lorrmann et al. [28] have developed a criterion for the validity of the simplified approach based on equations, as derived in the pioneering papers for the CELIV technique. According to this criterion, equations without numerical simulations are reliable if the dimensionless voltage slope  $A'$  is larger than unity:

$$A' = \frac{2\varepsilon^2 \varepsilon_0^2}{e^2 d^2 p^2 \mu} A > 1. \quad (9)$$

Although criterion (9) has been suggested only for the case of equilibrium carriers [28], one might try to use it for the case of photo-CELIV just for estimations. In order to make the estimates, one should take into account that different mobility values shown in Fig. 3 were measured at different  $A$  values shown in Fig. 2. For all our experiments, the maximum voltage bias has been kept constant  $U = 10$  V, while voltage pulse time was varied, providing different voltage ramps  $A$ . Therefore, for each mobility measurement its own  $A$  has been set. For instance,  $\mu = 6 \times 10^{-2}$  cm<sup>2</sup>/Vs was measured at  $A = 10^7$  V/s, while  $\mu = 2 \times 10^{-2}$  cm<sup>2</sup>/Vs corresponds to  $A = 10^6$  V/s, etc. Inserting these  $(A, \mu)$  values along with  $d = 5$  μm,  $p = 5 \times 10^{19}$  m<sup>-3</sup>,  $\varepsilon = 13$  into criterion (9) one can claim, that the criterion is fulfilled for  $A$  values between  $10^4$  and  $10^7$  V/s. For two lowest  $A$  values of  $10^2$  V/s and  $10^3$  V/s, the criterion (9) would be valid for  $\mu$  smaller than  $1.65 \times 10^{-5}$  cm<sup>2</sup>/Vs and  $1.65 \times 10^{-4}$  cm<sup>2</sup>/Vs, respectively. As it is seen from Fig. 3, the corresponding measured mobilities are slightly larger than these values, and one can only claim the fulfilling of criterion (9) by order of magnitude. More theoretical study is necessary to develop a similar criterion for the case of non-equilibrium carriers relevant to the photo-CELIV technique.

Overall, the experiments were performed under conditions, which were shown to provide most accurate values of mobility [25, 27]. Thus, uniformly absorbed light was used to generate carriers and the illumination level was adjusted to provide the magnitude of the photocurrent lower than the capacitive one. The measurements were repeated multiple times on different spots of the samples, providing essentially the same result. Therefore, the only major source of uncertainties in the mobility measurement is believed to come from how accurately the photo-peak position can be determined. The latter is limited by the width of the CELIV signal at the photo peak. As seen from Fig. 1b and Fig. 4, the peak position can be reasonably well defined within less than  $\pm 5\%$  of the  $t_{peak}$  value. This results in relative uncertainty to be smaller than the symbol size in Figs. 2, 3.

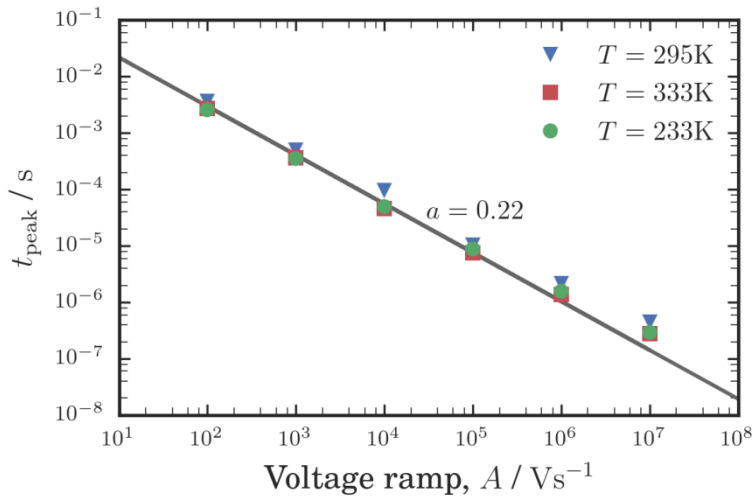


Figure 2. Dependence of  $t_{peak}$  on voltage ramp  $A$  for different temperatures. When plotted on a log-log scale,  $t_{peak}$  shows linear dependence on  $A$ , with a slope, corresponding to  $\alpha = 0.22$ . Note: uniformly absorbed light of 532 nm was used for  $t_{peak}$  measurements.

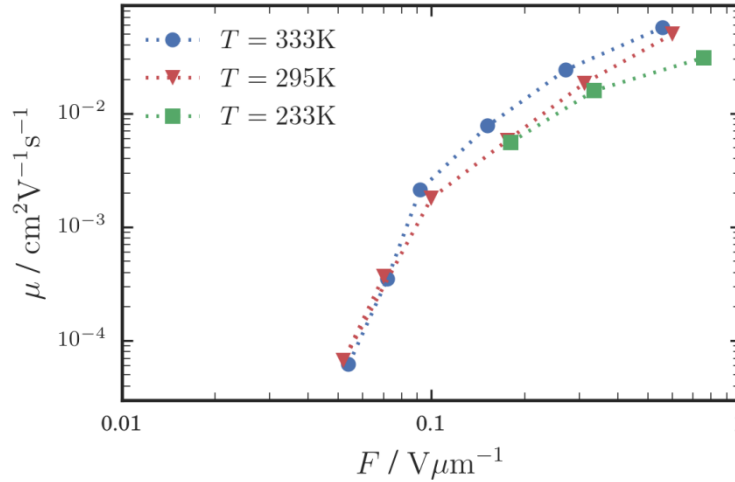


Figure 3. Dependence of hole mobility on electric field for different temperatures. Hole mobility tends to reach  $\sim 0.1 \text{ cm}^2/\text{Vs}$  at  $F \sim 1 \text{ V}/\mu\text{m}$ , while remaining almost temperature independent.

### Experimental data on recombination of charge carriers

In order to investigate the recombination in PbO, measurements by the CELIV technique were performed at different light intensities and delay times  $t_{del}$ . Fig. 4 shows the magnitude of the photocurrent  $\Delta i$  as a function of the delay time at light intensity which allows  $\Delta i$  to significantly exceed the magnitude of the capacitive signal  $i_0$ .

The relatively low mobility value of carriers ( $\mu_h \sim 0.1 \text{ cm}^2/\text{Vs}$  at  $F = 1 \text{ V}/\mu\text{m}$ ) in poly-PbO suggests that recombination of carriers occurs in the so-called Langevin mode [32, 33]. In the Langevin mode, the recombination rate is limited by the time, which carriers need to meet in space, i.e., recombination is limited by the transport process. Juska *et al.* performed a detailed analysis of the effect of recombination on the CELIV tracers, and showed that a photocurrent  $\Delta i$  exceeding the magnitude of the capacitive signal  $i_0$  (like the one demonstrated in Fig. 4) unambiguously indicates that recombination is reduced in comparison to the conventional three-dimensional Langevin recombination [29].

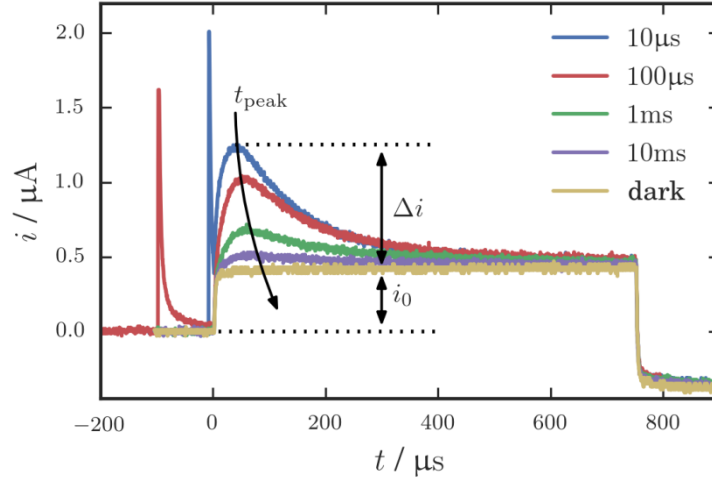


Figure 4. Dependence of the total current  $i$  and the photocurrent  $\Delta i$  on the delay time  $t_{del}$  for the excitation with the uniformly absorbed light of 532 nm. The photocurrent  $\Delta i$  decreases with time as carriers recombine.

Fig. 4 also allows to estimate hole lifetime  $\tau_h$  and mobility-lifetime product  $\mu_h \tau_h$  for our experimental conditions. For this we calculated the density of the photogenerated holes  $p$  by integrating the area under the photocurrents shown in Fig. 4 and subtracting the contribution of the capacitive signal. The results are plotted in Fig. 5 as function of the delay time  $t_{del}$ . As it is seen from Fig. 5, the carrier density remains constant for  $\sim 30 \mu s$ . After this,  $p$  starts to decrease gradually, indicating the beginning of the recombination process. Taking into account the reduced Langevin recombination, we can assume that hole concentration depends on time as:

$$p(t) = p_0 \exp\left(-\frac{t}{\tau_h(p)}\right) \quad (10)$$

with the hole lifetime  $\tau_h(p)$  that depends on the carriers' concentration  $p$ . The concentration-dependent carrier lifetime is inherent to any bimolecular recombination including the reduced Langevin one. Fitting our experimental results with the equation (10) in the vicinity of initial hole concentration yields  $\tau_h \approx 200 \mu s$ .

Taking  $\mu_h \approx 0.1 \text{ cm}^2/\text{Vs}$  at  $F = 1 \text{ V}/\mu\text{m}$ , one can deduce that  $\mu_h \tau_h = 2 \times 10^{-5} \text{ cm}^2/\text{V}$  at the carrier concentration  $\sim 5 \times 10^{13} \text{ cm}^{-3}$ . It should be noted, that in the disordered materials with bimolecular type of recombination, lifetime depends on carrier concentration and mobility. In such, carrier lifetime should not be considered as a material parameter [34]. In contrast,  $\tau$  is a characteristic of a device or experimental conditions [34] and hence it is reported here in conjunction with the hole concentration  $p$ .

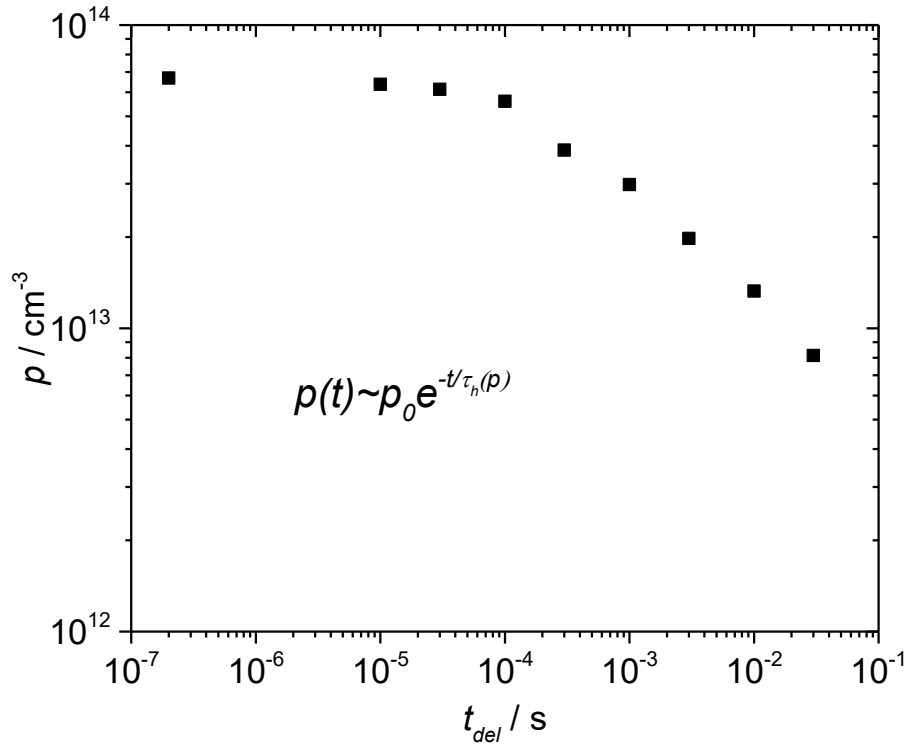


Figure 5. Photogenerated carrier density is plotted as a function of delay time  $t_{del}$ .

## Discussion

The hole mobility obtained from CELIV measurements depends strongly on the electric field and tend to reach  $\sim 0.1 \text{ cm}^2/\text{Vs}$  at comparatively low  $F = 1 \text{ V}/\mu\text{m}$ ; electrons were found to be much

slower carriers and did not contribute to the signal within the time scale of the performed measurements (see Fig. 1b). Remarkably, the hole mobility in PbO is similar to that in a-Se at room temperature, the only photoconductor, which is currently used commercially in direct conversion mammographic X-ray detectors. However, even though the carrier mobility values in these two materials are comparable, the transport mechanisms in a-Se and in PbO are of a fundamentally different nature. In a-Se, the hole mobility depends strongly on both the electric field  $F$  and the temperature  $T$ . Conduction in a-Se occurs in the frame of the so-called multiple trapping (MT) model, in which carriers move via extended states above the mobility edge, being trapped into and released from the localized states in the band tail of the valence band. Hole transport is dispersive at low temperatures only, and turns non-dispersive at room temperature [26]. The dispersion observed at low temperatures is due to the multiple trapping into energetically distributed trapping states [35].

The most comprehensive and prominent mathematical description of the dispersive transport is based on the model of a continuous random walk of a charge carrier in a disordered material [36]. According to this picture, a carrier will be confronted with successively more and more difficult transitions in the course of its random motion, which would slow down the motion continuously, as described phenomenologically by equation (1). A microscopic transport mechanism behind this phenomenological treatment is to be clarified in each particular case depending on the experimentally observed features [32]. As has been shown by Pollak [37], the broad dispersion of transit times requires traps, which catch charge carriers within times much shorter than those needed to release carriers out of these traps. This can be reached in a system with a sufficiently broad energy distribution of traps since carriers can be trapped rapidly from the transport states into energetically deep traps where they spend a long time before they are released back into

transport states. Energy disorder has been identified in numerous organic (polymers) and inorganic (a-Si:H and a-Se) disordered materials as being responsible for the dispersive nature of charge transport. The energy distribution of traps in these materials leads to the broad distribution of the release times due to the exponential dependence of the release time on the trap energy [37]. As a result, mobility becomes temperature dependent.

In contrast, in the case of PbO, the hole mobility does not change significantly with  $T$ , while still depends strongly on  $F$  (see Fig. 2, 3). This temperature-independent behavior of the hole mobility rules out the MT as a possible transport mechanism in PbO. Indeed, if energy disorder would be responsible for charge transport providing, for instance, traps with energies below those corresponding to the transport path, rising  $T$  would enhance the release of carriers from the traps to the transport states and, concomitantly, it would increase the carrier mobility.

The same conclusion on the irrelevance of energy disorder for transport of holes in PbO can be reached by taking into account the observed independence of the dispersion parameter  $\alpha$  on temperature  $T$ . If energy disorder is responsible for the dispersive nature of charge transport, the dispersion parameter  $\alpha$  should be dependent on temperature [35, 37]. Therefore, the evidenced independence of the dispersion parameter  $\alpha$  on temperature in PbO in our study rules out energy disorder as a possible cause for the dispersive behavior of the hole mobility in this material.

In order to account for this temperature-independent dispersion parameter  $\alpha$ , one should then search for mechanisms based on spatial disorder. In contrast to the assumption by Scher and Montroll [36], hopping of carriers via randomly distributed isoenergetic sites would not lead to the broad dispersion of transient times at low electric fields, since carriers can always leave the traps as fast as they are captured [37]. At high electric fields, the situation is changed because the high

electric field prevents the release of carriers backwards with respect to the field direction and herewith restricts the random walk. If charge carriers cannot leave the areas, in which they are trapped by material inhomogenities at the time scale of capture processes, the charge transport can become dispersive, with the dispersion parameter independent of  $T$ .

Highly dispersive hole transport can be linked to the peculiarities of the polycrystalline structure of PbO layers. As it is seen in Fig. 6, the layer is a porous network of separate PbO platelets. Similar structure was previously repeatedly observed [17, 18, 21, 22, 38] indicating a highly reproducible PbO thermal deposition process. It is believed that, at the mesoscopic level, each platelet consists of weakly coupled Pb-O layers characterized by highly anisotropic hole transport [39 and references therein]. At this point, we can only speculate that a very unusual structural configuration of poly-PbO provides spatial inhomogeneity, responsible for highly dispersive hole transport. The inhomogeneous structure of the material could also be responsible for the observed reduced carrier recombination, compared with that in spatially homogeneous systems.

We would like to mention, that due to the requirements of large area deposition all photoconductors that have been investigated for use in direct conversion medical imaging detectors, have disordered structures. In addition to a-Se and PbO, selected examples are: polycrystalline layers of PbI<sub>2</sub> [40], HgI<sub>2</sub> [14] and CdZnTe [41]. All of them exhibit dispersive transport that is typical for disordered materials. Regardless of its nature (whether this is energy or spatial disorder that causes dispersion), dispersive transport is trap-limited and is characterized by low drift mobilities. As a result, the drift mobility  $\times$  lifetime product,  $\mu\tau$ , can be insufficient, causing the distance drifted by the carrier before it is trapped or recombined (the so-called carrier *schubweg*  $s = \mu\tau F$ ) to be shorter than the thickness of the photoconductive layer at practical electric fields. This results in incomplete charge collection, loss of detector sensitivity [42-45], degradation of signal-to-noise ratio and image blur

[19, 23]. Trapped charge will be eventually collected, though this contributes to the undesired image lag and deteriorates temporal performance. The above problems, however, do not mean that low mobility materials with dispersive transport cannot be used in imaging. A plausible approach to achieve “detector grade” polycrystalline photoconductor is to improve a carrier schubweg, by increasing the applied electric field while reducing dark current. This, in turn, requires development of special blocking contacts similar to how this was done for a-Se [1]. In such an approach, the fundamental problem of low mobility dispersive transport can be bypassed. Once schubweg exceeds the layer thickness, the X-ray generated charge is successfully collected, thus making a material suitable for applications in X-ray imaging. As for the particular case of the polycrystalline PbO, the strong dependence of hole drift mobility on the applied field facilitates the task of improving schubweg since it increases with  $F$  rapidly.

Our findings suggest a new direction towards optimization of the PbO technology, which has previously been focused on the improvement of the layer stoichiometry to increase mobility and  $\mu\tau$ . The latter approach may not be worth the effort since transport seems to be governed by spatial inhomogeneity of the PbO network, which is inherent to this material, rather than by a structure within a platelet.

## **Methods**

PbO layers were prepared from a high grade (5N) PbO powder using a thermal vacuum evaporation technique as reported elsewhere [17, 18]. The deposition takes place in the atmosphere of molecular oxygen at the partial pressure of  $\sim 4 \times 10^{-3}$  mbar. The PbO vapor condenses on ITO covered glasses in a form of platelets, which are several microns in diameter and about a hundred nanometers thick. The scanning electron micrograph of the grown layer is shown in Fig. 6. For mobility measurements, a metal contact (Au) 2 mm in diameter is deposited ex-situ on the PbO surface in a

different vacuum chamber. All experiments were performed on PbO layers with the thickness  $d = 5 \mu\text{m}$ .

The hole drift mobility, transport mechanism and recombination were characterized by conventional time-of-flight (TOF) and photo-CELIV measurements. TOF is known to be one of the major tools for direct determination of the charge transport mechanism [24]. In this technique charge carriers are generated by strongly absorbed light and their drift through the sample is caused by the external constant electric field. Since carriers are generated close to a sample surface, polarity of the applied bias governs the type of moving carriers. Carrier transit time,  $t_{tr}$ , is determined from the characteristic kink of the quasi-rectangular current transients. However, in non-crystalline materials with dispersive carrier transport, the shape of the current transient often deviates significantly from the ideal rectangular shape, making it difficult to measure carrier transit times.

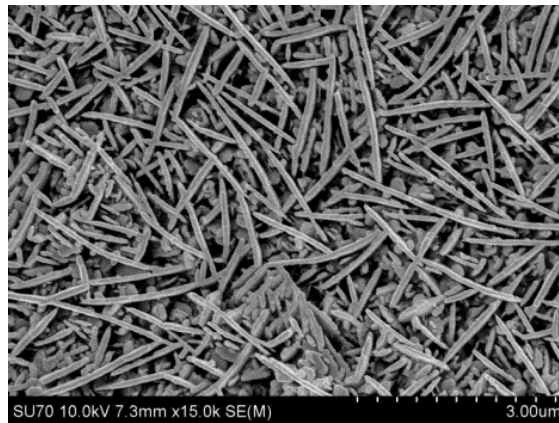


Figure 6. The SEM picture of the grown PbO layer.

Charge extraction by linear increasing voltage (photo-CELIV) has been proposed to overcome the problems associated with TOF measurements [25]. In photo-CELIV, charge carriers are photo-generated in unbiased sample. After a preset delay time, a linearly increasing voltage ramp is

applied to the sample in order to extract the photo-generated charge. As voltage increases, more carriers are extracted and the photocurrent rises. Once most of the carriers have been collected, the photocurrent decays. Mobility is derived from the time ( $t_{peak}$ ) needed to reach the peak of the photocurrent. The typical TOF and photo-CELIV experimental apparatuses are shown in Fig. 7a and Fig. 7b, respectively. For the TOF measurements, the charge carriers were generated by 35 ps laser pulses with the wavelength of 355 nm, while a constant bias was applied to the sample. The sample was irradiated from the ITO side, to which positive polarity was applied. For the photo-CELIV measurements, excitation wavelengths of 355 nm and 532 nm were used. For 355 nm, the attenuation depth in PbO is  $\sim 0.2 \mu\text{m}$  (i.e., light is absorbed close to the sample surface), while for 532 nm, the attenuation depth is  $\sim 17 \mu\text{m}$  [38], which provides uniform absorption for the sample thickness  $d = 5 \mu\text{m}$ . In order to investigate the temperature dependencies of the carrier mobility, the sample was placed in a cooling-heating stage, which allowed precise temperature control over a wide temperature range.

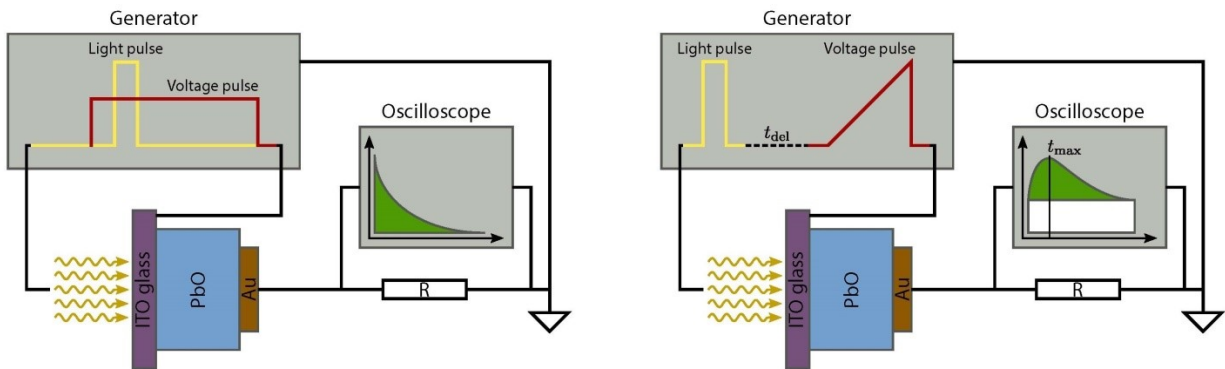


Figure 7. Schematic representation of the TOF (a) and photo-CELIV (b) apparatuses. The voltage from the generator was applied to the sample through the ITO contact. The signal was read out from the top (Au) contact and observed as a voltage drop on the oscilloscope resistance  $R$ .

## References

1. Bubon, O. et al. Electroded avalanche amorphous selenium (a-Se) photosensor. *Curr. Appl. Phys.* **12**, 983-9 (2012).
2. Abbaszadeh, S., Scott, C. C., Bubon, O., Reznik, A. & Karim, S. K. Enhanced detection efficiency of direct conversion X-ray detector using polyimide as hole-blocking layer. *Sci. Rep.* **3**, 3360 (2013).
3. Beutel, J., Kundel, H. L. & Van Metter, R. L. *Handbook of medical imaging* Vol.1 (eds Rowlands, J. A., Yorkstone, J.) Ch. 4, 223-328 (SPIE, 2000).
4. Destefano, N. & Mulato, M. Influence of multi-depositions on the final properties of thermally evaporated TlBr films. *Nucl. Instr. Meth. Phys. Res. A* **624**, 114-117 (2010).
5. Bennett, P. R. et al. Characterization of polycrystalline TlBr films for radiographic detectors. *IEEE Trans. Nucl. Sci.* **46**, 266-270 (1999).
6. Yun, M. S. et al. Investigation of PbI<sub>2</sub> film fabricated by a new sedimentation method as an X-ray conversion material. *Jpn. J. Appl. Phys.* **49**, 041801-041805 (2010).
7. Shah, K.S. et al. X-ray imaging with PbI<sub>2</sub>-based a-Si:H flat panel detectors. *Nucl. Instr. Meth. Phys. Res. A* **458**, 140-147 (2001).
8. Zhao, Q. et al. Performance evaluation of polycrystalline HgI<sub>2</sub> photoconductors for radiation therapy imaging. *Med. Phys.* **37**, 2738-2748 (2010).
9. Du, H. et al. Investigation of the signal behavior at diagnostic energies of prototype, direct detection, active matrix, flat-panel imagers incorporating polycrystalline HgI<sub>2</sub>. *Phys. Med. Biol.* **53**, 1325-1351 (2008).

10. Zentai, G., Partain, L. & Pavlyuchkova, R. Dark current and DQE improvements of mercuric iodide medical imagers. *Proc. SPIE Med. Imag.* **6510**, 65100Q (2007).
11. Kim, K. et al. Quantitative evaluation of mercuric iodide thick film for X-ray imaging device. *Proc. SPIE Med. Imag.* **6142**, 61422Z (2006).
12. Zuck, A., Schieber M., Khakhan, O. & Burshtein, Z. Near single-crystal electrical properties of polycrystalline HgI<sub>2</sub> produced by physical vapor deposition. *IEEE Trans. Nucl. Sci.* **50**, 991-997 (2003).
13. Iwanczyk, J. S. et al. HgI<sub>2</sub> polycrystalline films for digital X-ray imagers. *IEEE Trans. Nucl. Sci.* **49**, 160-164 (2002).
14. Street, R. A. et al. Comparison of PbI<sub>2</sub> and HgI<sub>2</sub> for direct detection active matrix X-ray image sensors. *J. Appl. Phys.* **91**, 3345-3355 (2002).
15. Tokuda, S., Kishihara, H., Adachi, S. & Sato, T. Improvement of temporal response and output uniformity of polycrystalline CdZnTe films for high-sensitivity X-ray imaging. *Proc. SPIE* **5030**, 861-870 (2003).
16. Tokuda, S., Kishihara, H., Adachi, S. & Sato, T. Preparation and characterization of polycrystalline CdZnTe films for large-area, high-sensitivity X-ray detectors. *J. Mat. Sci.: Mat. Elec.* **15**, 1-8 (2004).
17. Simon, M. et al. PbO as direct conversion X-ray detector material. *Proc. SPIE* **5368**, 188-199 (2004).

18. Simon, M. et al. Analysis of lead oxide (PbO) layers for direct conversion X-ray detection. *IEEE Trans. Nucl. Sci.* **52**, 2035-2040 (2005).
19. Kasap, S. O. et al. Amorphous and Polycrystalline Photoconductors for Direct Conversion Flat Panel X-Ray Image Sensors. *Sensors* **11**, 5112-5157 (2010).
20. Keezer, R. C., Bowman, D. L. & Becker, J. H. Electrical and Optical Properties of Lead Oxide Single Crystals. *J. Appl. Phys.* **39**, 2062-2066 (1968).
21. Van den Broek, J. Physical interpretation of a PbO-photodetector. *Solid State Commun.* **4**, 295-297 (1966).
22. Schottmiller, J. C. Photoconductivity in tetragonal and orthorhombic Lead Monoxide layers. *J. Appl. Phys.* **37**, 3505-3510 (1966).
23. Kabir, M. Z. Effects of charge carrier trapping on polycrystalline PbO X-ray imaging detectors, *J. Appl. Phys.* **104**, 074506 (2008).
24. Haber, K. S. & Albrecht, A. C. Time-of-flight technique for mobility measurements in the condensed phase. *J. Phys. Chem.* **88**, 6025-6030 (1984).
25. Juska, G., Arlauskas, K. & Viliunas, M. Extraction Current Transients: New Method of Study of Charge Transport in Microcrystalline Silicon. *Phys. Rev. Lett.* **84**, 4946-4949 (2000).
26. Mott, N. F. & Davis, E. A. *Electronic processes in non-crystalline materials* Ch. 6, 199-319 (Clarendon, 1979).
27. Nekrasas, N., Genevicius, K., Viliunas, M. & Juska, G. Features of current transients of photogenerated charge carriers, extracted by linearly increased voltage. *Chem. Phys.* **404**, 56-59 (2012).

28. Lorrmann, J., Badada, B. H., Inganäs, O., Dyakonov, V. & Deibel, C. Charge carrier extraction by linearly increasing voltage: Analytic framework and ambipolar transients. *J. Appl. Phys.* **108**, 113705 (2010).
29. Juska, G., Nekrasas, N., Valentinavicius, V., Meredith, P. & Privrikas, A. Extraction of photogenerated charge carriers by linearly increasing voltage in the case of Langevin recombination. *Phys. Rev. B* **84**, 155202 (2011).
30. Schubert, M. et al. Mobility relaxation and electron trapping in a donor/acceptor copolymer. *Phys. Rev. B* **87**, 024203 (2013).
31. Hanfland, R., Fischer, M. A., Brütting, W., Würfel, U. & MacKenzie, R. C. I. The physical meaning of charge extraction by linearly increasing voltage transients from organic solar cells. *Appl. Phys. Lett.* **103**, 063904 (2013).
32. Pope, M. & Swenberg, C. E. *Electronic processes in organic crystals and polymers 2-nd edn.* Ch. 3 (Oxford, 1999).
33. Nenashev, A. V. et al. Role of diffusion in two-dimensional bimolecular recombination. *Appl. Phys. Lett.* **96**, 213304 (2010).
34. Privrikas, A., Philippa, B., White, R. D. & Juska, G. Photocarrier lifetime and recombination losses in photovoltaic systems. *Nature Photonics* **10**, 282-283 (2016).
35. Baranovskii, S. D. & Rubel, O. *Charge Transport in Disordered Solids with Applications in Electronics* (ed. Baranovskii, S. D.) Ch. 2, 49-96 (John Wiley & Sons, 2006).
36. Scher, H. & Montroll, E.W. Anomalous transit-time dispersion in amorphous solids. *Phys. Rev. B.* **12**, 2455-2477 (1975).
37. Pollak, M. On dispersive transport by hopping and by trapping. *Phil. Mag.* **36**, 1157-1178 (1977).

38. Biberman, L. M. & Nudelman, S. *Photoelectronic imaging devices* Vol. 2 (eds Stupp, E. H., Levitt, R. S.) Ch. 14, 275-300 (Plenum, 1971).
39. Berashevich, J., Semeniuk, O., Rowlands, J. A. & Reznik, A. Anisotropy of the carrier effective masses in bulk  $\alpha$ -PbO. *EPL* **99**, 47005 (2012).
40. Street, R. A. et al. Electronic transport in polycrystalline PbI<sub>2</sub> films. *J. Appl. Phys.* **86**, 2660-2667 (1999).
41. Kim, K. H. et al. Characterization of high-resistivity poly-CdZnTe thick films grown by thermal evaporation method. *IEEE Trans. Nucl. Sci.* **51**, 3094-3097 (2004).
42. Nemirovsky, Y. Statistical modeling of charge collection in semiconductor gamma-ray spectrometers. *J. Appl. Phys.* **85**, 8-15 (1999).
43. Kasap, S. O. X-ray sensitivity of photoconductors: application to stabilized a-Se. *J. Phys. D: Appl. Phys.* **33**, 2853-2865 (2000).
44. Kabir, M. Z. & Kasap, S. O. Charge collection and absorption-limited sensitivity of X-ray photconductors: applications to a-Se and Hgl<sub>2</sub>. *Appl. Phys. Lett.* **80**, 1664-1666 (2002).
45. Kim, H. K. Analytical model for incomplete signal generation in semiconductor detectors. *Appl. Phys. Lett.* **88**, 132112 (2006).

## Acknowledgement

The authors are thankful to Dr. Matthias Simon, Philips Research Labs, for help in optimization of the PbO growth process. The financial support from the National Science and Engineering Research Council (NSERC), Canadian Institute for Health Research (CIHR) and Ontario Research Fund–Research Excellence (ORF-RE) program and that of the Deutsche Forschungsgemeinschaft (GRK 1782) is gratefully acknowledged.

### **Author contributions**

O. S. deposited experimental PbO samples, performed CELIV experiments and drafted the manuscript text. G. J. extended the CELIV theory to cover the dispersive transport. J.-O. O. prepared all figures. M. W., S. D. B. and A. R. analyzed the obtained results in terms of spatial disorder linked to the peculiarities of the PbO structure. S. D. B. and A. R. edited the manuscript text. All authors reviewed the manuscript.

### **Additional information**

There are no competing financial interests.

### **3. 2. Electron transport in poly-PbO**

This topic has been elaborated in the following publication: O. Semeniuk, G. Juska, J. -O. Oelerich, S. D. Baranovskii & A. Reznik “Transport of electrons in Lead Oxide studied by CELIV technique”, published in *Journal of Physics D: Applied Physics*, Volume 50, Issue 3, 035103 (2016). The full text of the publication is listed below.

# Transport of electrons in Lead Oxide studied by CELIV technique

O Semeniuk<sup>1,2\*</sup>, G Juska<sup>3</sup>, J O Oelerich<sup>4</sup>, K Jandieri<sup>4</sup>, S D Baranovskii<sup>4</sup> and A Reznik<sup>2,5</sup>

<sup>1.</sup> Chemistry and material science program, Lakehead University, 955 Oliver Road, Thunder Bay, ON, Canada P7B 5E1

<sup>2.</sup> Advanced detection devices department, Thunder Bay Regional Research Institute, 980 Oliver Road, Thunder Bay, ON Canada P7B 6V4

<sup>3.</sup> Department of Solid State Electronics, Vilnius University, Saulėtekio 9 III k., 10222 Vilnius, Lithuania

<sup>4.</sup> Faculty of Physics, Philipps Universität Marburg, D-35032 Marburg, Germany

<sup>5.</sup> Department of Physics, Lakehead University, 955 Oliver Road, Thunder Bay, ON, Canada P7B 5E1

\*e-mail: [osemeniu@lakeheadu.ca](mailto:osemeniu@lakeheadu.ca)

Short title (running heads): Transport of electrons in Lead Oxide studied by CELIV technique

Keywords: Polycrystalline Lead Oxide (poly-PbO), photoconductor, photo-CELIV, electron mobility, dispersive transport.

## **Abstract**

Although polycrystalline lead oxide (PbO) has a long history of applications in optoelectronics and imaging, the transport mechanism for electrons in this material has not yet been clarified. Using the photo-generated charge extraction by linear increasing voltage (photo-CELIV) technique, we provide the temperature- and field-dependences of the electron mobility in poly-PbO. It is found that electrons undergo dispersive transport, i.e. their mobility decreases in the course of time. Multiple trapping of electrons from the conduction band into the developed band tail is revealed as dominant transport mechanism. This differs dramatically from the dispersive transport of holes in the same material, dominated by topological factors and not by energy disorder.

## **1. Introduction**

Polycrystalline Lead Oxides (PbO) is of high interest for numerous applications including large area photovoltaic [1] and photodetecting devices [2-7]. Several reports are available, which describe the crystalline structure, bonding and the photoconducting behavior of different lead oxides [5,8-17]. However, the transport properties of electrons in poly-PbO are not yet clarified, although these properties are decisive for practical utilization of the material. Only recently the features of hole transport in poly-PbO has been revealed [18]. The hole mobility was reported to be  $\sim 0.1 \text{ cm}^2/\text{Vs}$ , which is comparable to that of a-Se – the only commercial competitor to PbO for use in direct conversion X-ray medical imaging detectors. It was shown that hole transport is highly dispersive, which is attributed to spatial inhomogeneity of the PbO layers [18]. As for the electron transport, to the best of our knowledge, the only available data are on the mobility-lifetime ( $\mu_e \tau_e$ ) product, derived from the X-ray-generated current [3] or from the photoconductivity measurements [5,8]. It should be noted that the published results on  $\mu_e \tau_e$  scatter significantly. This is not

surprising since the photocarrier lifetime  $\tau$  in disordered structures is not a material parameter but rather a characteristic of a device and it can vary significantly depending on the experimental conditions and the experimental technique used [19]. It is well established now that objective characterization of transport properties requires direct measurements of the carrier drift mobility  $\mu$ . However, in disordered structures the precise mobility evaluation is very challenging [19]. Indeed, the time-of-flight (TOF) technique, known as the major tool for direct measurements of the carrier mobility in wide band-gap photoconductors [20] was proven inefficient [18] to study the transport properties of holes in poly-PbO. This is due to the dispersive nature of hole transport [18], that blurs a packet of photo-generated carriers so that transit time (the basis for the mobility measurement in TOF technique) cannot be measured. Therefore, other experimental methods than the TOF technique should be searched for in order to investigate charge transport in disordered materials.

In the early 2000's, an alternative to TOF technique called charge extraction by linearly increasing voltage (CELIV) has been proposed [21]. We have recently extended CELIV theory to account for the dispersive transport and showed on the example of holes in PbO, that photo-CELIV provides a reliable tool for measuring mobilities in highly dispersive media [18]. In the current manuscript, we apply this method to study electron transport in PbO in a wide range of temperatures and electric fields.

## 2. Methods

### 2.1. Sample preparation

The poly-PbO layers were prepared by conventional thermal evaporation technique as described elsewhere [2,3,9]. The pure (5N) PbO powder was evaporated from the Pt crucible at

~1000-1100 °C in the atmosphere of molecular oxygen. The evaporated particles of PbO condense on the ITO covered glass substrate kept at ~ 100 °C. This provides the growth rate of ~ 1 μm/min. PbO layers with thickness  $d = 5 \mu\text{m}$  were used in our experiments. A top Au contact ~200 nm thick was deposited *ex situ* in the dedicated chamber.

The poly-PbO films grow in a form of platelets, which are about a micron in diameter and about fifty nanometers thick [3]. The platelets are oriented mainly parallel to the growth direction and are randomly arranged within a plane. As a result, the structure has high porosity of ~50 %. The scanning electron micrograph of the grown layer is shown in figure 1. Raman spectroscopy indicates that the platelets are composed of the highly crystalline material with predominance of tetragonal phase in the bulk [17].

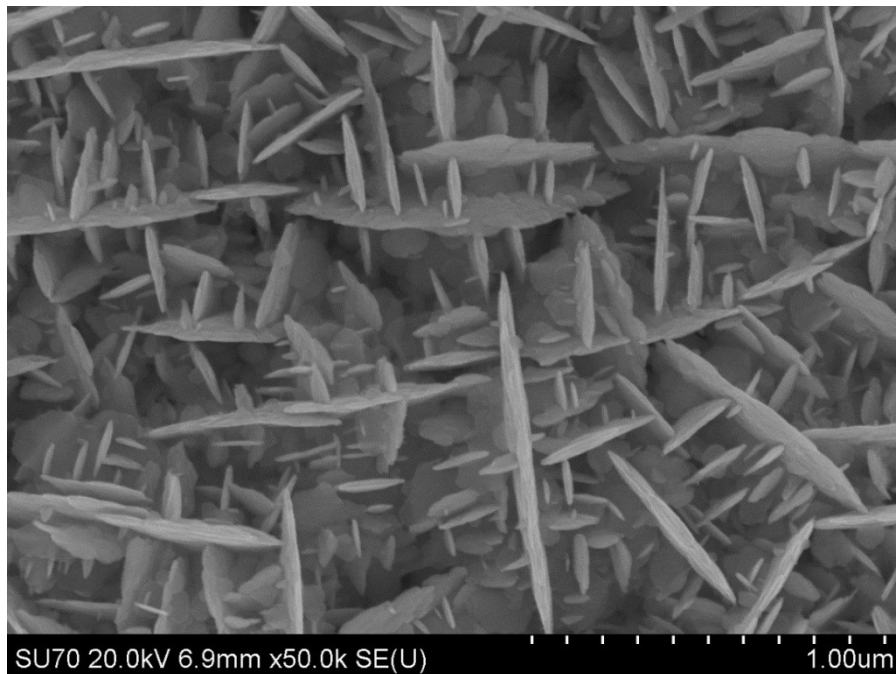


Figure 1. The scanning electron micrograph of the of the poly-PbO layer.

## 2.2. Experimental techniques

The electron drift mobility and the transport mechanism were characterized by a photo-CELIV technique. In photo-CELIV, a light pulse is used to generate charge carriers in an unbiased sample. Subsequently, in order to extract the photo-generated carriers, a linearly increasing voltage is applied to the sample. As applied voltage increases, the photocurrent rises as more carriers are extracted. At the end of the extraction, when most carriers have been collected, the photocurrent decays. The carrier mobility is derived from the time of the peak photocurrent  $t_{peak}$ . The typical photo-CELIV experimental apparatus is shown in figure 2. For the photo-CELIV measurements the charge carriers were generated by 35 ps laser pulses with the excitation wavelength of 532 nm that provided uniform absorption. Indeed, for wavelength of 532 nm the attenuation depth in poly-PbO is  $\sim 17 \mu\text{m}$  [7]. Thus, when the sample was irradiated from the ITO side, the charge carriers were uniformly photo-generated throughout the sample, as required for accurate CELIV results [22]. The linearly increasing voltage ramp  $A = dU/dt$  was applied to ITO contact via the generator Tektronix AFG3022C and amplifier Tegan 2340. The range of voltage ramp  $A$  between  $5 \times 10^5$  to  $2 \times 10^8$  V/s was selected to observe the extraction of slow electrons. Such range of  $A$  was obtained by fixing the applied voltage to  $U=200$  V and varying the voltage pulse duration between  $4 \times 10^{-4}$  to  $1 \times 10^{-6}$  s. The photocurrent transients were observed on the oscilloscope Tektronix TDS 2024C. All measurements were performed with the positive polarity applied to the ITO. Reversing polarity, i.e. application of negative polarity on ITO, did not affect the extraction of photo-generated charge carriers. On the other hand, reverse polarity resulted in strong increase of the dark current, which diminished the visibility of CELIV photo-peak and thus was not practical for characterization of transport properties. In order to investigate the temperature dependences of the carrier mobility, the sample was placed in a LINKAM LTS350 cooling-heating stage, which allowed a precise temperature stabilization and control in a wide temperature range.

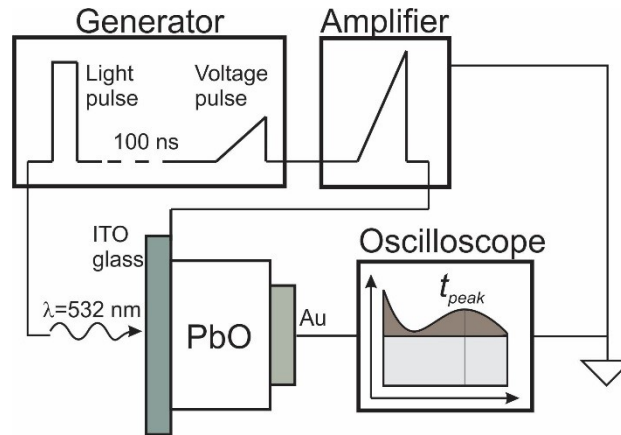


Figure 2. Schematic representation of the photo-CELIV.

### 3. Results

The typical photo-CELIV signal is shown in figure 3. When uniformly absorbed light is used, two CELIV photo peaks are observed. Initially, the photocurrent rises rapidly until most of faster carriers have been extracted. After this, photocurrent starts to decay. As electric field further increases, the extraction of slower carrier begins and photocurrent rises again. Once most of the slower carriers have been extracted, the photocurrent drops, approaching the value of the capacitive signal.

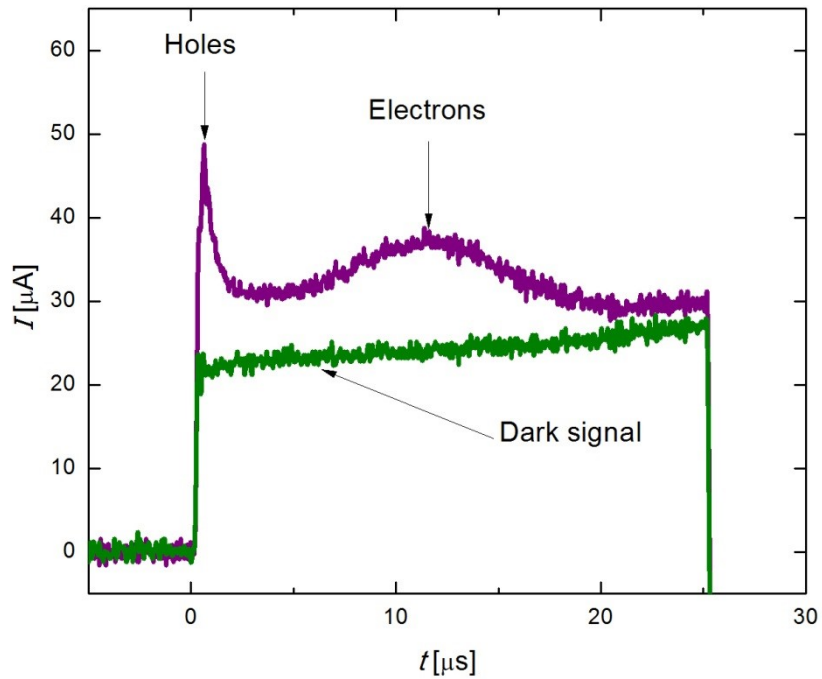


Figure 3. Photo-CELIV signal corresponding to extraction of photo-generated charge carriers.

Previously it was shown that holes are faster carriers in poly-PbO [18]. Thus, the first peak of the photocurrent is caused by the drift of holes, and the second peak is related to slower electrons. For the chosen range of  $A$ , the extraction of holes occurs at the beginning of the voltage ramp (i.e. at low applied voltages) and terminates well before the beginning of the electron extraction. Therefore, extraction of holes is separated from the extraction of slow electrons and these two processes do not interfere.

According to Ref [18] in the case of dispersive transport when carriers are photo-generated in the bulk of the sample, the mobility can be derived as:

$$\mu = \frac{a(a+1)}{2a+1} \frac{d^2}{t_{peak}^2 A}, \quad (1)$$

where dispersive parameter  $\alpha$  is calculated from the dependence of  $t_{peak}$  on voltage ramp  $A$  [18]:

$$t_{peak} \sim A^{-\frac{1}{1+\alpha}}, \quad (2)$$

In order to elucidate the transport mechanism for electrons in poly-PbO, the measurements were performed at different temperatures between 243 K and 363 K. In figure 4,  $t_{peak}$  is plotted as a function of the voltage ramp  $A$ . In accord with equation (2), if plotted in the double logarithmic scale, the slope of  $\log(t_{peak})$  vs  $\log(A)$  curve yields the dispersion parameter  $\alpha$ . The inset in figure 4 shows that  $\alpha$  changes linearly with temperature from  $\sim 0.2$  at 243 K to  $\sim 0.9$  at 363 K.

The electron mobility is calculated from  $t_{peak}$  according to equation (1) and is plotted in figure 5 as a function of applied field ( $F$ ) for different temperatures. As seen from figure 5, the electron mobility strongly depends on both  $F$  and  $T$ : the lower the temperature, the more pronounced is the field dependence. At the same time, a stronger temperature dependence is observed at lower applied electric fields: at comparatively low  $F = 10$  V/ $\mu\text{m}$  the change in temperature by 100 K alters the mobility by more than two orders of magnitude.

The electron mobility follows Arrhenius dependence for all electric fields used in our experiments. For the selected field  $F = 20$  V/ $\mu\text{m}$  the electron mobility, plotted as a function of inverse temperature, is shown in figure 6. It follows Arrhenius dependence yielding activation energy  $E_a = 0.45$  eV.

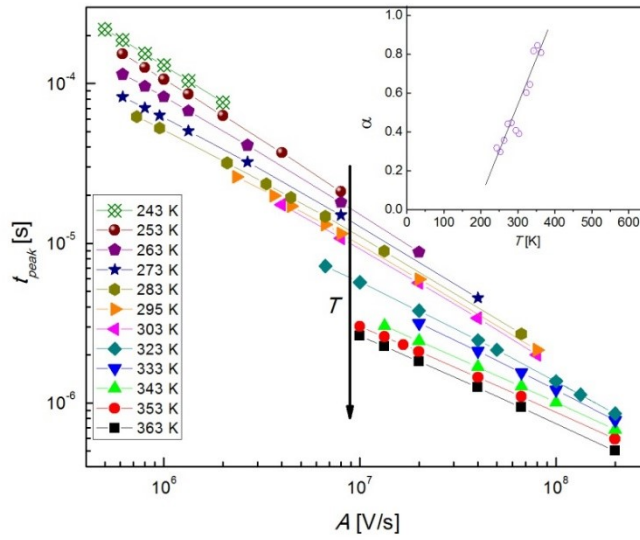


Figure 4.  $t_{peak}$  is plotted for different temperatures  $T$  as a function of voltage ramp  $A$ .

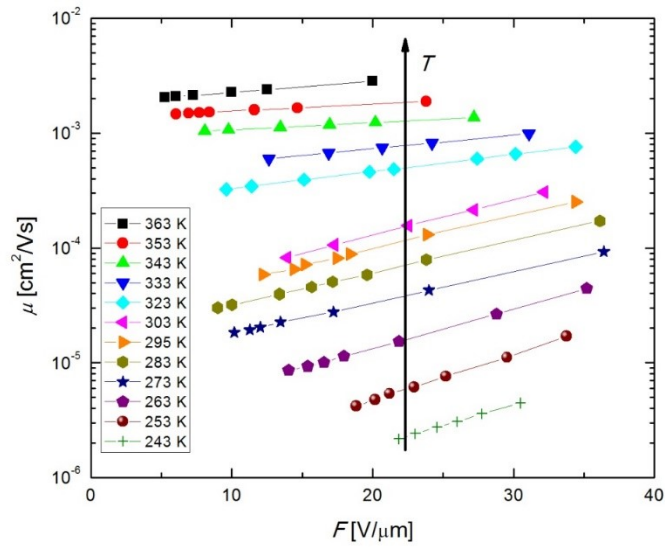


Figure 5. Electron mobility is plotted for different temperatures as a function of applied electric field. Since in CELIV technique the electric field changes with time, mobility values were calculated for electric field  $F$ , determined from the voltage ramp  $A$  and  $t_{peak}$  as:  $F = \frac{A \cdot t_{peak}}{d}$ . The size of the symbols reflects the error bars due to the mobility variation as a result of surface roughness (the surface roughness is  $\sim 400$  nm for  $5 \mu\text{m}$  thick poly-PbO sample).

#### 4. Discussion

The Arrhenius temperature dependence of the electron mobility along with its low values, high activation energy and the dispersive nature of the charge transport points at the multiple-trapping (MT) mechanism as responsible for transport of electrons in poly-PbO. The MT model has been developed to describe charge transport in disordered materials, such as chalcogenide glasses and amorphous silicon [23-26], which possess a mobility edge, i.e., the energy level that separates extended states with rather high carrier mobility from the localized states, which can be considered as traps. The latter states form the so-called band tail in the mobility gap. In the MT model, a charge carrier moves with a microscopic mobility  $\mu_0$  only via delocalized states with energies above the mobility edge. This motion is interrupted by trapping into localized tail states with subsequent activation of the carriers back into the conducting states above the mobility edge. As a result, overall carrier transit is characterized by the effective drift mobility  $\mu$  that in the case of local trapping level depends on trapping and release times as:

$$\mu = \mu_0 \frac{\tau_{free}}{\tau_{trap} + \tau_{free}} \quad (3)$$

where  $\tau_{free}$  is a trapping time, and  $\tau_{trap}$  is a temperature-dependent release time:  $\tau_{trap} \sim e^{E_a/kT}$ , that provides Arrhenius behavior for the drift mobility described by equation (3), when  $\tau_{trap} \gg \tau_{free}$ .

MT model has been described in the literature in all details by semi-phenomenological approaches [27,28] as well as by exact analytical equations for various shapes of the energy spectrum in the band tail under equilibrium and non-equilibrium conditions [29-31].

Assuming MT as the dominant mechanism for electron transport, we extrapolated mobility values shown in figure 5 to zero field, and re-plotted in figure 6 thus obtaining the electron drift

mobility  $\mu$  as a function of inverse temperature. It follows the Arrhenius dependence with larger activation energy  $E_a^0 = 0.55$  eV than that for the drift mobility at  $F = 20$  V/ $\mu\text{m}$  ( $E_a = 0.45$  eV).

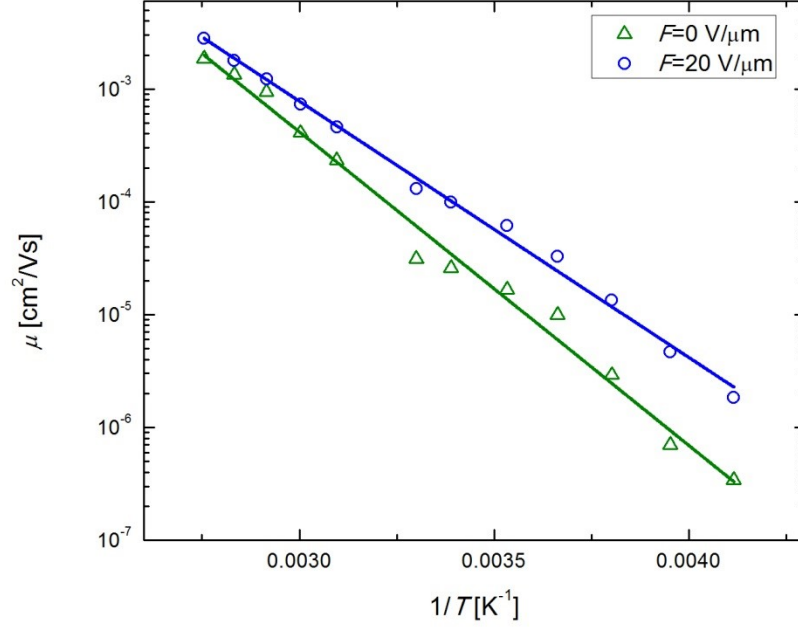


Figure 6. Mobility of electrons as a function of temperature for selected electric fields:  $F = 20$  V/ $\mu\text{m}$  and estimated for  $F = 0$ .

For the exponential distribution of traps in the band tail with characteristic energy scale  $E_0$ ,

$$N(E) = N_0 \exp\left(-\frac{E}{E_0}\right), \quad (4)$$

the MT model predicts the temperature dependence of the dispersion parameter  $\alpha$  in the form [27,28]:

$$\alpha = kT/E_0. \quad (5)$$

If such temperature dependence of the dispersion parameter  $\alpha$  was observed, this would allow one to estimate  $E_0$  and subsequently the density of states below the conduction band edge. The insert to figure 4 evidences a strong temperature dependence of  $\alpha$ , though not literally in the form

of equation (5). Such a steep temperature dependence of the dispersion parameter is often observed in disordered materials, in which charge transport is dominated by multiple trapping of carriers into the band tail states [26]. According to numerical simulations, this behavior suggests that real materials often possess some significant structure in the energy distribution of localized states, rather than containing a featureless tail of traps [26]. We do not want to speculate here about the diagnostics of the density of states in the band tail and restrict our message to the claim that the strong temperature dependence of the electron mobility along with the dispersive nature of charge transport characterized by the temperature-dependent dispersion parameter  $\alpha$  point at the dominating role of the energy disorder for electron transport and concomitantly at the multiple trapping mechanism as the most probable model to account for the observed transport features.

The established MT transport mechanism for electrons in poly-PbO is drastically different from the transport mechanism for holes in the same material as revealed recently by photo-CELIV technique [18]. While transport of holes has also a dispersive nature with mobility decreasing in the course of time, the characteristic features of the hole transport in poly-PbO are essentially temperature-independent [18]. This means that the mobility dispersion for holes is not related to the energy disorder but rather is caused by topological factors [18]. On the contrary, electron mobility is conditioned by the energy disorder as evidenced by the strong temperature dependence of the electron mobility (figure 5) and that of the dispersion parameter (inset to figure 4).

## 5. Conclusions

Mobility of electrons in poly-PbO has been studied experimentally using the photo-CELIV technique. Arrhenius temperature dependence of the carrier mobility along with the dispersive nature of the charge transport characterized by the temperature-dependent dispersion parameter

evidences the multiple-trapping mechanism as responsible for transport of electrons in poly-PbO. Electrons move via delocalized state above the mobility edge being trapped into and released from the traps in the band tail below the mobility edge.

### **Acknowledgement**

The financial support from the National Science and Engineering Research Council (NSERC), Canadian Institute for Health Research (CIHR), Ontario Research Fund–Research Excellence (ORF-RE) program, Research Council of Lithuania (grant MIP-091/2015) and that of the Deutsche Forschungsgemeinschaft (GRK 1782) is gratefully acknowledged.

### **Author contributions**

O. S. deposited PbO samples, performed experiments and processed CELIV results with CELIV theory developed by G. J. O.S. drafted the manuscript text. J.-O. O. prepared all figures. K. J., S. D. B. and A. R. analyzed the obtained results in terms of energetic disorder. S. D. B. and A. R. edited the manuscript text. All authors reviewed the manuscript.

### **References**

- [1] Droessler L M, Assender H E and Watt A A R 2012 Thermally deposited lead oxides for thin film photovoltaics *Mater. Lett.* **71**, 51-53
- [2] Simon M, Ford R A, Franklin A R, Grabowski S P, Mensor B, Much G, Nascetti A, Overdick M, Powell M J and Wiechert D U 2004 PbO as direct conversion X-ray detector material *Proc. SPIE* **5368** 188-199

- [3] Simon M, Ford R A, Franklin A R, Grabowski S P, Mensor B, Much G, Nascetti A, Overdick M, Powell M J and Wiechert D U 2005 Analysis of lead oxide (PbO) layers for direct conversion X-ray detection *IEEE Trans. Nucl. Sci.* **52** 2035-40
- [4] Kasap S et al 2010 Amorphous and polycrystalline photoconductors for direct conversion flat panel X-ray image sensors *Sensors* **11** 5112-57
- [5] Van den Broek J 1966 Physical interpretation of a PbO-photodetector *Solid State Commun.* **4** 295-297
- [6] Kabir M Z 2008 Effects of charge carrier trapping on polycrystalline PbO X-ray imaging detectors *J. Appl. Phys.* **104** 074506
- [7] Biberman L M and Nudelman S 1971 *Photoelectronic Imaging Devices* (New York: Plenum Press) ch. 14
- [8] Schottmiller J C 1966 Photoconductivity in tetragonal and orthorhombic lead monoxide layers *J. Appl. Phys.* **37** 3505-10
- [9] Berashevich J, Semeniuk O, Rowlands J A and Reznik A 2012 Anisotropy of the carrier effective masses in bulk  $\alpha$ -PbO *EPL* **99** 47005
- [10] Venkataraj S, Geurts J, Weis H, Kappertz O, Njoroge W K, Jayavel R and Wuttig M 2001 Structural and optical properties of thin lead oxide films produced by reactive direct current magnetron sputtering *J. Vac. Sci. Technol. A* **19**, 2870-2878
- [11] Trinquier G and Hoffmann R 1984 Lead Monoxide: Electronic Structure and Bonding *J. Phys. Chem.* **88**, 6696-6711
- [12] Watson G W, Parker S C and Kresse G 1999 *Ab initio* calculation of the origin of the distortion of  $\alpha$ -PbO *Phys. Rev. B* **59**, 8481-8486

- [13] Hughes C and Sokel A J 1981 Computation of photoconductivity in insulators in the space charge and recombination regime. Application to PbO films *J. Appl. Phys.* **52**, 6743-6748
- [14] Terpstra H J, de Groot R A and Haas C 1995 Electronic structure of the lead monoxides: bond structure calculations and photoelectron spectra *Phys. Rev. B* **52**, 11690-11697
- [15] Bordovsku G A, Gordeev M L, Ermoshkin A N, Izvozhikov V A and Evarestov R A 1982 Energy Band Structure of Rhombic Lead Monoxide *Phys. Stat. Sol. (b)* **111**, K123-K127
- [16] Berashevich J, Semeniuk O, Rubel O, Rowlands J A and Reznik A 2003 Lead monoxide a-PbO: electronic properties and point defect formation *J. Phys.: Condens. Matter* **25**, 075803
- [17] Wiechert D U, Grabowski S P and Simon M 2005 Raman spectroscopic investigation of evaporated PbO layers *Thin Solid Films* **484**, 73-82
- [18] Semeniuk O, Juska G, Oelerich J -O, Wiemer M, Baranovskii S D and Reznik A 2016 Charge transport mechanism in lead oxide revealed by CELIV technique *Sci. Rep.* accepted for publication (2016).
- [19] Privrikas A, Philippa B, White R D and Juska G 2016 Photocarrier lifetime and recombination losses in photovoltaic systems *Nature Photonics* **10**, 282-283
- [20] Haber K S and Albrecht A C 1984 Time-of-flight technique for mobility measurements in the condensed phase *J. Phys. Chem.* **88(24)** 6025-30
- [21] Juska G, Arlauskas K and Viliunas M 2000 Extraction current transients: new method of study of charge transport in microcrystalline silicon *Phys. Rev. Lett.* **84** 4946-49
- [22] Nekrasas N, Genevicius K, Viliunas M and Juska G 2012 Features of current transients of photogenerated charge carriers, extracted by linearly increased voltage *Chem. Phys.* **404** 56-59
- [23] Noolandi J 1977 Multiple-trapping model of anomalous transit-time dispersion in a-Se *Phys. Rev. B* **16**, 4466-4473

- [24] Schmidlin F W 1977 Theory of trap-controlled transient photoconduction *Phys. Rev. B* **16**, 2362-2385
- [25] Silver M and Cohen L 1977 Monte Carlo simulation of anomalous transit-time dispersion of amorphous solids *Phys. Rev. B* **15**, 3276-3278
- [26] Marshall J M 1983 Carrier diffusion in amorphous semiconductors *Rep. Prog. Phys.* **46**, 1235-1282
- [27] Tiedje T and Rose A 1980 A physical interpretation of dispersive transport in disordered semiconductors *Solid. State. Commun.* **37**, 49-52
- [28] Orenstein J and Kastner M A 1981 Thermalization and recombination in amorphous semiconductors *Solid State Commun.* **40**, 85-89
- [29] Rudenko A I and Arkhipov V I 1982 Drift and diffusion in materials with traps. I. Quasi-equilibrium transport regime *Phil. Mag. B* **45** 177-187
- [30] Arkhipov V I and Rudenko A I 1982 Drift and diffusion in materials with traps. II. Non-equilibrium transport regime *Phil. Mag. B* **45**, 189-207
- [31] Nenashev V, Jansson F, Baranovskii S D, Osterbacka R, Dvurechenskii A V and Gebhard F 2010 Effect of electric field on diffusion in disordered materials. II. Two- and three-dimensional hopping transport *Phys. Rev. B* **81**, 115204

## **Chapter 4: Investigation of structural properties of PbO layers**

This topic has been elaborated in the following publication: O. Semeniuk, A. Csik, S. Kökényesi & A. Reznik “Ion-Assisted Deposition of Amorphous PbO Layers”, published in *Journal of Materials Science*, Volume 52, Issue 13, pp. 7937–7946 (2017). The full text of the publication is listed below.

# Ion-Assisted Deposition of Amorphous PbO Layers

O. Semeniuk<sup>1,2\*</sup>, A. Csik<sup>3</sup>, S. Kökényesi<sup>4</sup>, A. Reznik<sup>2,5</sup>

<sup>1</sup> Chemistry and materials science program, Lakehead University, 955 Oliver Road, Thunder Bay, ON, Canada P7B 5E1

<sup>2</sup> Advanced detection devices department, Thunder Bay Regional Health Research Institute, 290 Munro Street, Thunder Bay, ON Canada P7A 7T1

<sup>3</sup> Institute for Nuclear Research, Hungarian Academy of Sciences, Bem tér 18/c, P.O. Box 51, H-4001, Debrecen, Hungary

<sup>4</sup> Institute of Physics, University of Debrecen, H-4026, Bem sq.18/a, Debrecen, Hungary

<sup>5</sup> Department of Physics, Lakehead University, 955 Oliver Road, Thunder Bay, ON, Canada P7B 5E1

\*Corresponding author.

*E-mail address:* [osemeniu@lakeheadu.ca](mailto:osemeniu@lakeheadu.ca) (O. Semeniuk).

## Abstract

Lead oxide (PbO) is one of the most promising materials for application in direct conversion medical imaging X-ray detectors. Despite its high potential, conventional polycrystalline PbO layers deposited with the basic thermal evaporation method are not yet mature for practical use in x-ray imaging; indeed, they are highly porous, unstable at ambient conditions, and sub-stoichiometric. In order to combat the above issues with PbO, we advance the basic evaporation process with simultaneous energetic ion bombardment of the growing film. We show that tuning the ion-assisted thermal deposition not only solves the structural problems of poly-PbO, but also enables the growth of a new non-crystalline polymorphic form of the material - amorphous PbO (a-PbO). In contrast to poly-PbO, novel a-PbO layers grown by ion-assisted thermal deposition are stable at ambient conditions. Structural and morphological analysis confirms that a-PbO is stoichiometric and free of detectable voids, which suggests higher bulk X-ray stopping power than porous poly-PbO.

*Keywords:* Oxide-film growth kinetics, phase transformation, polycrystals, amorphous.

## Introduction

There is great interest in the utilization of non-crystalline photoconductors for direct conversion medical X-ray imaging detectors. Lead Oxide (PbO) is one of the most promising candidates for this purpose, since it has high stopping power due to high atomic number of Pb and has high theoretical X-ray-to-charge conversion gain. In addition, poly-PbO room temperature deposition technology allows the deposition of a thick photoconductive layer directly on any imaging electronics, thus permitting a custom PbO detector design to fit the requirements of a variety of clinical applications.

Conventional poly-PbO layers are deposited by basic thermal evaporation in the atmosphere of molecular oxygen from a crucible loaded with high purity PbO powder and heated above PbO melting temperature  $T_{melt} \sim 890$  °C [1]. For use in the direct conversion x-ray detectors, the PbO layer has to be deposited on a substrate containing image read-out electronics [2]. In this case the substrate temperature is maintained at  $T_{sub} \sim 100$  °C as dictated by thermal tolerance of the majority of commercial read-out electronics [3]. The large mismatch between the substrate temperatures  $T_{sub}$  and the melting temperature of PbO  $T_{melt}$  results in low packing density and high porosity of grown layers [4,5]: the density of as-grown poly-PbO layers is much lower than that of a crystalline material (up to 50 % of single crystal density), which significantly decreases the X-ray attenuation of the grown film. A typical poly-PbO layer is composed of randomly oriented platelets about one micron in diameter and one hundred nanometers thick and exhibits a rough surface morphology [1,6]. The grown PbO films are known to consist of two different crystallographic phases of PbO: the seeding layer, several microns thick, is formed by the yellow orthorhombic  $\beta$ -PbO, while the bulk of the layer grows predominately as a red tetragonal lead oxide ( $\alpha$ -PbO), however,  $\beta$ -PbO is also present in the bulk [7]. In addition, the grown layers are substoichiometric with a deficit of oxygen [8-10]. The latter is due to the low formation energy of oxygen vacancies [10,11] which can act as charge trapping centers – a highly undesirable feature for any detector material. Poly-PbO layers are unstable in air and transform into Hyrdo Cerrusite under ambient conditions [12].

Suboptimal packing density, poor sample stability and oxygen deficiency are well known problems of many oxides deposited with basic thermal or electron beam evaporation techniques. These issues were successfully combated by means of simultaneous bombardment of growing film

with energetic ions. Here, a practical and easy to implement way of obtaining energetic ions is by utilization of a specially designed ion source during the deposition process [4,13].

The ion assisted depositions have proven to be a versatile tool for solving a broad range of material science challenges. Initially this method was employed to improve the basic properties of metal oxides, including packing density [14-17] and stoichiometry [18,19]. Nowadays, ion assisted deposition is successfully applied to advance the growth of organic transistors and polymers-based electronic devices [20-22]. In addition, ion assisted deposition is used as an alternative to high pressure and/or high temperature deposition technique of crystalline and epitaxial materials [23,24].

Motivated by the success of ion-assisted deposition to improve structure and stability of other materials, we applied this technique to PbO layers growth. The structural characterization performed with Raman spectroscopy, X-ray diffraction (XRD) and X-ray Photoelectron Spectroscopy (XPS), and morphological examinations with Scanning Electron Microscopy (SEM) revealed a new polymorphic form of PbO – an amorphous (a-PbO) material that appeared to be dense and stable at ambient conditions. a-PbO samples are free of voids, possess bulk packing density, and have perfect stoichiometry throughout the film thickness as will be shown below.

## **Materials and Methods**

### *Polycrystalline PbO (poly-PbO) sample preparation*

Poly-PbO layers were prepared by conventional thermal evaporation of PbO powder as shown in Fig. 1 (a). A Pt crucible, containing pure (5N) PbO powder obtained commercially from Chemsavers, is loaded into the furnace (evaporation source) of the vacuum chamber. Typically, the evaporation takes place at temperature  $\sim 1000$  °C which provides a growth rate  $\sim 1$   $\mu\text{m}/\text{min}$ . The evaporated particles of PbO (vapor stream) condense on the rotating substrate that is kept at  $\sim 100^\circ$

C. In order to improve the layer stoichiometry, the deposition takes place under  $\sim 0.2$  Pa background pressure of high purity molecular oxygen, which is directly supplied to the vacuum chamber [1,11].

#### *Amorphous PbO (a-PbO) sample preparation*

a-PbO layers were prepared by thermal evaporation with low energy oxygen ion bombardment. The key difference from the conventional deposition described above, is that the deposition takes place in the atmosphere of *ionized oxygen*, instead of molecular oxygen. This is achieved by running molecular oxygen through an ion source placed at  $\sim 10$  cm below the substrate holder with a beam incidence angle of  $\sim 45^\circ$  to the normal of the substrate as shown in Fig. 1 (b). In our system, the ion source utilizes a hot filament to produce electrons. Electrons are accelerated by the applied electric field which is towards the anode of the ion source where they bombard  $O_2$  introduced into the ion source body, producing oxygen ions [18]. The ion source allows for independent control of oxygen ion energy and ion flux (ion current density), required to achieve the desired structural modifications of a growing layer. Thus, during the typical ion assisted deposition, the ion energy was between 40-60 eV, while the ion flux was  $\sim 0.2$  mA/cm<sup>2</sup>. The substrate and evaporation source temperatures were similar to those of the conventional thermal evaporation, resulting in the deposition rate of a-PbO  $\sim 0.4$   $\mu\text{m}/\text{min}$ .

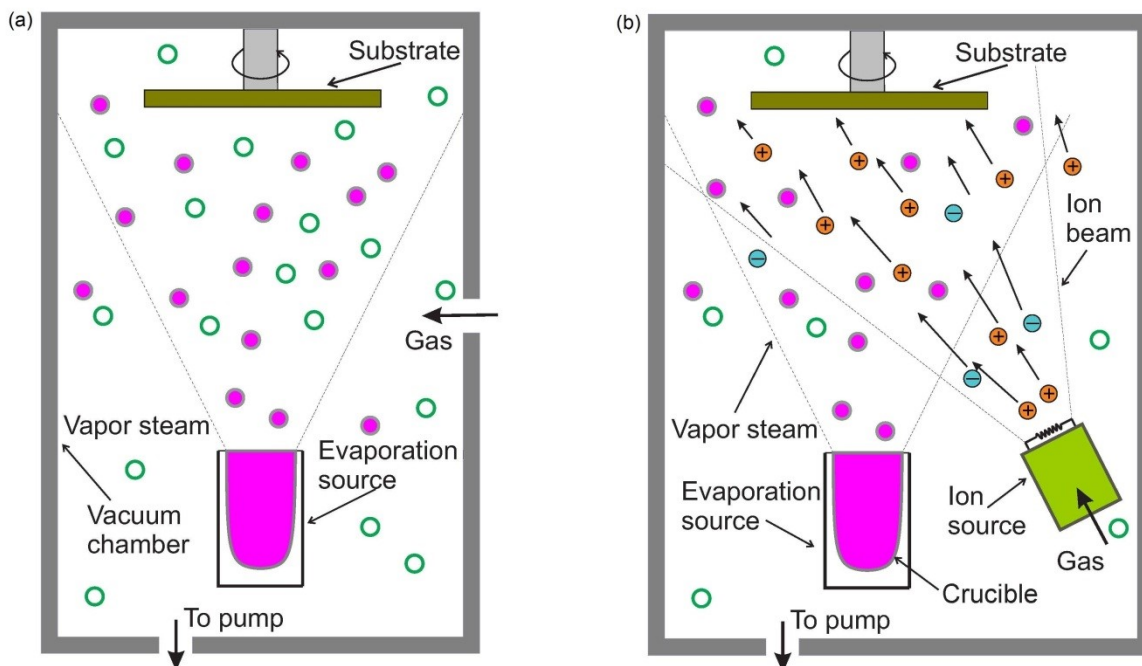


Figure 1 (a) Schematic description of the conventional deposition process. Process gas (oxygen) is supplied directly to the chamber. (b) Schematic description of advanced deposition process. Oxygen is supplied to the chamber through an ion source.

### *Sample characterization*

The structural and morphological analyses of poly- and a-PbO samples were performed with Raman, X-Ray diffraction (XRD) and X-ray Photoelectron Spectroscopy (XPS) and Scanning Electron Microscopy (SEM).

Since poly-PbO samples are known to transform into Hydro Cerrisite under ambient conditions, they were stored under the protective dry nitrogen atmosphere. They were exposed to ambient only for the time of the Raman spectrum acquisition and when the sample was relocated from one measurement system to the other. This maximal exposure time (during Raman spectroscopy) did not exceed 10 minutes, therefore no structural changes were observed. During XRD measurement, the samples were under continuous argon gas purge. XPS measurement was

done in high vacuum conditions (base pressure  $\sim 5 \times 10^{-6}$  Pa). One poly-PbO sample was stored under ambient conditions and was used as a reference. In order to establish stability of novel a-PbO layers, they were stored under ambient conditions.

#### *Raman and XRD spectroscopies.*

Raman spectroscopy measurements were performed with a Renishaw inVia Raman spectrometer with resolution of  $\sim 1$   $\text{cm}^{-1}$ . The Raman spectra were measured with an Ar ion laser, using the 785-nm laser line at 1200 lp/mm mesh. Prior to the measurements, the system was calibrated to silicon peak at  $520$   $\text{cm}^{-1}$ . The intensity level was carefully adjusted in order to prevent light induced changes, which was especially important for a-PbO samples.

XRD spectroscopy was performed with a Pananalytical Expert Pro Diffractometer and the X-ray source was  $\text{CuK}\alpha$  radiation with wavelength  $0.15405$  nm. The typical X-ray diffraction pattern was recorded from  $2\theta = 20^\circ$  to  $90^\circ$  with the scan step size of  $0.01313^\circ$ . The phase identification was achieved by the comparison with data from the JCPDS International diffraction data base.

For a-PbO samples, Raman and XRD measurements were performed on both, as-grown layers and layers undergoing one hour annealing in a temperature range from  $200$  to  $600$   $^\circ\text{C}$ . After annealing at each temperature, the sample was slowly cooled down with the rate of  $\sim 1$   $^\circ\text{C}/\text{min}$  in order to prevent thermal shock. After the XRD and Raman measurements were performed on the cooled sample, it was moved back to the oven for the annealing at a subsequent temperature. The upper temperature limit was dictated by thermal stability of the glass substrate. The annealing took place in the argon atmosphere in order to prevent over-oxidation of the samples.

#### *XPS spectroscopy*

Stoichiometry of poly- and amorphous PbO layers have been investigated by X-Ray Photoelectron Spectroscopy (XPS). The XPS spectra of PbO layers were investigated with a PHOIBOS 100 analyzer (SPECS GmbH, Berlin) equipped with Al X-Ray source. The NIST XPS Database [25] was used for peak identification and CasaXPS software was used for deconvolution and fitting of Pb 4f and O 1s peaks. Carbon (C 1s) peak with binding energy of 284.5 eV was used as a reference for calibration of energy.

In order to investigate any changes in-depth of the sample, the tested films were sputtered in-situ in a Secondary Neutral Mass Spectrometry (SNMS) [26] chamber connected to the XPS. Thus, the first XPS spectrum was recorded on the original surface (as-prepared) of the sample and afterwards the sample was moved into the SNMS chamber (base pressure 0.2 mPa) for sputtering with Ar<sup>+</sup> ion bombardment. After each sputtering the new XPS spectrum was recorded and the sample was moved back into the SNMS chamber for the next sputtering process. The lateral homogeneity of ion bombardment was checked by measuring the shape of the sputtered crater at the end of the experiment with an AMBIOS XP-1 type profilometer. A profilometer was also used to determine the sputtering rate by measuring both the crater depth and sputtering time. The poly-PbO sample was sputtered for 120, 420, 1020 and 1620 seconds, which correspond to 140, 510, 1250 and 1950 nm sputter depths, respectively. Similarly, a-PbO was sputtered for 60, 360, 960 and 1860 seconds, corresponding to 15, 87, 232 and 450 nm sputter depths.

Due to the high resistivity of PbO samples, a large charge accumulation effect occurred on the sputtered surface as a result of Ar<sup>+</sup> ion bombardment during the sputtering process. In order to account for this sample charging effect, the SNMS was operated in the High Frequency (HF) operation mode (at 100 kHz with 50% duty cycle), when a square-wave type high frequency voltage is applied to the sample instead of a constant DC voltage [27,28]. This operation mode

allows neutralization of the positive charge accumulated on the surface during ion bombardment periods.

## Results

### *Morphological analysis*

A SEM micrograph of the surface of the poly-PbO prepared with conventional deposition method, is shown in Fig. 2 (a). As seen from Fig. 2 (a), poly- PbO film consists of a network of platelets, each less than 2 microns in diameter and about 50 nm thick. On the film surface, platelets are seen to be oriented primarily in the growth direction (although arbitrary relative to each other). This platelet structure is highly porous and results in high surface roughness, which is on the range of a micrometer, as defined by the size of the platelets. It should be noted that the morphology of poly-PbO layers grown here is very similar to that reported previously by Simon et al. [1] suggesting high reproducibility of the basic thermal evaporation process.

Fig. 2 (b) shows the SEM picture of the amorphous PbO. The film is seen to be uniform, free from voids and does not exhibit a platelet structure typical of poly-PbO. The absence of a platelet network results in a smooth surface of the grown layer, never achieved before with polycrystalline films.

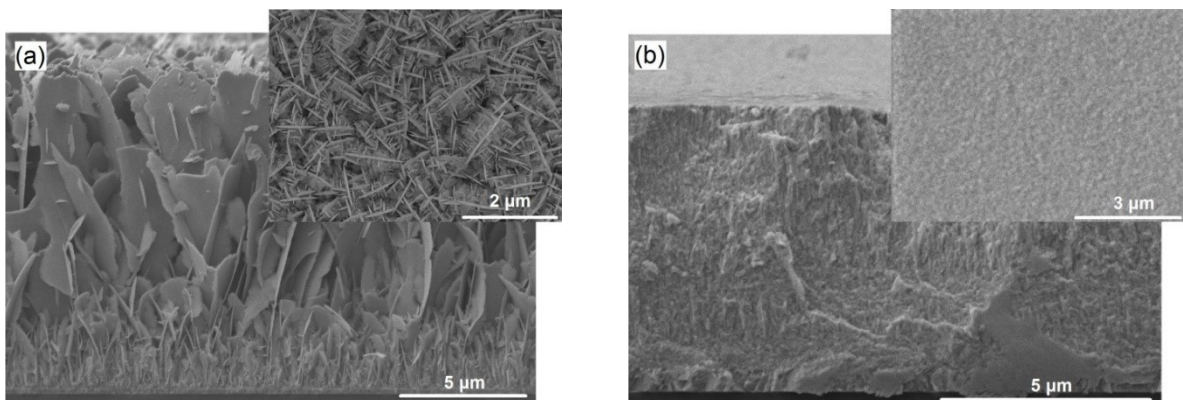


Figure 2 (a) The SEM cross-sectional view of the poly-PbO. The inset to the figure shows the surface of the poly-PbO layer. (b) SEM cross-sectional view of the a-PbO. The inset to the figure shows the surface of the a-PbO layer.

### *Raman spectroscopy*

Fig. 3 (a) compares Raman spectra of as-deposited poly- and a-PbO films. The Raman spectrum of poly-PbO indicates the presence of both phases: tetragonal  $\alpha$ -PbO peaks at 81 and 340  $\text{cm}^{-1}$  and  $\beta$ -PbO peaks at 89 and 289  $\text{cm}^{-1}$ . The Raman peak at  $\sim 146 \text{ cm}^{-1}$  cannot be unambiguously attributed to either phase, since both of them have the strongest signal in this region:  $\alpha$ -PbO at 145  $\text{cm}^{-1}$  and  $\beta$ -PbO at 147  $\text{cm}^{-1}$ .

Since the poly-PbO sample was stored under protective atmosphere of dry nitrogen, no Hydro Cerrisite peaks were detected. However, another poly-PbO sample from the same deposition run which was kept at ambient conditions developed a Hydro Cerrisite peak at 1050  $\text{cm}^{-1}$  on the Raman spectrum.

Overall, the measured Raman spectrum of poly-PbO is represented by high and relatively narrow peaks, indicating crystalline structure of the deposited layers. In contrast, Raman spectrum of novel PbO is very different. It is represented by wide peaks and a high plateau typical to amorphous structure.

Fig. 3 (b) shows gradual changes in Raman spectra of a-PbO following one hour annealing at four different annealing temperatures. As is clear from Fig. 3 (b), the a-PbO layer undergoes gradual re-crystallization, evident from the characteristic peaks which evolve from a broad spectrum. At 200 °C, crystallization begins with the formation of the peaks at 85, 143 and 288  $\text{cm}^{-1}$ ; in the temperature range from 200 °C to 300 °C these peaks grow gradually and become well defined at 300 °C. These peaks are close to those of the  $\beta$ -PbO phase [7]. At 400 °C, another characteristic  $\beta$ -PbO peak appears at 71  $\text{cm}^{-1}$ , as well as additional peak at 121, 224, 391 and 548  $\text{cm}^{-1}$  attributed to  $\text{Pb}_3\text{O}_4$  [7]. Upon annealing to 600 °C, most of the former peaks have disappeared. All peaks at 600 °C are attributed to orthorhombic PbO.

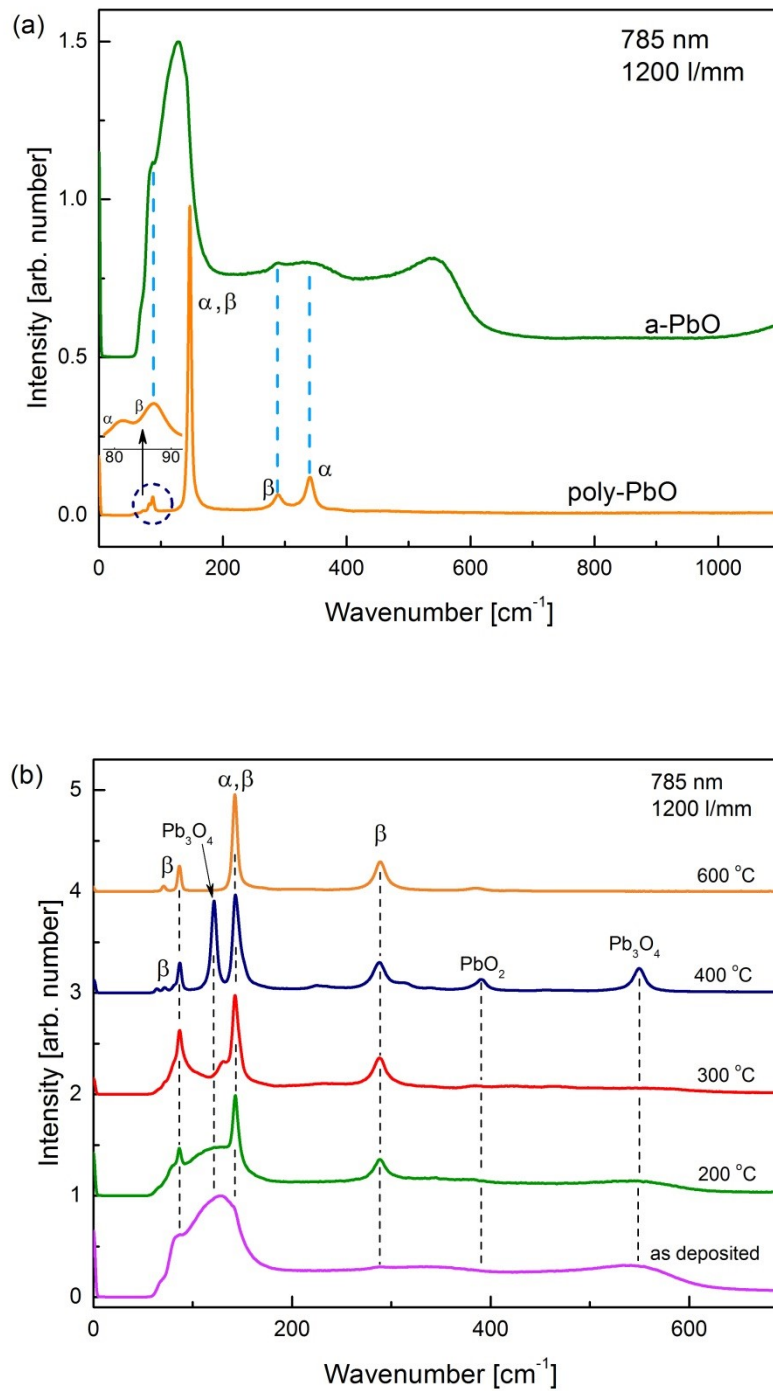


Figure 3 (a) Raman spectra of as deposited poly- and a-PbO. (b) Raman spectra of a-PbO layers after one hour annealing at the four temperatures indicated. Note: All spectra were measured on the surface of the films.

The spectra showed in Fig. 3 were normalized and shifted upwards for better visualization, however it is worth mentioning, that with higher temperature the peaks become taller and narrower. At the

same time plateaus decrease with increasing temperature, indicating refinement of the crystal structure.

It should be noted that a-PbO samples did not require a special protective environment. Thus, the Raman spectra of the a-PbO samples stored at ambient conditions persisted over time and did not show any features of Hydro Cerrusite.

#### *XRD spectroscopy*

The XRD spectra of as-grown poly- and a-PbO films are shown in Fig. 4 (a). While the XRD spectrum of poly-PbO is represented by sharp, well defined characteristic peaks, indicative of crystalline ordered structure, the XRD of a-PbO does not exhibit distinct narrow peaks indicating its amorphous nature.

X-Ray diffraction measurements of the poly-PbO sample reveal the presence of both tetragonal and orthorhombic phase of PbO, as well as an orthorhombic PbO<sub>2</sub> phase, which was not observed on Raman spectrum. This might be due to the fact that the sensitivity of the XRD measurements is higher than that of Raman spectroscopy. As for the a-PbO layer, its amorphous structure changes dramatically upon annealing (Fig. 4 (b)). The effect of annealing starts to appear at 200 °C, although very insignificantly. At higher temperatures, characteristic peaks emerge from a broad spectrum. A gradual refinement of the crystal structure is further observed: width of the emerged peaks decreases and their intensity increases with increasing temperature. At temperatures above of 300 °C, multiple phases of PbO were found to coexist simultaneously:  $\alpha$ ,  $\beta$ -PbO, Pb<sub>3</sub>O<sub>4</sub> and PbO<sub>2</sub>. However, at 600 °C, the spectrum closely resembling a single phase of orthorhombic PbO with a minor peak of PbO<sub>2</sub> detected.

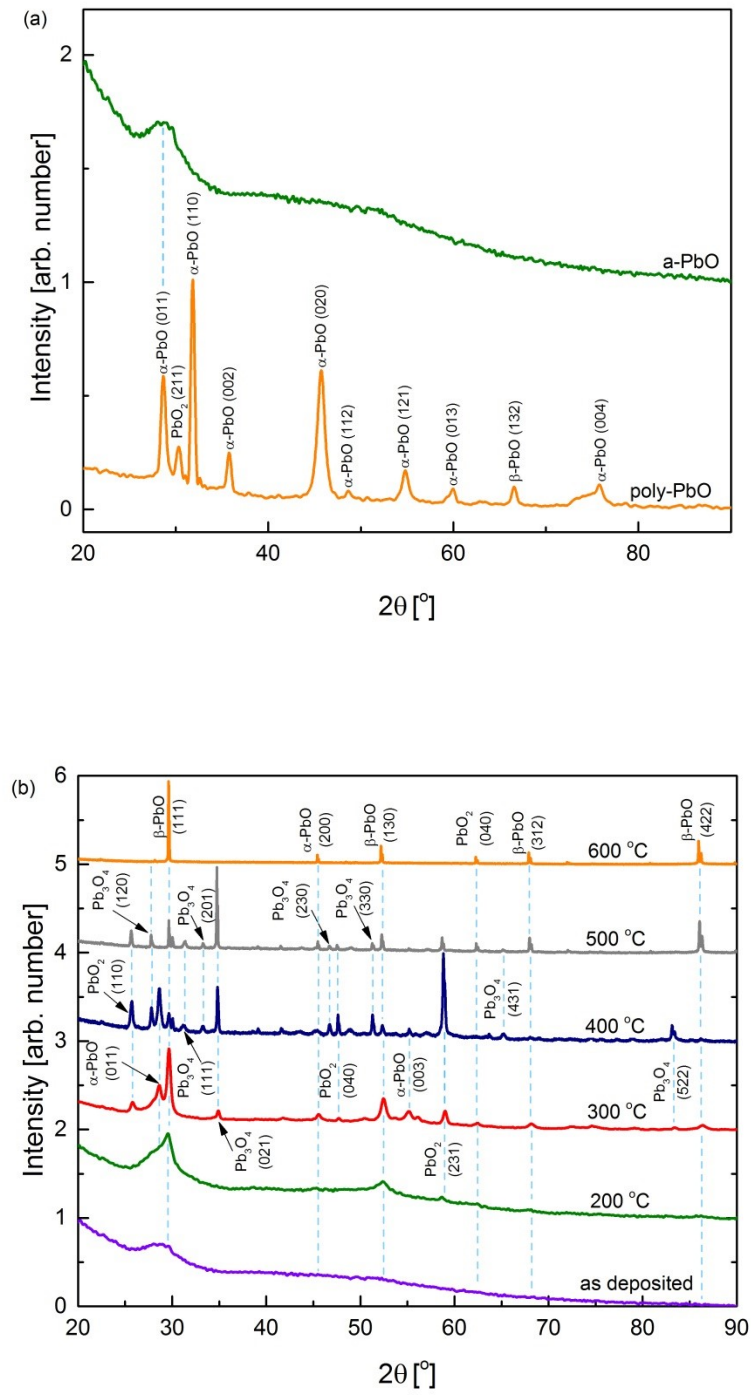
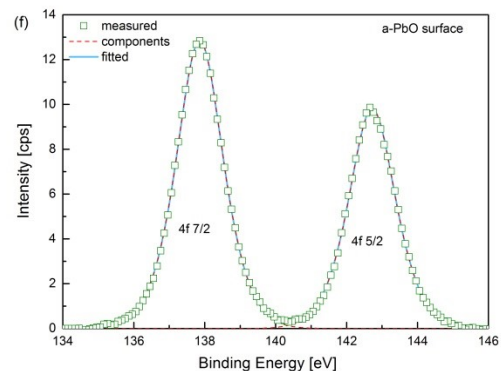
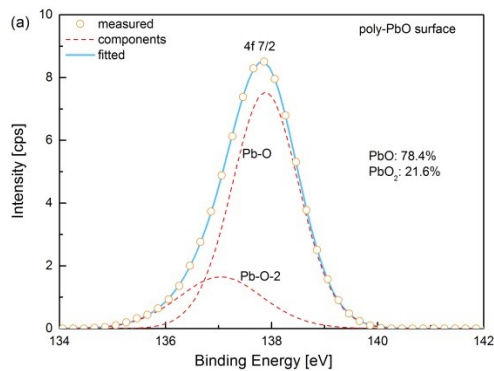


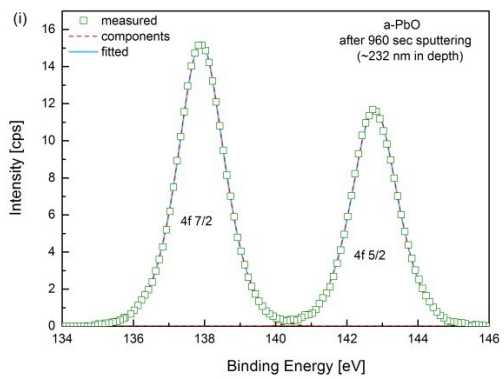
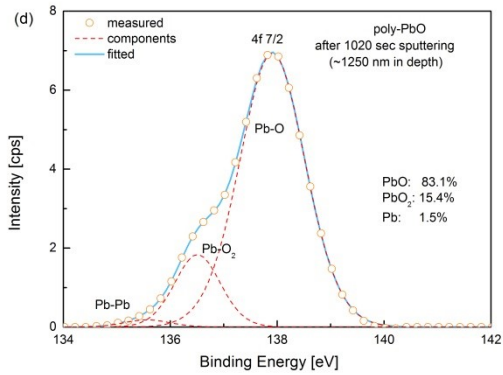
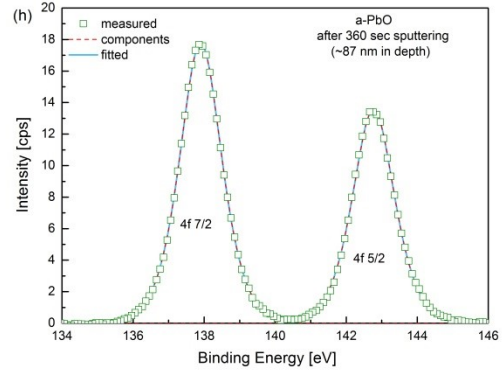
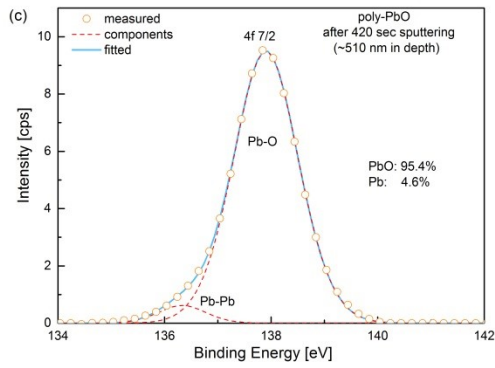
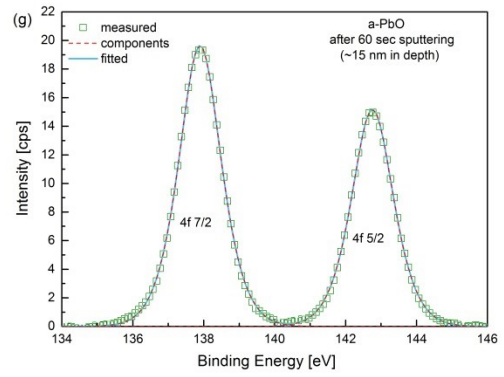
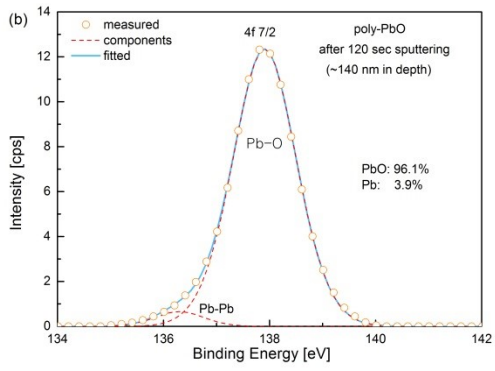
Figure 4 (a). The XRD spectra of as-grown poly- and a-PbO films. (b) The XRD spectra of as deposited amorphous PbO layer as well as the same layer annealed at five different temperatures for one hour. The spectra were measured on the surface of the films.

### XPS spectroscopy

Fig. 5 (a) shows the XPS spectra of the poly-PbO sample measured on the surface and in the bulk of the sample. The surface measurements indicate the presence of both PbO and PbO<sub>2</sub> phases. The PbO<sub>2</sub> peak disappears when measurements are taken at 140 nm in depth, however, a small amount of metal Pb phase is seen to be present in the spectrum. Spectra measured at a depth of 510 nm closely resemble that of 140 nm. However, with further sputtering, an additional contribution of pure PbO<sub>2</sub> appears in the measurements, while Pb-O remains the dominant bonding configuration.

Fig. 5 (b) shows the XPS spectra of a-PbO measured on the surface and after sputtering in SNMS system. As can be seen from the presented spectra, the composition of the film remains constant across the layer thickness: only lead-oxide (PbO) without any other elements or oxides of lead (e.g. PbO<sub>2</sub>) was detected.





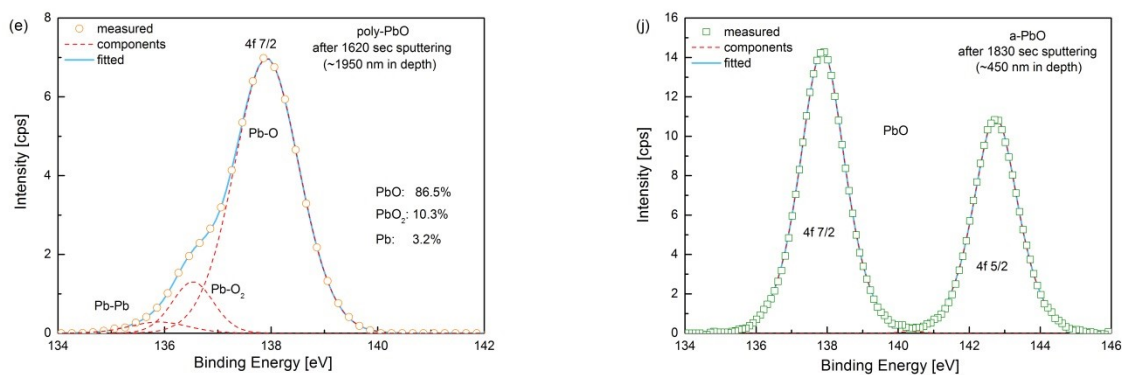


Figure 5 (a-e) XPS spectra of poly-PbO and (f-g) a-PbO at selected depths.

## Discussion

Morphological and structural properties of PbO layers deposited with both basic thermal evaporation and ion-assisted thermal evaporation were investigated with multiple characterization techniques, including SEM, Raman spectroscopy, XRD and XPS. While Raman and XRD measurements were taken on the layers' surfaces, XPS spectra were measured at different depths, monitoring stoichiometry and composition across the layers.

Qualitatively, all the measurements taken confirm that while basic thermal evaporation results in polycrystalline structure of the grown layers, oxygen ion bombardment with optimized ion energy and flow results in a new polymorphic form of the grown material, namely, amorphous Lead Oxide (a-PbO) not synthesized before. In contrast to the poly-PbO, a-PbO is uniform, free of voids and does not require special storage conditions to prevent structural degradation. In addition, morphological analysis of PbO layers indicates that novel a-PbO layers possess a significantly higher packing density, in comparison with poly-PbO (see Fig. 2). Improved density and absence of voids in the layer offers a high bulk X-ray stopping power – one of the main advantages of PbO for direct conversion X-ray detectors.

Although amorphous PbO is stable at ambient conditions, it is (as expected) fundamentally metastable with respect to the crystalline structure and undergoes gradual crystallization toward orthorhombic PbO at elevated temperatures as shown with XRD and Raman measurements after different stages of thermal annealing. This property is reminiscent of another amorphous material which is highly significant to radiation medical imaging, namely, amorphous selenium (a-Se) – currently the only wide-bandgap photoconductor used commercially in the direct conversion detectors for low x-ray energy clinical applications (i.e., in x-ray mammography). In comparison to a-Se, a-PbO structural stability is much higher: the first a-PbO layers deposited two years ago and stored in air did not degrade and do not show any changes in both Raman and XRD spectra. This is an advantage over a-Se, since the latter requires special doping for stabilization against recrystallization at ambient conditions, while un-stabilized pure a-Se structurally degrades in approximately one month after the deposition [29,30].

Perfect structural uniformity and stoichiometry of a-PbO layers is evident from the XPS analysis performed at different depths below the layer surface. In contrast, poly-PbO is over-oxidized at the surface while showing a certain deficit of oxygen in the bulk (as this is demonstrated by the presence of un-oxidized Pb in XPS spectra shown in Fig. 5 (a)). Oxygen deficiency is known to be a common problem of all metal oxides, since oxygen molecules are electrically neutral and thus do not react deliberately with other elements. Therefore, in order to promote incorporation of oxygen in the growing film, this charge neutrality must be distorted. Here, utilization of an ion source was a natural way of solving the oxygen deficiency problem. Indeed, the ion source ionizes oxygen, converting it to a charged state and thus making it more reactive. As a result of such an ion assisted deposition stoichiometric PbO layers were received for the first time ever (see Fig. 5 (b)).

Overall, optimization of the ion assisted thermal deposition process allows one to grow amorphous PbO layers – a new polymorphic configuration free of structural imperfections inherent to more common polycrystalline PbO. The improvement includes higher film density and much better uniformity, stoichiometry and stability against structural changes. The amorphous PbO deposition process is compatible with large area x-ray detector technologies. As such, an amorphous PbO x-ray-to-charge transducer should be considered as an alternative to a-Se for x-ray medical detectors in the diagnostic energy range where a-Se is suboptimal due to its low atomic number. Although comprehensive research on a-PbO electronic and photoconductive properties is needed, the reported results are very promising to extend the advances of direct conversion x-ray medical imaging over a variety of imaging procedures including radiography, fluoroscopy, pediatric imaging, etc. In addition, new a-PbO can also be considered for applications in large area photovoltaic devices [31], solar cell [32] and light emitting diodes [33], where electronic properties of PbO were shown to significantly improve the device performance.

## **Conclusion**

We propose advanced deposition process for PbO that allows one to obtain a new polymorphic form of this material - amorphous lead oxide, as confirmed with Raman and XRD spectroscopies. In contrast to poly-PbO, a-PbO samples are stable at ambient environment and perfectly stoichiometric. In addition, SEM indicates that new a-PbO layers have bulk packing density, which offers high X-ray stopping power. Proposed advances in the deposition technology are easy to implement and hold the promise to utilize the full potential of PbO in medical imaging X-ray detectors as well as many other applications.

## **Acknowledgement**

The authors are thankful to Dr. Matthias Simon, Philips Research Labs and Prof. Kai Wang, Joint Institute of Engineering at Carnegie Mellon University for help in optimization of the PbO growth process. The authors gratefully acknowledge the financial support from the National Science and Engineering Research Council (NSERC), Canadian Institute for Health Research (CIHR) and Ontario Research Fund–Research Excellence (ORF-RE) program. Also, this publication is supported by the GINOP-2.3.2-15-2016-00041 project. The project is co-financed by the European Union and the European Regional Development Fund. Support by the TAMOP 4.2.2.A-11/1/KONV-2012-0036 project, which is co-financed by the European Union and European Social Fund, is also acknowledged.

## **Author contributions**

O. S. deposited experimental polycrystalline and amorphous PbO samples, performed sample characterization with SEM, XRD, Raman spectroscopy and drafted the manuscript text. A.C. performed XPS characterization of the samples. S. K. and A. R. edited the manuscript text. All authors reviewed the manuscript.

**Conflict of Interest:** The authors declare that they have no conflict of interest.

## **References**

- [1] Simon M, Ford RA, Franklin AR et al (2005) Analysis of lead oxide (PbO) layers for direct conversion x-ray detection. IEEE Trans Nucl Sci 52:2035-2040. doi: 10.1109/NSSMIC.2004.1466833

- [2] Rowlands JA, Yorkstone J (2000) Flat panel detectors for digital radiography. In: Beutel J, Kundel HL, Van Metter RL (eds) Handbook of medical imaging, vol.1. SPIE Press, Bellingham pp 223-328
- [3] Zentai G (2009) Photoconductor-based (direct) large-area x-ray imagers. JSID 17: 543-550. doi:10.1889/JSID17.6.543
- [4] Macleod HA (2010) Factors affecting layer and coating properties. In: Brown RGW, Pike ER (eds) Thin film optical filters, 4th edn. CRC Press, Boca Raton, pp 569-584
- [5] Anders A (2010) A structure zone diagram including plasma-based deposition and ion etching. Thin Solid Films 518:4087-4090. doi:10.1016/j.tsf.2009.10.145
- [6] Semeniuk O, Juska G, Oelerich JO et al (2016) Charge transport mechanism in lead oxide revealed by CELIV technique. Sci Rep 6:33359. doi:10.1038/srep33359
- [7] Wiechert DU, Grabowski SP, Simon M (2005) Raman spectroscopic investigation of evaporated PbO layers. Thin Solid Films 484:73-82. doi:10.1016/j.tsf.2005.02.010
- [8] Bigelow JE, Haq KE (1962) Significance of fatigue in lead oxide vidicon target. J Appl Phys 33:2980-2982. doi: 10.1063/1.1728546
- [9] Hwang OH, Kim SS, Suh JH et al (2011) Effect of thermal annealing of lead oxide film. Nucl Instrum Methods Phys Res A 633:S69-S71. doi: 10.1016/j.nima.2010.06.125
- [10] Scanlon DO, Kehoe AB, Watson GW (2011) Nature of the band gap and origin of the conductivity of PbO<sub>2</sub> revealed by theory and experiment. Phys Rev Lett 107:246402. doi:10.1103/PhysRevLett.107.246402

- [11] Berashevich J, Semeniuk O, Rubel O et al (2013) Lead monoxide  $\alpha$ -PbO: electronic properties and point defect formation. *J Phys: Condens Matter* 25:075803. doi:10.1088/0953-8984/25/7/075803
- [12] Zhitomirsky I, Gal-Or L, Kohn A et al (1995) Electrochemical preparation of PbO films. *J Mater Sci Lett* 14:807-810. doi:10.1007/BF00278136
- [13] Anders A (2005) Plasma and ion sources in large area coating: A review. *Surf Coat Technol* 200:1893-1906. doi:10.1016/j.surfcoat.2005.08.018
- [14] Krishna MG, Rao KN, Mohan S (1992) Optical properties of ion assisted deposited zirconia thin films. *J Vac Sci Technol A* 10:3451-3455. doi:10.1116/1.577801
- [15] Allen TH (1982) Properties of ion assisted deposited silica and titania films. *SPIE Proc* 0325:93-100. doi:10.1117/12.933291
- [16] Jensen TR, Warren J, Johnson RL (2002) Ion-assisted deposition of moisture-stable hafnium oxide films for ultraviolet applications. *Appl Opt* 41:3205-3210. doi:10.1364/AO.41.003205
- [17] Netterfield RP, Sainty WG, Martin PJ et al (1985) Properties of CeO<sub>2</sub> thin films prepared by oxygen-ion-assisted deposition. *Appl Opt* 24:2267-2272. doi:10.1364/AO.24.002267
- [18] Wang K, Abbaszadeh S, Karim KS et al (2015) Reactive ion-assisted deposition of cerium oxide hole-blocking contact for leakage-current suppression in an amorphous selenium multilayer structure. *IEEE Sens J* 15:3871-3876. doi:10.1109/JSEN.2015.2397953
- [19] McNeil JR, Barron AC, Wilson SR et al (1984) Ion-assisted deposition of optical thin films: low energy vs high energy bombardment. *Appl Opt* 23:552-559. doi:10.1364/AO.23.000552

- [20] Wang L, Yoon MH, Lu G et al (2006) High-performance transparent inorganic–organic hybrid thin-film n-type transistors. *Nat Mater* 5:893-900. doi:10.1038/nmat1755
- [21] Tan M, Deng Y, Hao Y (2013) Enhanced thermoelectric properties and superlattice structure of a  $\text{Bi}_2\text{Te}_3/\text{ZrB}_2$  film prepared by ion-beam-assisted deposition. *J Phys Chem C* 117:20415-20420. doi:10.1021/jp4053133
- [22] Tepavcevic S, Choi Y, Hanley L (2003) Surface polymerization by ion-assisted deposition for polythiophene film growth. *J Am Chem Soc* 125:2396-2397. doi: 10.1021/ja029851s
- [23] Farhan MS, Zalnezhad E, Bushroa AR et al (2013) Electrical and optical properties of indium-tin oxide (ITO) films by ion-assisted deposition (IAD) at room temperature. *IJPEM* 14:1465-1469. doi:10.1007/s12541-013-0197-5
- [24] Zhang XW, Boyen HG, Deyneka N (2003) Epitaxy of cubic boron nitride on (001)-oriented diamond. *Nat Mater* 2:312 - 315. doi:10.1038/nmat870
- [25] NIST X-ray Photoelectron Spectroscopy Database. <https://srdata.nist.gov/xps/>. Accessed 12 December 2016
- [26] Vad K, Csik A, Langer GA (2009) Secondary neutral mass spectrometry - a powerful technique for quantitative elemental and depth profiling analyses of nanostructures. *Spectrosc Eur* 21:13-17. ISSN: 09660941
- [27] Geiger JF, Kopnarski M, Oechsner H (1987) SNMS-analysis of insulators. *Mikrochim Acta* 91:497-506. doi:10.1007/BF01199524

- [28] Oechsner H (1995) Secondary neutral mass spectrometry (SNMS)-recent methodical progress and applications to fundamental studies in particle/surface interaction. *Int J Mass Spectrom Ion Proces* 143:271-282. doi:10.1016/0168-1176(94)04122-N
- [29] Kabir M, Kasap S, Rowlands A J (2006) Photoconductors for x-ray image detectors. In: Kasap S, Capper P (eds) *Springer Handbook of Electronic and Phntonic Materials*. Springer, New York, pp. 1125-1126
- [30] Grenet J, Larmagnac JP, Michon P (1980) Aging and crystallization of evaporated amorphous selenium films. *Thin Solid Films* 67:L17-L20. doi:10.1016/0040-6090(80)90309-0
- [31] Droessler LM, Assender HE, Watt AAR (2012) Thermally deposited lead oxides for thin film photovoltaics. *Mater Lett* 71:51-53. doi:10.1016/j.matlet.2011.12.027
- [32] Zhang H, Ouyang J (2011) High-performance inverted polymer solar cells with lead monoxide-modified indium tin oxides as the cathode. *Org Electron* 12:1864–1871. doi:10.1016/j.orgel.2011.07.023
- [33] Wang Q, Deng Z, Ma D (2009) Highly efficient inverted top-emitting organic light-emitting diodes using a lead monoxide electron injection layer. *Opt Express* 17:17269-17278. doi:10.1364/OE.17.017269

## **Chapter 5: Investigation of X-ray performance of PbO**

### **5.1. X-ray performance of poly-PbO**

This topic has been elaborated in the following publication: [O. Semeniuk](#), O. Grynko, G. Decrescenzo, G. Juska, K. Wang & A. Reznik “Characterization of polycrystalline lead oxide for application in direct conversion X-ray detectors”, accepted with minor revisions to *Scientific Reports*. The full text of the publication is listed below.

# **Characterization of polycrystalline lead oxide for application in direct conversion X-ray detectors**

O. Semeniuk<sup>1,2\*</sup>, O. Grynko<sup>1,2</sup>, G. Decrescenzo<sup>3</sup>, G. Juska<sup>4</sup>, K. Wang<sup>5\*</sup>, A. Reznik<sup>2,3</sup>

1. Chemistry and materials science program, Lakehead University, 955 Oliver Road, Thunder Bay, ON, Canada P7B 5E1
2. Advanced detection devices department, Thunder Bay Regional Health Research Institute, 290 Munro Street, Thunder Bay, ON Canada P7A 7T1
3. Department of Physics, Lakehead University, 955 Oliver Road, Thunder Bay, ON, Canada P7B 5E1
4. Department of Solid State Electronics, Vilnius University, Saulėtekio 9 III k., 10222 Vilnius, Lithuania
5. SYSU-CMU Joint Institute of Engineering, School of Electronics and Information Technology, Sun Yat-sen University, 132 Waihua Rd., Guangzhou 510006, P. R. China.

\**e-mail*: [osemeniu@lakeheadu.ca](mailto:osemeniu@lakeheadu.ca) (O. Semeniuk); [wangkai23@mail.sysu.edu.cn](mailto:wangkai23@mail.sysu.edu.cn) (K. Wang).

## Abstract

While polycrystalline lead oxide (poly-PbO) is known to be one of the most promising photoconductors for utilization in X-ray detectors, its major performance parameters such as charge yield and mobility-lifetime product ( $\mu\tau$ ) are still not well established and require further investigation. Combining the conventional X-ray induced photocurrent and pulse height spectroscopy techniques we examine the X-ray photogeneration and recombination processes in poly-PbO. The measurements indicate that the amount of energy required to release a single electron hole pair  $W_{\pm}$  (inverse of charge yield) strongly depends on applied electric field and at  $10 \text{ V}/\mu\text{m}$  reaches  $\sim 20 \text{ eV}/\text{ehp}$ . Fitting the measured pulse height spectra with the Hecht formula provided  $\mu\tau$  for holes and electrons to be  $4.1 \times 10^{-8} \text{ cm}^2/\text{V}$  and  $10^{-9} \text{ cm}^2/\text{V}$ , respectively. Obtained  $\mu\tau$  values combined with recently reported mobility values of charge carriers in PbO suggest a new direction towards improvement of PbO technology by incorporation of Frisch grid or X-ray transistor architectures.

## Introduction

Semiconductor-based direct-conversion X-ray detectors have been actively sought for a wide range of applications in the fields of domestic security, medical imaging and astronomy [1-9]. Compared with its indirect conversion counterpart, the direct conversion scheme offers an improved performance in sensitivity and resolution, provided that a high-performance photoconductor as an X-ray-to-charge transducer is employed. Multiple crystalline and non-crystalline direct-conversion semiconductor materials are currently in competition for practical usage. For large area detectors with a photoconductive layer deposited directly on the imaging array, the crystalline materials are disfavored due to process incompatibility and high thermal budgets [10]. Currently, the only

commercially-viable X-ray photoconductor in direct-conversion X-ray imaging is amorphous selenium (a-Se) whose properties meet the requirements of wide dynamic range and low energy applications (due to its comparatively low atomic number  $Z$ ) and therefore, it is mainly used for medical applications in the so-called “mammography energy range”  $\sim 20$  keV [11]. For higher X-ray energies, a-Se has to be replaced by higher  $Z$  material. With recent results on solution-processed high  $Z$  perovskites, it seems like a new generation of smart materials for radiation sensing is emerging, however, large area perovskite semiconductors are not mature enough for practical application and require more investigation [1,12]. Currently, Polycrystalline lead oxide (PbO) is one of the most promising candidates due to high  $Z$  of Pb and proven capability for low-dose and high-resolution imaging. Previously, Simon et al. showed the first prototype of a PbO direct conversion flat panel detector and evaluated its imaging performance [13]. The results were very encouraging: the charge yield was high enough for low dose imaging while the modulation transfer function (MTF) was limited only by the pixel size, indicating potentially a very high spatial resolution [13, 14]. However, such a detector exhibited image lag caused by a residual current even after terminating the X-ray irradiation. This is a very undesirable effect that hampers real time imaging applications. The root cause of the residual current is still unclear, although it was suggested that charge accumulation near the bias electrode triggers injection and thus is responsible for the poor temporal performance of the detector [13]. A similar effect was also observed in a-Se structures, where charge trapping on the electrode/a-Se interface was suspected to enhance the local electric field, thus facilitating charge injection [15,16]. Once X-ray exposure is terminated, the enhancement of electric field decreases as a result of charge de-trapping, which further leads to the decay of the injected current observed as image lag. The injection-related processes in a-Se are relatively slow and were shown to manifest on the order of seconds [15,16].

In addition, the X-ray charge yield of PbO, although higher than that of a-Se, was still lower than the theoretically predicted one. This resulted in relatively high electron-hole pair creation energy  $W_{\pm}$ . The evaluation of  $W_{\pm}$  was previously performed with an X-ray induced photocurrent method (XPM) [13,17]. In this technique, the charge carriers are generated with a relatively *long* X-ray pulse, while constant bias voltage is applied to the detector to extract the generated carriers.  $W_{\pm}$  is obtained by integrating the X-ray signal and comparing the total collected charges against the energy of the incident flux of radiation [13, 18]. The major disadvantage of the XPM measurement is that if the charge injection takes place in the material (as it was suggested for poly-PbO), the injected current will be added to the X-ray signal of the detector, thus reducing the calculated  $W_{\pm}$  and leading to the overestimated X-ray conversion efficiency of the detector. In addition, the injection can cause the residual current i.e. image lag.

Charge injection is a common problem for many semiconductors [13, 15, 16, 19] and it was shown that alternative experimental techniques allow an accurate characterization of both the temporal response and the charge yield of the detector. For example, an advanced XPM technique, performed with a sequence of short X-ray pulses (millisecond scale) rather than a single long pulse (seconds scale), is frequently chosen for investigation of the temporal behavior of the detector, since it allows differentiation between injected and X-ray photogenerated charge [15,16]. At the same time, Pulse Height Spectroscopy (PHS) performed with a monoenergetic X-ray source is also a tool-of-choice for accurate measurements of  $W_{\pm}$  [18,20-23]. In this technique, the charge from a *single* absorbed X-ray photon is integrated over a very *short* time (microseconds) and compared with the energy of an incident photon. Since the signal is generated by a single photon absorption at very low flux rates (in contrast to X-ray flux used in XPM), there is no significant (if any) electric field redistribution, while utilization of microsecond integration times makes PHS spectrum

insensitive to injection currents, thus providing a more accurate measurement of  $W_{\pm}$ . In addition, the shape of the pulse height spectrum also gives insights into the charge transport, being affected by the mobility-lifetime product,  $\mu\tau$ , of the carriers [18]. This in turn allows evaluation of the carrier schubweg  $s$ , i.e., the mean carrier range before it is trapped by deep traps or recombines. Schubweg can be expressed as the product of charge mobility  $\mu$ , lifetime  $\tau$  and applied field  $F$  i.e.  $s = \mu\tau F$ .

It should be noted that PHS measurements have never been performed on poly-PbO mainly due to a challenge to make PbO X-ray detector with low noise to acquire spectra with distinguishable peaks. Recent improvements in the deposition technology lead to a significant dark current suppression that in turn enables measuring an X-ray photocurrent spectrum with distinguishable peaks. In this work, we apply both advanced XPM and PHS methods to study charge generation in polycrystalline PbO to understand the source of lag and to examine the feasibility of real-time imaging. We also provide an analysis of the  $\mu\tau$  product for holes and electrons ( $\mu_h\tau_h$  and  $\mu_e\tau_e$ , respectively) and  $W_{\pm}$  for a wide range of electric fields.

## Results

### Experimental data by XPM

The typical X-ray response of poly-PbO is shown in Fig. 1. As can be seen, our result is very similar to the previously published data by Simon et al. [13]. The amplitude of the signal grows in the beginning of the X-ray pulse, reaching the steady state value in  $\sim 2$  seconds. At the end of the exposure, there is a well-pronounced residual signal, or lag. With increasing the applied electric field  $F$ , the signal amplitude and signal lag also increase, however when data are normalized, they closely resemble each other as shown in the inset to Fig. 1.

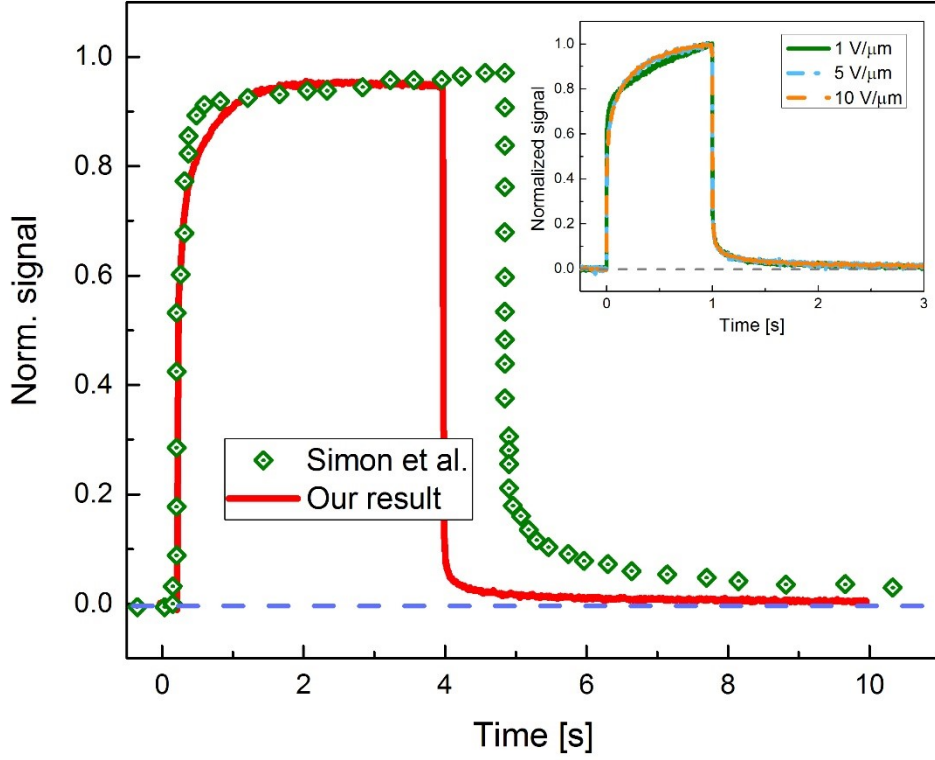


Figure 1. X-ray signal of poly-PbO, measured at  $F = 4 \text{ V}/\mu\text{m}$ . The inset shows normalized X-ray signals measured at different applied fields. Dark signal  $I_{dark}$  is subtracted.

In order to calculate  $W_{\pm}$  from XPM measurements, the signal is integrated and the total collected charged is compared against the exposure to the PbO detector [13, 17]. For the 3.75 s X-ray pulse at  $F = 4 \text{ V}/\mu\text{m}$ , we obtained  $W_{\pm} \approx 12 \text{ eV}/\text{ehp}$ , which is larger than theoretically predicted by Klein rule ( $W_{\pm}^{th} \sim 5.9 \text{ eV}$ ) [13] but it is in a good agreement with the previously reported value of 9.9 eV/ehp, obtained under similar experimental conditions (5 s X-ray pulse,  $F = 3.5 \text{ V}/\mu\text{m}$  [13]). However, it should be noted that  $W_{\pm}$  measured by this method appeared to be sensitive to the X-ray pulse duration  $t_{pulse}$ . Longer X-ray pulses give smaller  $W_{\pm}$  and even  $W_{\pm}^{th}$  can be reached at

higher electric fields ( $F > 10 \text{ V}/\mu\text{m}$ ) and longer exposures ( $t_{pulse} > 3.75 \text{ s}$ ). At the same time, if we decrease the X-ray pulse duration,  $W_{\pm}$  values will increase. For instance, at  $F = 4 \text{ V}/\mu\text{m}$  and  $t_{pulse} = 100 \text{ ms}$ ,  $W_{\pm}$  will increase to  $14.2 \text{ eV}/\text{ehp}$ . If we decrease exposure time even further at the same electric field,  $W_{\pm}$  values will continue to grow, reaching values of  $15.8$  and  $18.3 \text{ eV}/\text{ehp}$  at  $t_{pulse} = 50$  and  $10 \text{ ms}$ , respectively. In order to investigate such peculiar dependence of  $W_{\pm}$  values on the duration of X-ray pulse, we used an X-ray chopper to modulate the exposure to the detector. The example is shown in Fig. 2, where a  $3.75 \text{ s}$  long X-ray pulse was modulated with the frequency of  $5 \text{ Hz}$  and  $50/50$  duty cycle, thus effectively providing  $\sim 18$  X-ray pulses  $100 \text{ ms}$  each with the  $100 \text{ ms}$  interval between pulses.

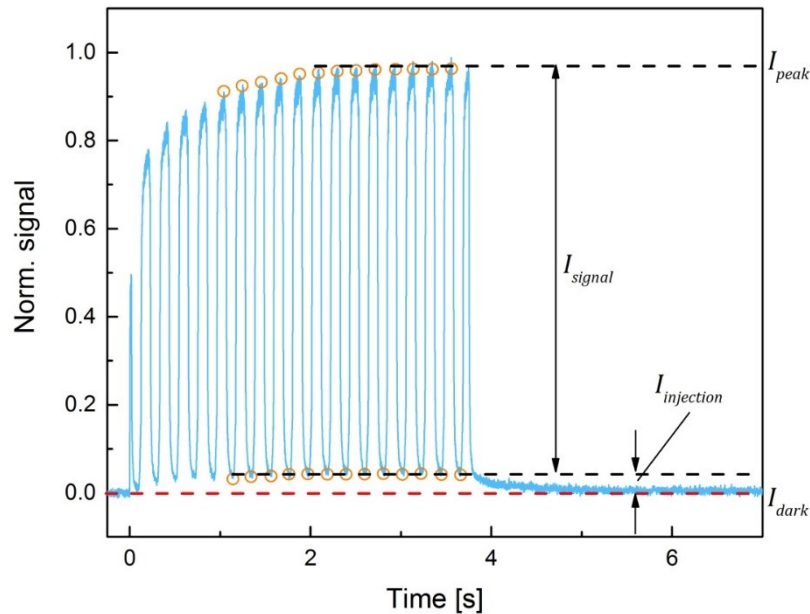


Figure 2. Response of PbO detector to the modulated X-ray exposure at  $F = 2 \text{ V}/\mu\text{m}$ . It should be noted that first points at the beginning of the exposure are affected by asynchronous position of the chopper as compared to the start of the exposure and fluctuations in X-ray intensity at the beginning of the X-ray pulse.

Experiments with modulated X-ray pulse shown in Fig. 2 revealed that the X-ray response of PbO detector  $I_{peak}$  has two components: the signal due to the X-ray generation of charge carriers  $I_{signal}$  and the signal due to the increase in the dark current i.e. injection  $I_{injection}$ . As shown in Fig. 2,  $I_{injection}$  builds up during the X-ray exposure reaching a steady-state value after  $\sim 2$  s, while the  $I_{signal}$  has a constant amplitude. Moreover, it was found that the injection current level changes with the chopper frequency  $f$  as shown in Fig. 3, where the steady-state ratio of  $I_{injection}/I_{peak}$  is plotted as a function of  $f$ . At higher frequencies,  $I_{injection}$  contributes more to the total signal (corresponds to higher  $I_{injection}/I_{peak}$  ratio on the graph) than at the lower frequencies. At the end of exposure  $I_{injection}$  decays over time and is observed as lag. As seen from Fig. 2, when X-rays are terminated, lag rolls off from the steady-state  $I_{injection}$  level reached during the X-ray pulses. The decay of lag with time for different frame rates is shown in Fig. 4. The magnitude of lag is proportional to X-ray pulse duration  $t_{pulse}$ . Thus, for 1 s X-ray exposure, it takes several seconds to decay below 1 %. At the same time if exposure lasts only 10 ms, it takes less than 50 ms to decay to about the same level. Also, lag is more severe at shorter exposures. This is in agreement with the previous observation of higher  $I_{injection}/I_{peak}$  ratio for higher chopper speed (i.e. shorter X-ray pulses) shown in Fig.3.

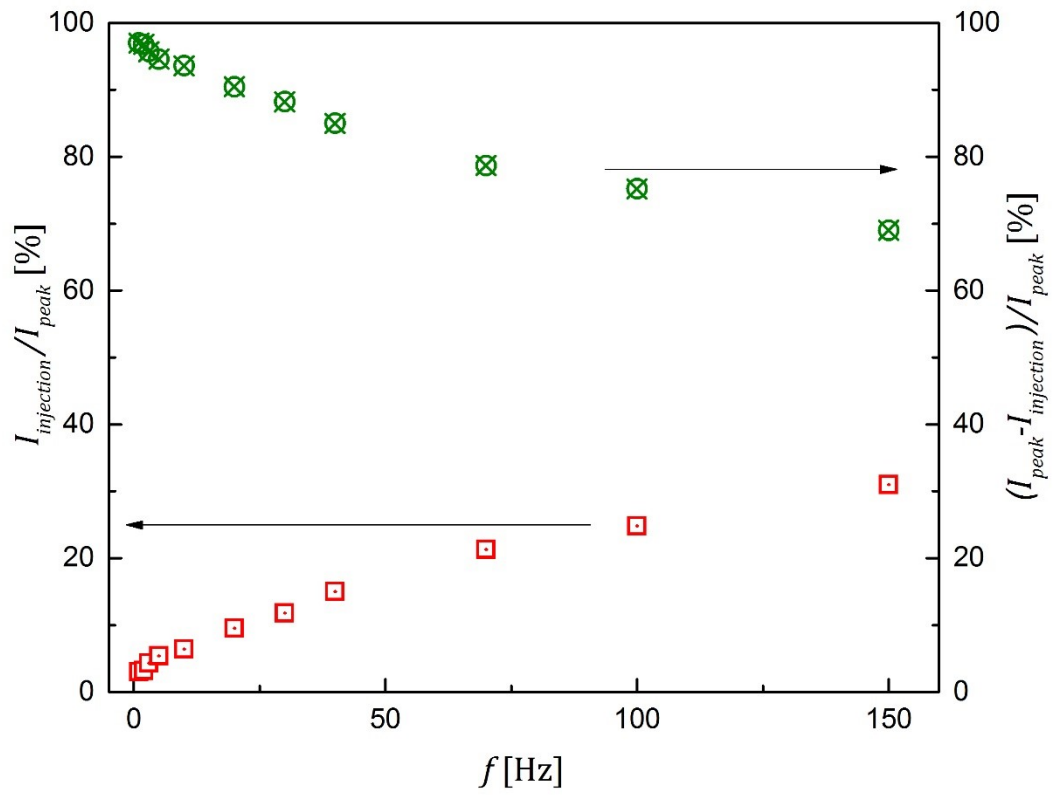


Figure 3. The ratios of  $I_{injection}/I_{peak}$  and  $I_{signal}/I_{peak}$  are plotted as a function of the chopper frequency  $f$  for  $F = 2 \text{ V}/\mu\text{m}$ .

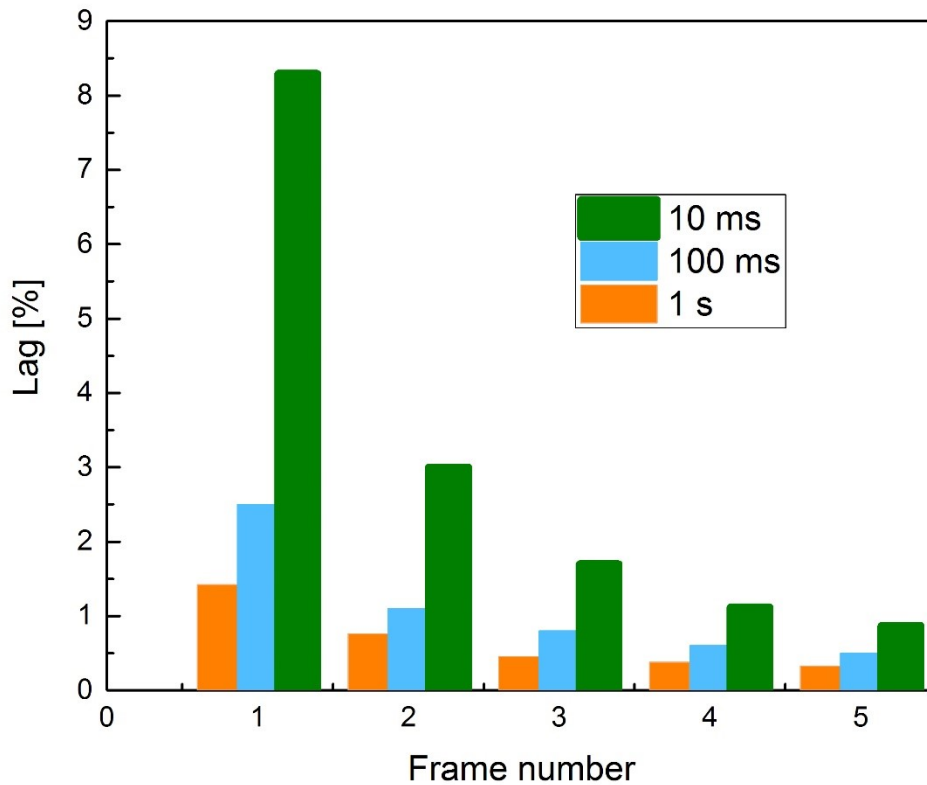


Figure 4. The lag (presented as a percentage of  $I_{peak}$ ) is shown as the function of a frame number. The frame read-out time is the same as exposure duration.

### Experimental data by PHS

Fig. 5 exhibits the typical pulse height spectrum of poly-PbO. The spectral waveform is seen to be asymmetrical and obscured by the background noise at lower channel numbers. The measured PHS allows us to determine the  $\mu\tau$  product of the charge carriers and the value of  $W_{\pm}$  which corresponds to the position of the spectral peak [24]. However, because of asymmetrical nature of the spectrum a numerical simulation must be applied to accurately determine the peak position [24-29]. For our experimental conditions we expect nearly uniform charge generation since the attenuation length

of PbO  $\delta \approx 300 \mu\text{m}$  (for  $\varepsilon = 59.5 \text{ keV}$  [10]) is much larger than the detector thickness ( $d = 42 \mu\text{m}$ ). Therefore, we divided the PbO layers into virtual slices and assuming uniform generation, calculated the collection efficiency from every slice using the depth dependent Hecht formula. This formula describes the collection efficiency  $\eta(x)$  (i.e., the ratio of collected charge carriers  $N_{col}$  to the total number of carriers created by the X-ray absorption  $N_{gen}$ ) as follows [24-29]:

$$\eta(x) = \frac{N_{col}(x)}{N_{gen}} = s_h/d \left(1 - e^{-\frac{d-x}{s_h}}\right) + s_e/d \left(1 - e^{-\frac{x}{s_e}}\right) \quad (1)$$

where  $x$  is the distance from the anode to the charge generation position,  $s_{h,e}$  is carrier schubweg. Subsequently, the Hecht fit was convolved with noise spectrum and the result was used to fit the measured spectra. After a spectrum fit was obtained the true peak position was determined from the unconvolved Hecht fit (see Fig. 5). The fitting provided the mobility-lifetime products for holes and electrons  $\mu_h\tau_h = 4.1 \times 10^{-8} \text{ cm}^2/\text{V}$ ,  $\mu_e\tau_e \approx 10^{-9} \text{ cm}^2/\text{V}$ .  $\mu\tau$  values are assigned to a type of carrier based on the previous reports that revealed holes to be the faster carrier in poly-PbO [30,31].

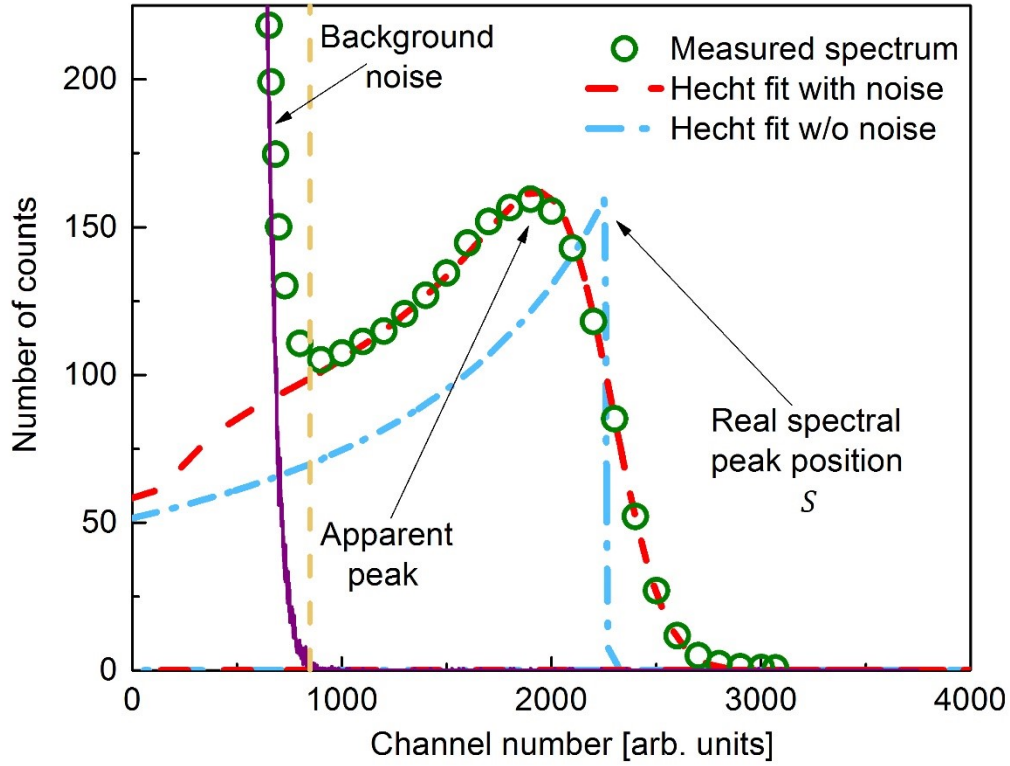


Figure 5. Pulse height spectrum measured with 42  $\mu\text{m}$  PbO sample at  $F = 10 \text{ V}/\mu\text{m}$ ,  $\varepsilon = 59.5 \text{ keV}$ , shaping time  $\tau_s = 50 \mu\text{s}$  and superimposed with noisy and noiseless Hecht fits. Background counts are shown to dominate the spectral waveform below channel 800 (vertical dashed line). The measured position of the noise free spectral peak is shown to be affected by the system noise.

The Hecht fit shows how the true peak position  $S$  is affected by the system noise, which is typical for materials with significant differences in carrier's *schubweg* [24-29]. Electron-hole pair creation energy  $W_{\pm}$  was derived from the true peak position  $S$  as:

$$W_{\pm} = \varepsilon/S, \tag{2}$$

where  $\varepsilon = 59.5$  keV corresponds to emission from  $^{241}\text{Am}$  source. Fig. 6 shows the field dependence of  $W_{\pm}$  for different shaping times  $\tau_s$ , as derived from PHS measurements. As seen from Fig. 6,  $W_{\pm}$  decreases with both  $F$  and  $\tau_s$  reaching the value  $\sim 17$  eV/ehp at  $F = 10$  V/ $\mu\text{m}$  and  $\tau_s = 17$   $\mu\text{s}$ .

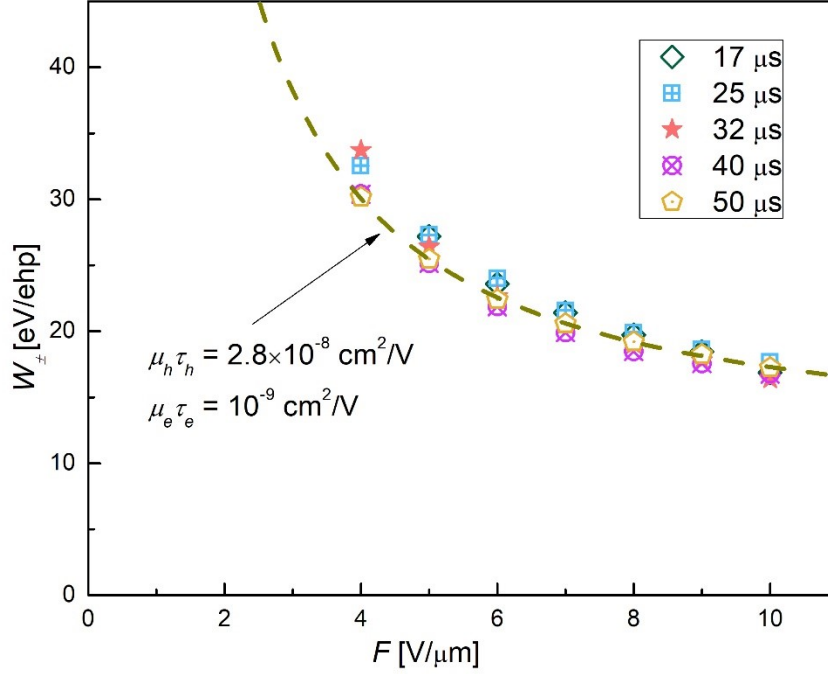


Figure 6. Measured values of  $W_{\pm}$  are plotted as a function of  $F$  for different  $\tau_s$ .

We used the dependence of  $W_{\pm}$  on  $F$  to validate  $\mu\tau$  values obtained from PHS measurements, following the recipe in Ref. [32] where X-ray sensitivity is given by:

$$\frac{N_{col}}{N_{inc}} = x_h \left[ \left( 1 - e^{-\frac{1}{\Delta}} \right) + \frac{1}{\frac{\Delta}{x_h} - 1} \left( e^{-\frac{1}{x_h}} - e^{-\frac{1}{\Delta}} \right) \right] + x_e \left[ \left( 1 - e^{-\frac{1}{\Delta}} \right) - \frac{1}{\frac{\Delta}{x_e} + 1} \left( 1 - e^{-\frac{1}{x_e} - \frac{1}{\Delta}} \right) \right] \quad (3)$$

Here  $x_e, x_h$  are normalized electron and hole schubwegs, respectively ( $x_{e,h} = S_{e,h}/d$ ),  $\Delta$  is a normalized attenuation length  $\Delta = \delta/d$  and  $N_{inc}$  is the number of incident X-ray quants. For our case of uniform absorption, equation (3) can be simplified as follows:

$$\frac{N_{col}}{N_{inc}} = \frac{1}{\Delta} \left[ x_h \left( 1 + x_h \left( e^{-\frac{1}{x_h}} - 1 \right) \right) + x_e \left( 1 + x_e \left( e^{-\frac{1}{x_e}} - 1 \right) \right) \right] \quad (4)$$

assuming that for large  $\Delta$  (i.e. uniform absorption):  $\left( 1 - e^{-\frac{1}{\Delta}} \right) \rightarrow \frac{1}{\Delta}$ ;  $\frac{1}{\frac{\Delta}{x_{e,h}} + 1} \rightarrow \frac{x_{e,h}}{\Delta}$ ;  $e^{-\frac{1}{\Delta}} \rightarrow 1$ . It

should be noted, that equations (3,4) provide a generic expression of photoconductor sensitivity, simultaneously accounting for both *X-ray absorption efficiency* and *collection efficiency*. To derive the *charge collection efficiency* only as measured with PHS, equation (4) should be divided by absorption efficiency  $\left( 1 - e^{-\frac{1}{\Delta}} \right)$ , which for large  $\Delta$  reaches  $\frac{1}{\Delta}$ . Thus, the expression for collection efficiency for the case of uniform absorption looks as follows:

$$\eta = \frac{N_{col}}{N_{gen}} \left[ x_h \left( 1 + x_h \left( e^{-\frac{1}{x_h}} - 1 \right) \right) + x_e \left( 1 + x_e \left( e^{-\frac{1}{x_e}} - 1 \right) \right) \right] \quad (5)$$

where  $N_{gen} = N_{inc}/\Delta$ . Interestingly, same expression (5) can be obtained by integrating equation (1) over  $x$  and normalizing by thickness  $d$ .

Fitting  $W_{\pm}$  dependence on  $F$  (shown in Fig. 6) with equation (5) provided similar  $\mu\tau$  values as those obtained from spectrum fitting:  $\mu_h\tau_h = 2.8 \times 10^{-8} \text{ cm}^2/\text{V}$ ,  $\mu_e\tau_e \approx 10^{-9} \text{ cm}^2/\text{V}$ .

## Discussion

Although XPM measurements are affected by the injection current and hence overestimate the total charge created leading to inaccurate  $W_{\pm}$  values, they can be still used to elucidate the signal lag in

poly-PbO. Conventionally, in disordered structures, lag is linked to the release of carriers that have been previously trapped into deep traps within the band tails [33]. If the release time from these traps is longer than the frame duration, then the de-trapped charge will cause a residual current even after termination of X-ray exposure. However, as seen from the inset of Fig. 1, the lag is scalable with applied field, while Figs. 3 and 4 show that lag is proportional to exposure duration  $t_{pulse}$ , indicating that it is not associated with the charge carriers trapping during their transit across the sample. Indeed, if charge trapping and de-trapping was responsible for lag in PbO, the lag should decrease with application of higher electric field, as charge schubweg becomes larger and de-trapping becomes more efficient. The de-trapping time and therefore the signal lag also should not depend on  $t_{pulse}$ , as it is a fundamental property of material and not an experimental parameter. Finally, previous observations of lag dependence on the material of the bias electrodes [13] suggest that charge trapping in the bulk is not the dominant mechanism for signal lag in poly-PbO.

A plausible explanation of these effects is the time-dependent enhancement of the electric field at the metal/semiconductor interface that triggers *injection* from the bias electrodes into the poly-PbO. XPM measurements utilize a flux of X-rays to generate a measurable signal, thus creating a relatively large amount of charge carriers. When the charge carriers get trapped, they redistribute the electric field applied to the sample. If they are trapped on the electrode/photoconductor interface (surface of the photoconductor has an extreme concentration of trapping states), they might cause a local enhancement of electric field. This triggers injection, which builds up over exposure time, and introduces uncertainty in derived values of  $W_{\pm}$  [15,16].

The trapped carriers can de-trap and therefore injection builds up until a steady state level of accumulated charge is reached between the trapping and de-trapping charge at the interface. After X-ray exposure, the electric field gradually returns to the initial level and the residual injection

current decreases accordingly. The kinetics of the injection build up during exposure is further elaborated with pulsed X-rays. Fig. 7 shows the response of poly-PbO to two successive 100 ms pulses, plotted in a semi-log scale.

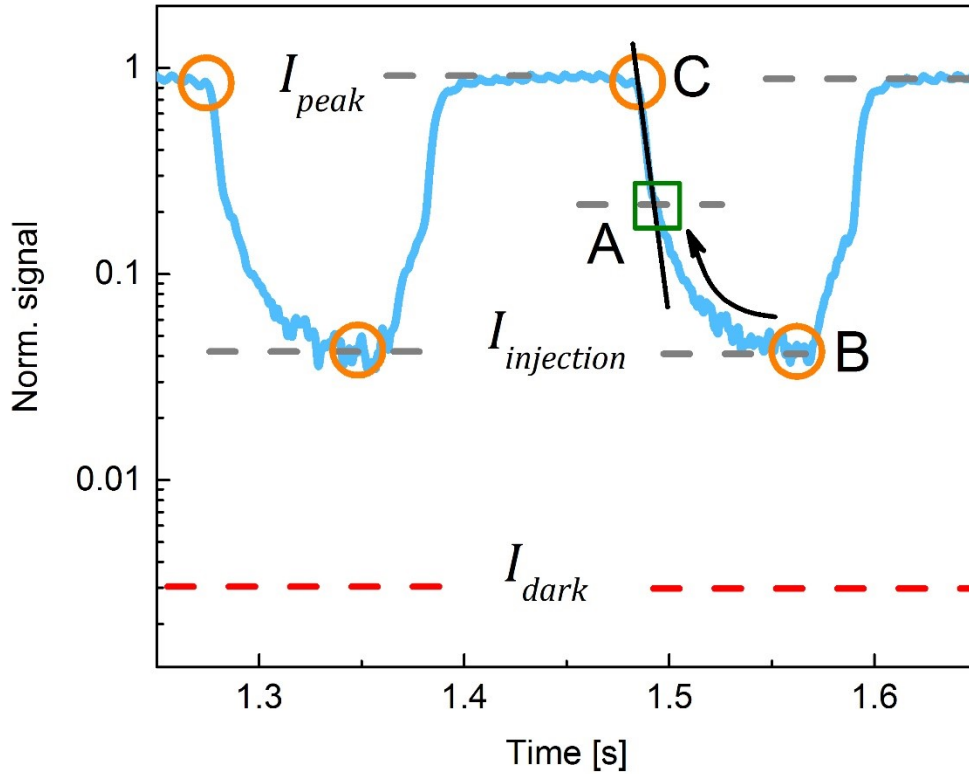


Figure 7. The response of PbO detector to subsequent 100 ms X-ray pulses at  $F = 2 \text{ V}/\mu\text{m}$  plotted in the semi-log scale (taken from the middle section of the graph shown in Fig. 2). Points C and B represent the total current and the injection current levels, respectively, while point A defines the inflection point in the signal decay, i.e. the beginning of lag.

As shown in Fig. 7, the kinetics of the signal  $I_{signal}$  is composed of two components: fast C-A and slow A-B. The fast C-A component is associated with the transit of the X-ray generated carriers through the sample, while slow A-B component represents the contribution of the injection current

to the total signal  $I_{peak}$  [15,16]. With increase in chopper frequency, the X-ray pulse duration and the interval between pulses decrease. This shifts point B toward the A region, thus resulting in larger injection current levels (see Figs. 3, 4). It would be very tempting to use only the C-A signal value for the  $W_{\pm}$  calculations; however, the position of A will vary with experimental conditions such as X-ray pulse duration, exposure, etc. Indeed, as shown in Fig. 4, lag depends on X-ray pulse duration. Since C-A signal value is inversely correlated to lag, it makes C-A also depend on experimental conditions. This suggests that for materials with dynamic type of injection, XPM measurements inherently overestimate  $W_{\pm}$  values. Therefore  $W_{\pm}$  measurements should be verified with an alternative technique insensitive to injection, such as PHS.

It should be noted, that the XPM measurements performed here indicate that temporal performance of the PbO based detector is limited by the structure of the detector, rather than by fundamental charge transport properties of poly-PbO. This finding suggests a possible avenue of improvement of PbO technology: development a PbO blocking structure, as it was previously done for a-Se [2]. Indeed, sandwiching poly-PbO between the blocking layers that will prevent charge injection from bias electrodes into material, while permitting charge exit from the material, should improve the temporal performance of PbO detectors and make it suitable for real time dynamic imaging.

The asymmetrical shape of the spectral waveform revealed by the PHS measurements and shown in Fig. 5, is indicative of a considerable difference between electron and hole schubwegs and the ballistic deficit as a result of insufficient shaping time [18, 24, 25, 29]. However, an increase in shaping time and the application of higher electric field cannot bring the PHS histogram closer to a Gaussian shape. This suggests that at the electric fields applied here, the transit time of the slower carriers is much longer than the shaping times used. Similar phenomenon was observed on other materials, like CdTe and CdZnTe, which are currently used as gamma-detectors [24, 25, 34]. In

these materials, holes are much slower than electrons and possess a relatively long transit time. Also, fitting of the PHS spectra gave a mobility-lifetime products of  $\approx 4.1 \times 10^{-8} \text{ cm}^2/\text{V}$  (for faster carriers) and  $\approx 10^{-9} \text{ cm}^2/\text{V}$  (for slow carrier), respectively. Based on previously reported measurements of electron and hole transport in poly-PbO, we assign the larger  $\mu\tau$  value for holes. Indeed, it has been shown that similar to a-Se, holes in PbO are much faster carriers than electrons [30,31]. Given the mobility-lifetime product for holes of  $\mu_h\tau_h \approx 4.1 \times 10^{-8} \text{ cm}^2/\text{V}$ , at  $F=10 \text{ V}/\mu\text{m}$  the hole schubweg  $s_h = 41 \mu\text{m}$  which is almost the sample thickness  $d = 42 \mu\text{m}$ . It is not surprising that at this particular field charge collection efficiency is no longer dependent on the integration time: as this is seen in Fig. 6 at  $F = 10 \text{ V}/\mu\text{m}$  where all data points merge together as most of X-ray generated holes are collected regardless of the integration time used in the experiment. The situation is very much different for slower electrons with  $\mu_e\tau_e \approx 10^{-9} \text{ cm}^2/\text{V}$ ; they do not contribute significantly to the signal on the  $\mu\text{s}$  scale. Overall, obtained with PHS mobility-lifetime values are smaller by an order of magnitude from those reported by Kabir on poly-PbO [13,35]. The discrepancy may arise from the difference in experimental techniques used to estimate  $W_{\pm}$ : while in our study we used PHS method, Kabir treated results obtained with XPM technique. Since XPM is sensitive to injection that supplements to the total integrated photocurrent, use of XPM technique may overestimate total collected charge thus underestimating  $W_{\pm}$  and overestimating  $\mu\tau$ .

The  $\mu_h\tau_h$  and  $\mu_e\tau_e$  measured here, allow us to estimate lifetimes for both types of carriers provided mobility values are known. For this purpose, we measured separately the hole mobility using a photo-CELIV technique similar to how it was done in Ref. [31]. Hole mobility was found to be  $\mu_h \approx 0.008 \text{ cm}^2/\text{Vs}$  at an electric field of  $1 \text{ V}/\mu\text{m}$ . Measurements at higher electric field were technically unfeasible due to the limited bandwidth of the signal generator. However, for a rough estimate of  $\tau_h$  we neglect mobility growth at higher electric field, obtaining  $\tau_h = \mu_h\tau_h/\mu_h \approx 5.1$

$\mu\text{s}$ . The hole lifetime of  $\tau_h = 5.1 \mu\text{s}$  differs from the one obtained earlier with the photo-CELIV technique ( $\sim 200 \mu\text{s}$ ) [31]. In photo-CELIV, non-equilibrium carriers are generated in unbiased samples by a short pulse of uniformly absorbed light. After a preset delay time, the carriers are extracted by a linearly increasing voltage pulse. The carrier lifetime is derived by varying the delay time between carrier photogeneration and application of the electric field. Therefore, photo-CELIV provides the lifetime of the *diffusing* carriers that for the special case of poly-PbO can significantly differ from the lifetime of *drifting* carriers. Indeed, the peculiarity of poly-PbO is its spatial inhomogeneity (poly-PbO layers are composed of randomly oriented platelets) that results in hole transport governed by a spatial disorder rather than energy disorder, which is typical for the majority of non-crystalline and amorphous materials [31]. For spatial disorder governed transport, carriers are trapped only when they drift as opposed to the case of energetic disorder where carriers fall into deeper trapping states with time regardless whether they drift or diffuse. Therefore, when holes are not drifting i.e. in the absence of electric field, they diffuse around the generation site and only slowly recombine, since the diffusion length  $L$  is very small:  $L = \sqrt{\mu\tau \frac{kT}{e}} \approx 0.3 \mu\text{m}$  (where  $k$  is Boltzmann constant,  $e$  – elementary charge and  $T$  – temperature), in comparison to both the sample thickness and  $\text{schubweg} \sim 41 \mu\text{m}$ . The relatively high dielectric constant of PbO ( $\epsilon = 13$  [31]) suggests that the recombination time might be longer than the trapping time during charge transit, thus effectively leading to longer lifetimes measured with CELIV.

In a similar fashion, it is possible to estimate the electron transit time and electron lifetime in our samples. Measurements of electron mobility in such a thick sample required a higher electric field than that could be obtained with the experimental equipment used, therefore as a reference point we used the mobility of electrons reported for a  $5 \mu\text{m}$  thick sample [30] and extrapolate it to our

thickness, as mobility in dispersive media is scalable with the thickness of the material [36, 37]. Since the hole mobility of the 42- $\mu\text{m}$ -thick sample was about an order of magnitude smaller than that of 5- $\mu\text{m}$ -thick sample [31], we can apply the same ratio to electrons. The electron mobility of the 5- $\mu\text{m}$ -thick sample was found to be  $\mu_e \approx 2 \times 10^{-5} \text{ cm}^2/\text{Vs}$  at  $F=10 \text{ V}/\mu\text{m}$  [30], therefore for 42  $\mu\text{m}$  thick sample we assume electron mobility  $\mu_e \approx 2 \times 10^{-6} \text{ cm}^2/\text{Vs}$ . For such  $\mu_e$  the electron lifetime is  $\tau_e \approx 0.5 \text{ ms}$ , while the electron transit time at maximal  $F = 10 \text{ V}/\mu\text{m}$ , would be  $\sim 21 \text{ ms}$ . These calculations suggest that electrons are responsible for ballistic deficit in the PHS measurements. In order to collect slow electrons i.e. to compensate for a ballistic deficit, the integration time should be on the order of milliseconds. Such a long integration time inevitably leads to significant noise increase [38] that thus would obscure the signal.

It should be noted that for the shaping times used in the experiment (17-50  $\mu\text{s}$ ) the measured  $W_{\pm}$  values are seen to saturate at  $W_{\pm} \approx 17 \text{ eV}/\text{ehp}$  for an electric field of  $10 \text{ V}/\mu\text{m}$ . Such a value of  $W_{\pm}$  compares very favorably with a  $W_{\pm}$  of  $\approx 45 \text{ eV}/\text{ehp}$  obtained on a-Se [18, 20] for the same electric field and shaping times used. a-Se is the only photoconductor currently used in direct conversion mammographic X-ray detectors. Poly-PbO with its higher charge yield and higher quantum efficiency looks to be a promising candidate to replace a-Se in the next generation digital X-ray detectors. In comparison with another promising material, namely  $\text{HgI}_2$ , PbO offers a similar performance in terms of signal lag and  $W_{\pm}$ , while  $\mu\tau$  and dark current are better in  $\text{HgI}_2$ . The latter can be improved by developing a PbO blocking structure, as it was successfully done for a-Se [16]. However,  $\text{HgI}_2$  layers are toxic in the sense that they chemically react with imaging array electronics, thus creating additional technological challenges [39,40]. Currently, the major competitors of PbO seems to be perovskite photoconductors, for example methylammonium lead iodide ( $\text{CH}_3\text{NH}_3\text{PbI}_3$ ). This photoconductor combines comparatively high carrier mobility with low

electron-hole creation energy of  $\sim 0.4$  eV/e-hp caused by photoconductive gain [12]. However, despite high carrier mobility,  $\mu\tau$  product is still low (although higher than in PbO) due to the short carrier lifetime. In addition, materials with photoconductive gain are generally challenging for real-time imaging, when fast temporal response is needed.

One of the current challenges in poly-PbO is the presence of the slower carrier, which diminishes the temporal response of the material. The co-existence of both fast and slow carriers is a common issue of solid state detectors. It has been addressed by the Frisch grid technology [41] and X-ray transistor technology [42]. Both technologies take advantage of the motion of the faster carrier locally. The objective is achieved by means of utilizing a coplanar grid, placed close to one of the bias electrodes or using transistor-type architecture. The Frisch grid detector is arranged in such a way that the charge signal is only induced during the motion of the charge carrier between the grid and the collection electrode, thus discarding the transit of the slower carriers across the sample and simultaneously suppressing the effect of charge carriers trapping in the bulk of the sample. The technology has proven efficient for both gas filled [41] and solid stated [43] detectors. Therefore, we suggest this proven technological solution be applied to a poly-PbO detector as well. The X-ray transistor architecture on the other hand, utilizes strong lateral field to collect fast carriers, while minimizing the impact of slow carriers on the output photocurrent. We believe that the improved speed of operation of the PbO detector together with smaller values of  $W_{\pm}$  and higher quantum efficiency than a-Se will make it a very promising candidate for both radiographic and fluoroscopic X-ray medical imaging applications.

## **Methods**

### **Sample preparation**

A 42  $\mu\text{m}$ -thick poly-PbO sample was grown by a thermal evaporation method where a high purity PbO powder was evaporated in the presence of oxygen gas as described elsewhere [13]. Evaporated poly-PbO layers have an interesting structure: it is composed of a porous network of platelets 1-3  $\mu\text{m}$  in size and  $\sim 100$  nm thick. The samples were deposited on a  $25 \times 25$  mm<sup>2</sup> glass substrate coated with conductive Indium Tin Oxide (ITO) layer, which serves as anode during XPM and PHS measurements. For the cathode, a gold contact 2 mm in diameter was sputtered atop the PbO layer.

### **Experimental apparatus**

Both  $W_{\pm}$  and  $\mu\tau$  product in poly-PbO were investigated by X-ray induced photocurrent (XPM) and pulse height spectroscopy (PHS) techniques. The typical XPM and PHS experimental apparatuses are shown in Figs. 8 **a** and **b**, respectively. For the XPM measurements, the Mammomat 3000 system at 35 kVp was used to generate long ( $t = 3.75$  s) exposures, while an X-ray tube model PX1412CS at 70 kVp was used to generate less than 1 s exposures. With both systems, we utilized a 2 mm thick aluminum filter, which limited the range of energies incident on the detector. The ionization chamber Keithley model 96035 was used to measure X-ray exposure to the poly-PbO detector, which varied between 5 mR to  $\sim 1$  R, depending on the pulse duration and X-ray system used. Also, a rotating chopper (2 mm Cu) was used to modulate the exposure in a wide frequency range between 1 to 150 Hz. During all experiments, an external power supply maintained a constant bias applied to the sample with the positive polarity applied to ITO. The signal current induced by the X-ray pulse in the PbO layers was observed on a 150 MHz bandwidth digital oscilloscope Tektronix model TDS 420.

For the PHS measurements, an <sup>241</sup>Am source was used to generate 59.5 keV monoenergetic X-rays. The signal generated by each X-ray photon was readout from the top (Au) contact coupled to

a low noise charge preamplifier (AMPTEK model A250CF), then to a pulse shaping amplifier (APTEC model 6300) and finally to a multi-channel analyzer (MCA, Ortec model ASPEC927). At the energy  $\varepsilon = 59.5$  keV emitted by the  $^{241}\text{Am}$  source the probability of photoelectric interactions in PbO is 89.1%, meaning that the measured PHS peak represents full absorption of the incident photon energy. The PHS apparatus was calibrated with a Si PIN photodiode (Thorlabs model FDS010). A value of  $W_{\pm}$  for Si = 3.62 eV/ehp [18] was assumed for the photodiode. A HP model 8111A signal generator, coupled to the test input of the preamplifier was used for the measurement of the preamplifier noise and shot noise intrinsic in the dark current of the detector. The main source of electronic noise was found to be the white noise due to the dark current of the PbO spectrometer, which was found to be  $I_{dark} \approx 200$  pA/mm<sup>2</sup> at 10 V/ $\mu\text{m}$ . The main sources of X-ray noise are Compton backscattering due to the glass substrate, aluminum box and the presence of unfiltered low energy peaks in the source itself. The source was collimated to a small beam directly on the sample in order to reduce the stray scatter from adjacent structures. The radioactive source was placed in a lead enclosure shown in Fig. 8b. The impact of the low-energy X-rays from the source was minimized by the use of a 2 mm Al filter placed between the source and the detector. Vibration isolation was used in order to eliminate the influence of external mechanical disturbances. The count rate of  $\sim 30\text{-}50$  s<sup>-1</sup> ensured that the influence of pulse pile-up can be ignored for pulse shaping time (17-50  $\mu\text{s}$ ) used in this study. The *background noise* spectrum was separately measured without the source and used for the deconvolution of the measured spectra.

PHS measurements have been done for the electric fields  $F$  from 4 V/ $\mu\text{m}$  to 10 V/ $\mu\text{m}$  with a step of 1 V/ $\mu\text{m}$  and for different shaping times  $\tau_s$  from 17  $\mu\text{s}$  to 50  $\mu\text{s}$ . The lower limit of applied field was determined by the ability to resolve the signal above electronic noise, whereas the upper limit was determined by the increase of the dark current and noise associated with it.

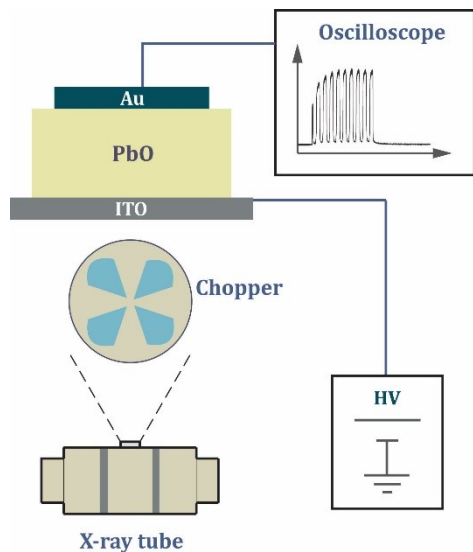


Figure 8. (a) Schematic representation of the XPM apparatus. The exposure was applied from the ITO side.

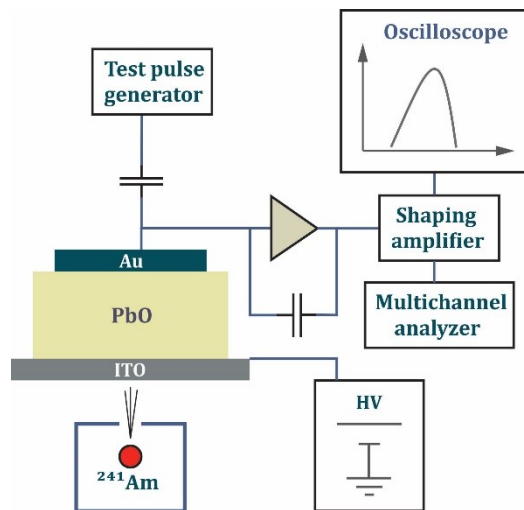


Figure 8. (b) Schematic representation of the PbO-based pulse height spectrometer with a virtual ground input to charge amplifier. The radioactive source was located behind the ITO glass.

## References

1. Wei, H. et al. Sensitive X-ray detectors made of methylammonium lead tribromide perovskite single crystals. *Nat. Photon.* **12**, 333-340 (2016).
2. Kasap, S. et al. Amorphous selenium and its alloys from early xeroradiography to high resolution x-ray image detectors and ultrasensitive imaging tubes. *Phys. Status Solidi B* **246**, 1794-1805 (2009).
3. Yaffe, M. J. & Rowlands, J. A. X-ray detectors for digital radiography. *Phys. Med. Biol.* **42**, 1-39 (1997).
4. Tegze, M. & Faigel, G. X-ray holography with atomic resolution. *Nat.* **380**, 49-51 (1996).

5. Zhang, Z., Zheng, W., Chen, A., Ding, K. & Huang, F. Crystal growth of  $\alpha$ -HgI<sub>2</sub> by the temperature difference method for high sensitivity x-ray detection. *Cryst. Growth Des.* **15**, 3383-3387 (2015).
6. Piechotra, M. Mercuric iodide for room temperature radiation detectors. Synthesis, purification, crystal growth and defect formation. *Mater. Sci. Eng.* **18**, 1-98 (1997).
7. McGregor, D. S. & Hermon, H. Room-temperature compound semiconductor radiation detectors. *Nucl. Instrum. Methods Phys. Res., Sec. A* **395**, 101-124 (1997).
8. Owens, A. & Peacock, A. Compound semiconductor radiation detectors. *Nucl. Instrum. Methods Phys. Res., Sect. A* **531**, 18-37 (2004).
9. Stoumpos, C. C. et al. Crystal growth of the perovskite semiconductor CsPbBr<sub>3</sub>: a new material for high-energy radiation detection. *Cryst. Growth Des.* **13**, 2722-2727 (2013).
10. Kasap, S. et al. Amorphous and polycrystalline photoconductors for direct conversion flat panel X-ray image sensors. *Sensors* **11**, 5112-5157 (2011).
11. Sultana, A., Reznik, A., Karim, K. S. & Rowlands, J. A. Design and feasibility of active matrix flat panel detector using avalanche amorphous selenium for protein crystallography. *Med. Phys.* **35**, 4324-4332 (2008).
12. Yakunin, S. et al. Detection of X-ray photons by solution-processed lead halide perovskites. *Nat. Photon.* **9**, 444-449 (2015).
13. Simon, M. et al. Analysis of lead oxide (PbO) layers for direct conversion x-ray detection. *IEEE Trans. Nucl. Sci.* **52**, 2035-2040 (2005).

14. Simon, M. et al. PbO as direct conversion x-ray detector material. *Proc. SPIE* **5368**, 188-199 (2004).
15. Zhao, B. & Zhao, W. Temporal performance of amorphous selenium mammography detectors. *Med. Phys.* **32**, 128-136 (2005).
16. Abbaszadeh, S., Scott, C. C., Bubon, O., Reznik, A. & Karim, S. K. Enhanced detection efficiency of direct conversion x-ray detector using polyimide as hole-blocking layer. *Sci. Rep.* **3**, 3360 (2013).
17. Cho, S. et al. Effect of annealing on the x-ray detection properties of nano-sized polycrystalline lead oxide films. *Jpn. J. Appl. Phys.* **47**, 7393-7397 (2008).
18. Blevis, I. M., Hunt, D. C. & Rowlands, J. A. Measurement of x-ray photogeneration in amorphous selenium. *J. Appl. Phys.* **85**, 7958-7963 (1999).
19. Kang, Y. et al. Examination of PbI<sub>2</sub> and HgI<sub>2</sub> photoconductive materials for direct detection, active matrix, flat-panel imagers for diagnostic x-ray imaging. *IEEE Trans. Nucl. Sci.* **52**, 38-45 (2005).
20. Rowlands, J. A., Decrescenzo, G. & Araj, N. X-ray imaging using amorphous selenium: determination of x-ray sensitivity by pulse height spectroscopy. *Med. Phys.* **19**, 1065-1069 (1992).
21. Bertuccio, G. & Casiraghi, R. Study of silicon carbide for x-ray detection and spectroscopy. *IEEE Trans. Nucl. Sci.* **50**, 175-185 (2003).

22. Barnett, A. M., Lees, J.E., Bassforda, D.J. & Ng, J.S. Determination of the electron-hole pair creation energy in Al<sub>0.8</sub>Ga<sub>0.2</sub>As. *J. Inst.* **7**, P06016 (2012).
23. Bertuccio, G. & Maiocchi, D. Electron-hole pair generation energy in gallium arsenide by x and  $\gamma$  photons. *J. Appl. Phys.* **92**, 1248-1255 (2002).
24. Olschner, F., Lund, J.C. & Stern, I. Monte carlo simulation of gamma ray spectra from semiconductor detectors. *IEEE Trans. Nucl. Sci.* **36**, 1176-1179 (1989).
25. Barrett, H. H., Eskin, J.D. & Barber H. B. Charge transport in arrays of semiconductor gamma-ray detectors. *Phys. Rev. Lett.* **75**, 156-159 (1995).
26. Kim, K. O., Kwon, T. J. & Kim J. K. A new approach for evaluating the mobility-lifetime products of electron-hole pairs in semiconductor detectors. *J. Korean Phys. Soc.* **59**, 20-26 (2011).
27. Scannavini, M.G. et al. Computer simulation of charge trapping and ballistic deficit effects on gamma-ray spectra from CdTe semiconductor detectors. *Nucl. Instr. Meth. Phys. Res. A* **353**, 80-84 (1994).
28. Miyajima, S. & Imagawa, K. CdZnTe detector in diagnostic x-ray spectroscopy. *Med. Phys.* **29**, 1421-1429 (2002).
29. Akutagawa, W. & Zanio, K. Gamma response of semiinsulating material in the presence of trapping and detrapping. *J. Appl. Phys.* **40**, 3838-3854 (1969).
30. Semeniuk, O. et al. Transport of electrons in lead oxide studied by CELIV technique. *J. Phys. D: Appl. Phys.* **50**, 035103 (2017).

31. Semeniuk, O. et al. Charge transport mechanism in lead oxide revealed by CELIV technique. *Sci. Rep.* **6**, 33359 (2016).
32. Kabir, M. Z. & Kasap, S. O. Charge collection and absorption-limited sensitivity of x-ray photoconductors: Applications to a-Se and HgI<sub>2</sub>. *Appl. Phys. Lett.* **80**, 1664 (2002).
33. Zhao, W., Decrescenzo, G. & Rowlands J. A. Investigation of lag and ghosting in amorphous selenium flat-panel x-ray detectors. *Proc. SPIE* **4682**, 9-20 (2002).
34. Redus, B. Efficiency of Amptek XR-100T-CdTe and -CZT detectors. *Application Note ANCZT-1 Rev 2*. 1-8 (2002).
35. Kabir, M. Z. Effects of charge carrier trapping on polycrystalline PbO X-ray imaging detectors, *J. Appl. Phys.* **104**, 074506 (2008).
36. Scher, H. & Montroll, E. W. Anomalous transit-time dispersion in amorphous solids. *Phys. Rev. B* **12**, 2455-2477 (1975).
37. Pfister, G. & Scher, H. Dispersive (non-gaussian) transient transport in disordered solids. *Adv. Phys.* **27**, 747-798 (1978).
38. Nicholson, P.W. *Nuclear electronics* Ch. 6. (New York 1974).
39. Zhao, Q. et al. Performance evaluation of polycrystalline HgI<sub>2</sub> photoconductors for radiation therapy imaging. *Med. Phys.* **37**, 2738-2748 (2010).
40. Jiang, H., Zhao, Q., Antonuk, L. E., El-Mohri, Y. & Gupta, T. Development of active matrix flat panel imagers incorporating thin layers of polycrystalline HgI<sub>2</sub> for mammographic x-ray imaging. *Phys. Med. Biol.* **58**, 703-714 (2013).

41. Frisch, O. British Atomic Energy Report BR-49 (1944).
42. Wang, K. et al. Amorphous-selenium-based three-terminal x-ray detector with a gate. *IEEE Electron. Device Lett.* **32**, 782-784 (2011).
43. Mcgregor, D. S., He, Z., Seifert, H. A., Wehe, D. K. & Rojas, R. A. Single charge carrier type sensing with a parallel strip pseudo-Frisch-grid cdznte semiconductor radiation detector. *Appl. Phys. Lett.* **72**, 792-794 (1998).

### **Acknowledgement**

The authors are thankful to Dr. Matthias Simon from Philips Research Laboratories for active discussions on PbO. The authors gratefully acknowledge the financial support from the National Science and Engineering Research Council (NSERC), Canadian Institute for Health Research (CIHR) and Ontario Research Fund–Research Excellence (ORF-RE) program. This work was financially supported by the National Key Research and Development Program of China (Grant No. 2016YFA0202002). Support by Research Council of Lithuania (grant MIP-091/2015) is also acknowledged.

### **Author contributions**

O. S. prepared experimental PbO samples. O. S. and G. D. performed XPM and PHS experiments and drafted the manuscript text. O. G. performed CELIV measurements. G. J. and A. R. analyzed the obtained results and linked them with peculiarities of the charge transport in poly-PbO. K. W. and A. R. edited the manuscript text. All authors reviewed the manuscript.

### **Additional information**

There are no competing financial interests. There are no competing financial interests.

## 5.2. X-ray performance of a-PbO

This topic has been elaborated in the following publication: [O. Semeniuk](#), O. Grynko, G. Juska & A. Reznik “Investigation of X-ray performance of amorphous lead oxide (a-PbO) for application in direct conversion detectors”, submitted to *Scientific Reports*. The full text of the publication is listed below.

# **Amorphous lead oxide (a-PbO): suppression of signal lag via engineering of the layer structure**

O. Semeniuk<sup>1,2\*</sup>, O. Grynko<sup>1,2</sup>, A. Reznik<sup>2,3</sup>

1. Chemistry and materials science program, Lakehead University, 955 Oliver Road, Thunder Bay, ON, Canada P7B 5E1
2. Advanced detection devices department, Thunder Bay Regional Health Research Institute, 290 Munro Street, Thunder Bay, ON Canada P7A 7T1
3. Department of Physics, Lakehead University, 955 Oliver Road, Thunder Bay, ON, Canada P7B 5E1

\**e-mail*: [osemeniu@lakeheadu.ca](mailto:osemeniu@lakeheadu.ca) (O. Semeniuk).

## **Abstract**

Presence of a signal lag is a bottle neck of performance for many non-crystalline materials, considered for dynamic radiation sensing. Due to inadequate lag-related temporal performance polycrystalline layers of CdZnTe, PbI<sub>2</sub>, HgI<sub>2</sub> and PbO are not practically utilized, despite their superior X-ray sensitivity and low production cost (even for large area detectors). In the current manuscript, we show that a technological step to replace nonhomogeneous disorder in polycrystalline PbO with homogeneous amorphous PbO structure suppresses signal lag and improves time response to x-ray irradiation. In addition, the newly developed amorphous lead oxide (a-PbO) possesses superior X-ray sensitivity in terms of electron-hole pair creation energy  $W_{\pm}$  in comparison with amorphous selenium – currently the only photoconductor used as an X-ray-to-charge transducer in the state-of-the-art direct conversion x-ray medical imaging systems. The proposed advances of the deposition process are low cost, easy to implement and with certain customization might potentially be applied to other materials, thus paving the way to their wide-range commercial use.

## **Introduction**

Amorphous and polycrystalline modifications of wide band gap semiconductors are of paramount importance in modern electronics, since they allow large device area production at low cost. However, the transition from crystalline to non-crystalline materials is technologically challenging since structural disorder may lead to degradation of the material performance. A good example is CdTe and CdZnTe (CZT): the combination of outstanding photoconductive properties, and high atomic number of these materials made them widely employed in sensing electromagnetic radiation, particularly, in X-ray and gamma-ray detectors for a variety of applications ranging from

nuclear physics and astrophysics to homeland security and medical imaging [1-10]. However, polycrystalline forms of these materials are much less utilized. While the properties of poly-CdTe films are fit for optical photon harvesting in high efficiency solar cells [11-14], there are reported to be challenges for applications in X-ray medical imaging. Particularly, both poly-CdTe and poly-CdZnTe suffer from a residual signal after exposure termination, called signal lag [15-18]. The presence of residual a signal limits the application of these materials to static imaging (for instance, radiography), while the needs of vitally-important real-time imaging, like fluoroscopy, are left unmet. Interestingly, other polycrystalline high-Z (atomic number) materials that have also been considered for applications as radiation detectors (including polycrystalline layers of PbI<sub>2</sub>, HgI<sub>2</sub>, and PbO [19-23]) are all suffer from the same problem, i.e. signal lag. The values of the residual currents range from 10-30 % at 2-5 frame per second (fps) read-out in PbI<sub>2</sub> and HgI<sub>2</sub> [20,21,23] to 4-9 % at 1 fps in PbO [19], meaning that a significant fraction of the X-ray generated charge is collected after X-ray exposure is terminated. The similarity in X-ray response is correlated with a similarity in the layer structures: all these materials are highly inhomogeneous and are composed of grains which are 1-3  $\mu\text{m}$  in size for PbI<sub>2</sub> and PbO [19,20], and 30-60  $\mu\text{m}$  for high-quality HgI<sub>2</sub> layers [20]. It was suggested that the lag in these materials is caused by the presence of grain boundaries and associated defects which act as localized trapping sites for X-ray generated charge [20-23]. In addition, in poly-PbO lag is influenced by charge *injection* from the bias electrodes [19,24]. Indeed, it was shown that in poly-PbO the magnitude of lag depends on the material of the bias electrodes and is significantly suppressed for operation with electron beam-read out [25-27].

In terms of signal lag, the only exemption in the series of disordered materials considered for application in radiation sensing, is amorphous selenium (a-Se), where technological advances allowed suppression of image lag to a level that this material became a practical solution for

advanced direct conversion X-ray medical imaging detectors. Due to the comparatively low  $Z$  of a-Se, its properties are well suited to applications in so-called mammography energy range (20-30 keV). However, for general radiographic and fluoroscopic applications a-Se has to be replaced by a lag-free higher  $Z$  material. Interestingly, in contrast to the high- $Z$  polycrystalline materials mentioned above, a-Se has a *uniform* and homogeneous layer structure, composed of chains and rings of Se atoms [28] without grain boundaries. This suggests a possible approach to combat signal lag in disordered photoconductors, namely, to develop a grain boundary-free structure for lag-free operation.

In the current manuscript, we evaluate the image lag and x-ray sensitivity in newly developed homogeneous amorphous PbO structures. We show that elimination of the PbO polycrystalline structure has a very peculiar effect on the X-ray performance of PbO: signal lag was significantly improved, while X-ray sensitivity remains higher than reported for a-Se. The measurements performed at various exposures and at an extended range of electric fields suggests the suitability of a-PbO for real time imaging at 30 frames per second (fps).

## **Results**

### **Temporal behavior**

Fig. 1 shows the typical response of an a-PbO detector to a 4 s X-ray pulse. The amplitude of the signal remains constant during the exposure, while after termination of X-rays it promptly drops to the dark current level. As seen from Fig. 1, our result compares favorably with previously reported data on polycrystalline PbO, which exhibits a signal build up during exposure and a relatively long lag for similar pulse duration [19].

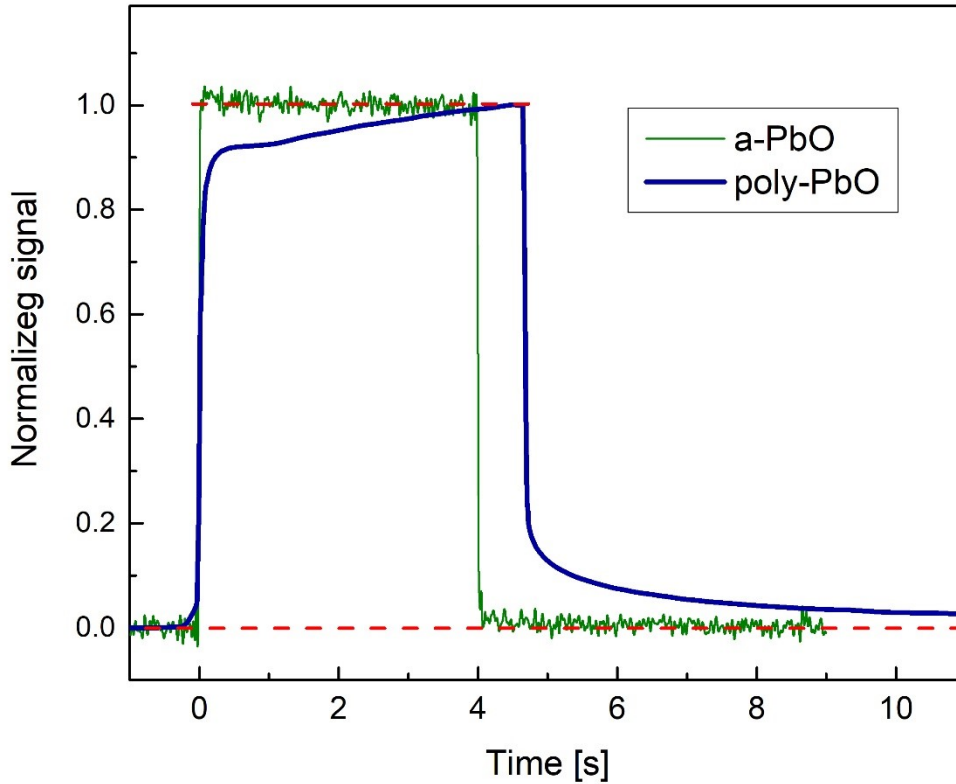


Figure 1. Response of a-PbO at  $F = 10 \text{ V}/\mu\text{m}$  to a 4 s X-ray exposure. The X-ray signal was offset corrected for the dark current. For this purpose, the average of data points before exposure was subtracted from the X-ray trace of a-PbO.

Fig. 2 shows signal lag of a-PbO detector measured for various experimental conditions, relevant to those used in pulsed fluoroscopy. For this purpose, the detector was exposed to short (4 ms and 10 ms) X-ray pulses and an X-ray response was readout every 33 ms (i.e. at 30 fps) [29-30]. The lag was determined as the ratio of the residual signal after exposure to the X-ray signal value. As seen from Fig. 2, signal lag of a-PbO increases with exposure duration, which was previously observed in other materials, like a-Se and poly-PbO [30; 31]. Thus, the first frame lag of a-PbO

was found to be 0.4 % and 1.4 % after single X-ray pulses of 4 ms and 10 ms, respectively. The lag dropped to undetectable values after the first frame for the shortest pulse duration (4 ms) and after the second frame for 10 ms pulse. While the data obtained compares favorably with lag measured in a-Se detectors of 1.5% and 3.7% for same pulse durations [29,32,33], it is also important to check the residual signal under longer exposures, which are more relevant to fluoroscopic imaging. To simulate such conditions, a-PbO detector was subjected to extended exposures of 100 ms, 1 s and 4 s. The corresponding values for the first frame lag are: 3.2 %, 4.1 % and 4.7 %, respectively. The obtained values are also comparable with those measured on a-Se direct conversion and CsI indirect conversion detectors, which normally exhibit the first frame lag values less than 10 % and 5 %, respectively [30,31,34-36]. It should be noted that lag in these detectors was measured in the pulsed fluoroscopy mode, i.e. with sequence of short exposures 1-8 ms every 33 ms so that detector material has time to “rest” and recover between exposures. Nevertheless, as this is seen from Fig. 2, with the subsequent frames the lag quickly drops even for long exposures; it is no longer detected after the fourth frame for 100 ms pulse duration and after the eighth frame for 1s pulse. For the longest pulse of 2 s the lag is still at ~2% after eight frames, although this long pulse of X-rays represents extreme operation conditions with extra load on the detector.

Fig. 3 illustrates normalized response of a-PbO to 100 ms exposures measured at selected electric fields. Residual signal is shown to be scalable with applied electric field, i.e. no lag improvement is observed at higher fields.

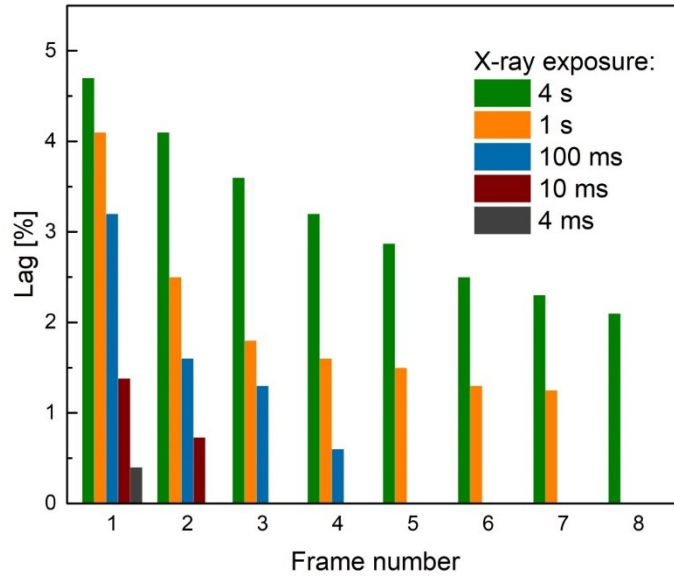


Figure 2. The lag measured at read-out rate of 30 fps in a-PbO at 10 V/ $\mu\text{m}$  is shown for different X-ray pulses.

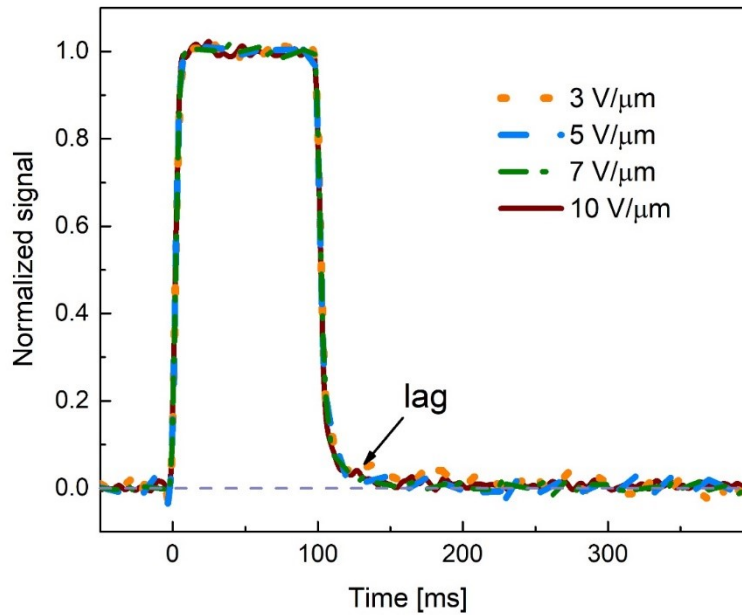


Figure 3. The normalized response of a-PbO to 100 ms X-ray pulse.

## X-ray sensitivity

The sensitivity of a-PbO to X-rays is characterized in terms of energy, required for creation of a single electron-hole pair  $W_{\pm}$ . This quantity was derived from the total charge collected with a-PbO detector upon X-ray exposure. More details on this analysis can be found elsewhere [19,24,37]. The measurements of X-ray response of a-PbO performed at different electric fields  $F$  show that  $W_{\pm}$  decreases with  $F$  as shown in Fig. 4, reaching the value of 22 eV/ehp and 18 eV/ehp at 10 V/ $\mu\text{m}$  and 20 V/ $\mu\text{m}$ , respectively. The measurements performed at 100 ms and 1s X-ray pulses provide essentially the same values within  $\sim 3\%$ . Plotting  $W_{\pm}$  as a function of inverse field and extrapolating it to the infinite field reveals saturation at  $\sim 14$  eV/ehp (see inset to Fig. 4).

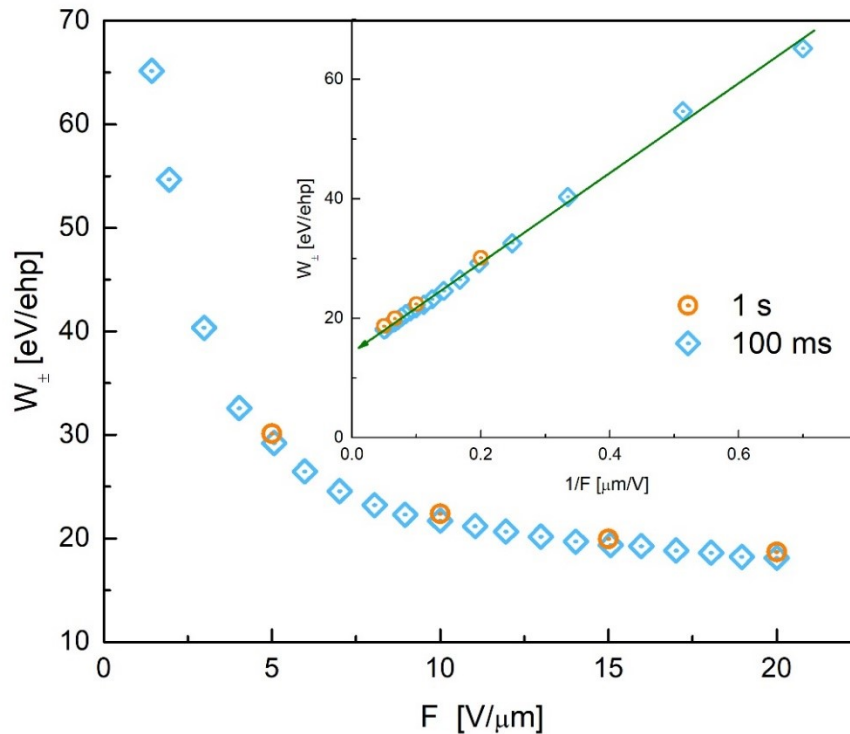


Figure 4. Measured values of  $W_{\pm}$  are plotted as a function of  $F$ . The inset to the figure shows  $W_{\pm}$  plotted as a function of  $1/F$ .

## Discussion

If a photoconductor is considered for applications in real-time i.e. fluoroscopic, imaging, its temporal performance (in terms of the signal rise time under x-ray exposure and the signal fall time once the exposure is terminated) is of particular importance. Indeed, fluoroscopic imaging is the most challenging and demanding radiation medical procedure, since the detector is exposed to very short, 2-4 ms (sometimes, 1-10 ms), X-ray pulses at  $\sim 70$  kVp, while the image acquisition rate is very fast: 30 frames per second (fps) [29,36,38]. Such dynamic read out is needed to capture the motion of the human structures and requires very little residual signal at the end of each frame, otherwise the previous image will be superimposed on the subsequent ones, resulting in a misleading view. Therefore, a quasi-rectangular shape of x-ray generated current and the absence of lag are important figures of merit to evaluate the readiness of an X-ray-to-charge transducer for direct conversion X-ray medical imaging detectors. Figs. 1 and 2 demonstrate the significant signal lag suppression in amorphous PbO in comparison with its polycrystalline form: for the most relevant to fluoroscopic procedures pulse duration of 4 ms, the first frame lag was as small as 0.4 % and was undetectable after the second frame. Even for the extended exposures the observed lag never exceeded 5 %, thus making the temporal performance of a-PbO comparable with CsI detectors, which are currently in use for fluoroscopic applications.

When it is detectable, the lag in a-PbO has an interesting behavior: it depends on the exposure duration, and is scalable with the applied electric field (see Figs. 2,3). Similar behavior was observed on a-Se layers and was related to electronic processes at the bias electrode interfaces, which facilitate injection [30]. The analogy with a-Se suggests injection as the primary cause for lag in a-PbO. Such injection builds-up during exposure [39,40] and interferes with X-ray sensitivity measurements, and misleadingly reducing  $W_{\pm}$  values at longer X-ray pulse durations [24].

However,  $W_{\pm}$  measurements performed on a-PbO (see Fig. 4) remain within 3% of the measured values with increase in pulse duration by a factor of 10, indicating an insignificant contribution of X-ray-modulated injection on  $W_{\pm}$  measurements in a-PbO. The obtained  $W_{\pm}$  values compare very favourably with those reported for a-Se: at  $F = 10 \text{ V}/\mu\text{m}$ ,  $W_{\pm}$  of a-PbO is  $\sim 22 \text{ eV}/\text{ehp}$ , which is about a half the a-Se value, measured at the same electric field [41].

Overall, our findings suggest an interesting and non-obvious approach to the improvement of X-ray response: replace the spatial disorder of grain boundaries in polycrystalline films with uniform disorder in amorphous layers. Such a structural transformation facilitates significant lag improvement in PbO, while preserving its high X-ray sensitivity (i.e. low  $W_{\pm}$ ). In addition, the deposition process behind this structural transformation, also results in a stoichiometric layer, thus solving the issue of oxygen deficiency – a common problem of metal oxides.

Finally, we would like to note that the proposed low-cost optimization of the deposition process which was applied to PbO can potentially be applied (with certain customization of course) to other materials, like  $\text{PbI}_2$ ,  $\text{HgI}_2$  and CZT. Since, these materials possess the similar layer structure and suffer from similar artefacts, the advancement of the deposition process with ion bombardment and *amorphization* of the layer structure might also pave the way for many other photoconductors with practical application in commercial devices.

## Methods

The  $\sim 8 \mu\text{m}$  thick amorphous lead oxide (a-PbO) samples were grown by an ion assisted thermal evaporation technique. In this technique, high quality PbO powder (5N) was thermally evaporated at  $\sim 1000 \text{ }^\circ\text{C}$  on an ITO covered glass substrate. During the deposition process, the growing PbO layer undergoes a phase transition from polycrystalline to an amorphous structure as a result of

continuous bombardment of the growing layer with oxygen ions. The substrate temperature did not exceed 100-150 °C, as indicated by temperature labels installed on the back of the substrate. The details of the evaporation process can be found in Ref. [42]. Scanning electron microscopy (SEM) measurements show that the a-PbO grows as highly packed layer, while energy dispersive X-ray spectroscopy (EDS) indicates a uniform distribution of lead and oxygen atoms in the sample (see Fig. 5). For electrical measurements, a gold contact (1 mm in diameter) was sputtered *ex-situ* atop the a-PbO film in a dedicated chamber.

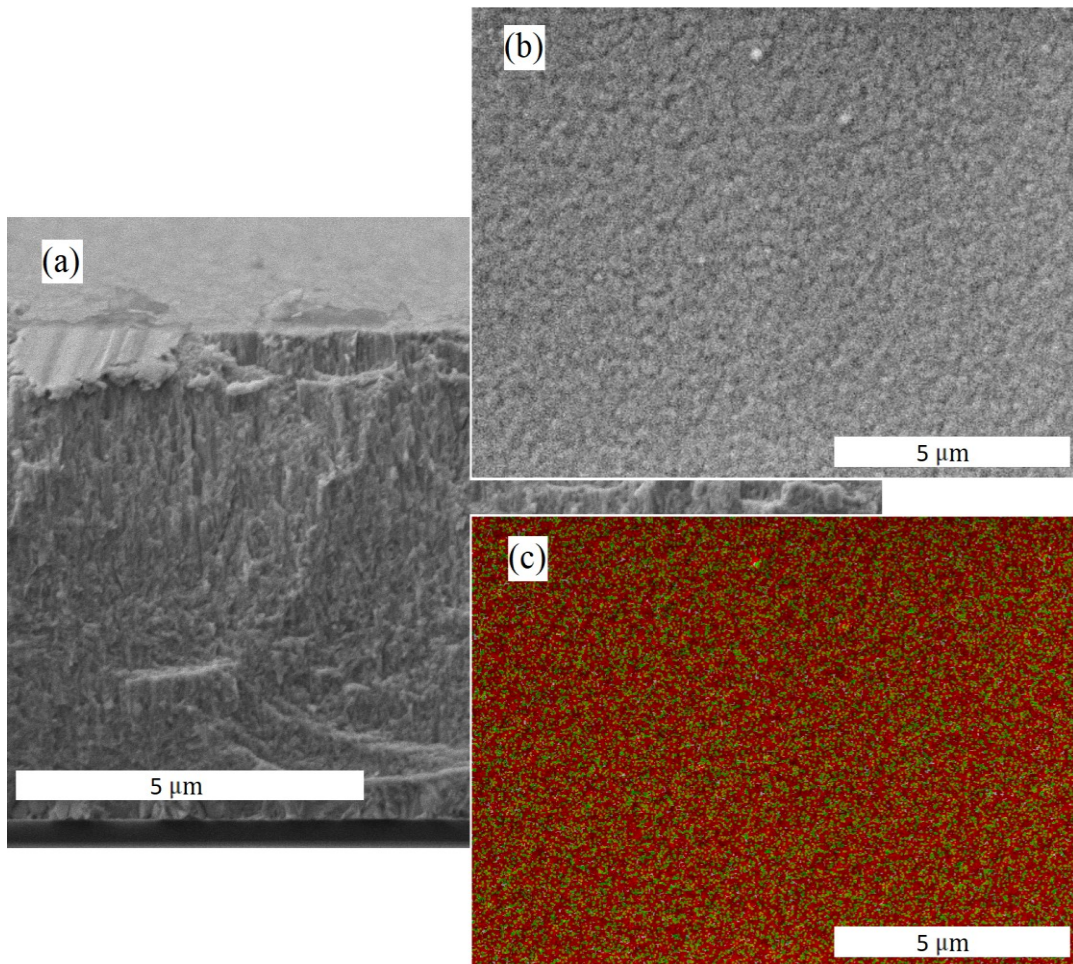


Figure 5. Morphological analysis of a-PbO samples: (a) SEM of a-PbO cross-section; (b) SEM micrograph of the a-PbO surface; (c) EDS of the surface. Red color represents Pb atoms and green color is for oxygen. It should be noted that the signal from Pb is stronger than that from O (typical for EDS measurements), therefore picture looks more red, while material is perfectly stoichiometric [42].

Fig. 6 shows the typical experimental apparatus for of X-ray performance evaluation. The X-ray tube model PX1412CS operated at 60 kVp was used to generate X-ray pulses of various duration ranging from 4 ms to 4 seconds. A 1.5 mm thick aluminum plate was used to cut off the low energy X-rays from entering the detector. The exposure to a-PbO layers was monitored with a Keithley model 96035 ionization chamber, which showed from 17 mR to 17 R exposure depending on X-ray pulse duration. A lead collimator 2 mm thick was used to minimize stray scattering. The model PS350 Stanford Research Systems power supply provided a constant electric field applied to the sample. During all experiments, a positive polarity was applied to the ITO. The X-ray response of the a-PbO detector was observed on the 1 MOhm input of a model TDS 420 Tektronix oscilloscope. The dark current measurements were performed with a Keithley model 35617EBS electrometer.

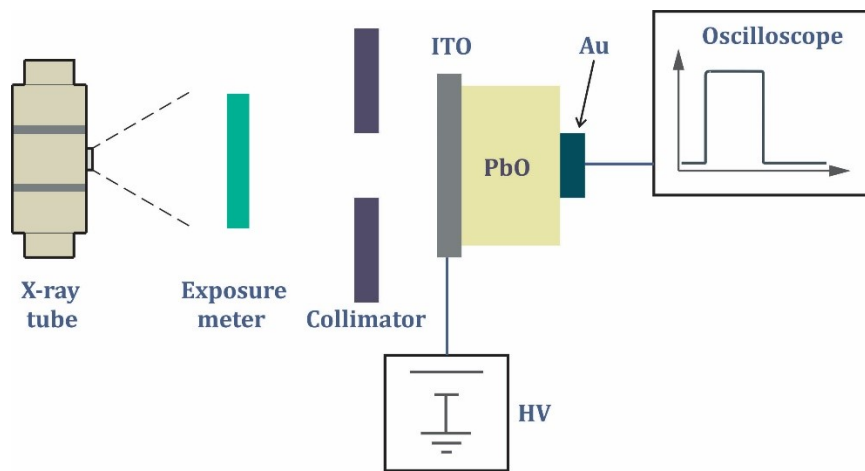


Figure 6. Schematic diagram of experimental apparatus for X-ray performance evaluation.

## References

1. Zhou, B. et al. Studies on the deep-level defects in CdZnTe crystals grown by travelling heater method. *Phys. Status Solidi A*. **214**, 1600748 (2017).

2. Roy, U. N. et al. Novel ZnO:Al contacts to CdZnTe for X- and gamma-ray detectors. *Sci. Rep.* **6**, 26384 (2016).
3. Zhang, Z. et al. A novel approach of chemical mechanical polishing for cadmium zinc telluride wafers. *Sci. Rep.* **6**, 26891 (2016).
4. Takahashi, T. & Watanabe, S. Recent progress in CdTe and CdZnTe detectors. *IEEE Trans. Nucl. Sci.* **48**, 950-959 (2001).
5. Eisen, Y. & Shor, A. CdTe and CdZnTe materials for room-temperature X-ray and gamma ray detectors. *J. Cryst. Growth.* **184**, 1302-1312 (1998).
6. Schlesinger, T. E. et al. Cadmium zinc telluride and its use as a nuclear radiation detector material. *Mater. Sci. Eng. R Rep.* **32**, 103-189 (2001).
7. Szeles, C. CdZnTe and CdTe materials for X-ray and gamma ray radiation detector applications. *Phys. Status Solidi.* **241**, 783–790 (2004).
8. Aamir, R. et al. Pixel sensitivity variations in a CdTe-Medipix2 detector using poly-energetic X-rays. *J. Instrum.* **6**, 1-8 (2011).
9. Zwerger, A., Fauler, A., Fiederle, M. & Jakobs, K. Medipix2: Processing and measurements of GaAs pixel detectors. 2007, *Nucl. Instrum. Meth. A.* **576**, 23 (2007).
10. Del Sordo, S. et al. Progress in the development of CdTe and CdZnTe semiconductor radiation detectors for astrophysical and medical applications. *Sensors.* **9**, 3491-3526 (2009).
11. Major, J. D., Treharne, R. E., Phillips, L. J. & Durose, K. A low-cost non-toxic post-growth activation step for CdTe solar cells., *Nat.* **511**, 334-337 (2014).
12. Zhao, Y. et al. Monocrystalline CdTe solar cells with open-circuit voltage over 1 V and efficiency of 17%. *Nat. Energy.* **1**, 16067 (2016).

13. Visoly-Fisher, I., Cohen, S. R., Ruzin, A. & Cahen, D. How polycrystalline devices can outperform single-crystal ones: thin film CdTe/CdS solar cells. *Adv. Mater.* **16**, 879–883 (2004).
14. Alberi, K. et al. Measuring long-range carrier diffusion across multiple grains in polycrystalline semiconductors by photoluminescence imaging. *Nat. Commun.* **4**, 2699 (2013).
15. Yin, S. et al. Direct conversion CdZnTe and CdTe detectors for digital mammography. *IEEE Nucl. Sci. Symp. Conf. Rec.* **7098962**, 23-6-10 (2001).
16. Arques, M. et al. Dynamic X-ray direct conversion detector using a CdTe polycrystalline layer. 2011, *Nucl. Instr. Meth. Phys. Res. Sec. A* **633**, S55–S58 (2011).
17. Sunwoo, Y., Park, S.-W. & Yi, Y. Polycrystalline CdZnTe thick films for low energy X-ray: system evaluation. *IEEE Proc.* **9219896**, 1990-1993 (2006).
18. Tokuda, S., Kishihara, H., Adachi, S. & Sato, T. Improvement of the temporal response and output uniformity of polycrystalline CdZnTe films for high-sensitivity X-ray imaging. *SPIE Proc.* **5030**, 861-870 (2003).
19. Simon, M. et al. Analysis of lead oxide (PbO) layers for direct conversion x-ray detection. *IEEE Trans. Nucl. Sci.* **52**, 2035-2040 (2005).
20. Street, R. A. et al. Comparison of PbI<sub>2</sub> and HgI<sub>2</sub> for direct detection active matrix X-ray image sensors. *J. Appl. Phys.* **91**, 3345-3355 (2002).
21. Du, H. et al. Investigation of the signal behavior at diagnostic energies of prototype, direct detection, active matrix, flat-panel imagers incorporating polycrystalline HgI<sub>2</sub>. *Phys. Med. Biol.* **53**, 1325-1351 (2008).
22. Simon, M. et al. PbO as direct conversion x-ray detector material. *Proc. SPIE* **5368**, 188-199 (2004).

23. Zhao, Q. et al. Performance evaluation of polycrystalline HgI<sub>2</sub> photoconductors for radiation therapy imaging. *Med. Phys.* **37**, 2738-2748 (2010).
24. Semeniuk, O. et al. Characterization of polycrystalline lead oxide for application in direct conversion X-ray detectors. Submitted to *Sci. Rep.*
25. L. Heijne, L., Schagen, P. & Bruining, H. Television pick-up tube for both light and X-Ray pictures. *Nat.* **173**, 220 (1954).
26. Haan, E. F., Van der Drift, A. & Schampers, P. P. M. The “Plumbicon”, a new television camera tube. *Philips Tech. Rev.* **25**, 133-180 (1964).
27. Biberman, L. M. & Nudelman, S. *Photoelectronic imaging devices* Vol. 2 (eds Stupp, E. H., Levitt, R. S.) Ch. 14, 275-300 (Plenum, 1971).
28. Reyes-Retana, J. A. & Valladares, A. A. Structural properties of amorphous selenium: An ab initio molecular-dynamics simulation. *Comput. Mater. Sci.* **47**, 934–939 (2010).
29. Tsukamoto, A. et al. Development and evaluation of a large-area selenium-based flat-panel detector for real-time radiography and fluoroscopy. *Proc. SPIE.* **3659**, 14-23 (1999).
30. Tousignant, O. et al. Spatial and temporal image characteristics of real time large area a-Se X-ray detector. *Proc. SPIE.* **5745**, 207-215 (2005).
31. Siewerdsen, J. H., Cunningham, I. A. & Jaffray, D. A. A framework for noise-power spectrum analysis of multidimensional images. *Med. Phys.* **29**, 2655 (2002).
32. Tsukamoto, A et al. Development of a selenium-based flat-panel detector for real-time radiography and fluoroscopy. *Proc. SPIE.* **3336**, 388-395 (1998).
33. Adachi, S. et al. Experimental evaluation of a-Se and CdTe flat-panel x-ray detectors for digital radiography and fluoroscopy. *Proc. SPIE.* **3977**, 38-47 (2000).

34. Granfors, P. R. et al. Performance of a 41×41 cm<sup>2</sup> amorphous silicon flat panel X-ray detector designed for angiographic and R&F imaging applications. *Med. Phys.* **30**, 2715 (2003).
35. Granfors, P. R. et al. Performance of a flat panel cardiac detector. 2001, *Proc. SPIE.* **4320**, 77-86 (2001).
36. Hunt, D. C., Tuosignant, O. & Rowlands, J. A. Evaluation of the imaging properties of an amorphous selenium-based flat panel detector for digital fluoroscopy. *Med. Phys.* **31**, 1166-1175 (2004).
37. Haugen, C. & Kasap, S. O. Langevin recombination of drifting electrons and holes in stabilized a-Se (Cl-doped a-Se: 0.3% As). *Philos. Mag. B.* **71**, 91-96 (1995).
38. Kasap, S. & Rowlands, J. A. Direct-conversion flat-panel X-ray image sensors for digital radiography. *Proc. IEEE.* **90**, 591-604 (2002).
39. Zhao, B. & Zhao, W. Temporal performance of amorphous selenium mammography detectors. *Med. Phys.* **32**, 128-136 (2005).
40. Abbaszadeh, S., Scott, C. C., Bubon, O., Reznik, A. & Karim, S. K. Enhanced detection efficiency of direct conversion x-ray detector using polyimide as hole-blocking layer. *Sci. Rep.* **3**, 3360 (2013).
41. Kasap, S. et al. Amorphous selenium and its alloys from early xeroradiography to high resolution X-ray image detectors and ultrasensitive imaging tubes. *Phys. Status Solidi B.* **246**, 1794–1805 (2009).
42. Semeniuk, O., Csik, A., Kokenyesi, S. & Reznik, A. Ion-assisted deposition of amorphous PbO layers. *J. Mater. Sci.* **52**, 7937-7946 (2017).

## Acknowledgement

The authors are thankful to Dr. Guosheng Wu from Lakehead University for help with SEM and EDS measurements. Also, the authors gratefully acknowledge the financial support from the National Science and Engineering Research Council (NSERC), Canadian Institute for Health Research (CIHR) and Ontario Research Fund–Research Excellence (ORF-RE) program.

### **Author contributions**

O. S. developed the deposition procedure, prepared the a-PbO samples and drafted the manuscript text. O. S. and O. G. the performed experiments. O. G. and A. R. edited manuscript. A. R. examined the obtained results and related them to modifications of the layer structure. All authors reviewed the manuscript.

### **Additional information**

There are no competing financial interests.

# Chapter 6: Conclusions and future work

## 6.1. Conclusions

The focus of this work is to investigate the properties of PbO for applications as direct X-ray-to-charge transducers in medical imaging detectors. For this purpose, comprehensive material science research on different polymorphic forms of the material were performed to provide solid information on their structural and electro-optical properties and X-ray performance. The PbO samples were prepared with conventional thermal deposition and newly developed ion assisted deposition technique.

Structural investigation of PbO layers with XRD and Raman spectroscopy indicates that while basic thermal evaporation results in a polycrystalline structure (poly-PbO), oxygen ion bombardment of the growing layer can provide a new polymorphic form, namely, amorphous Lead Oxide (a-PbO), not synthesized before. In contrast to poly-PbO, a-PbO is uniform, free of voids and does not require special storage conditions to prevent structural degradation. In addition, morphological analysis of PbO layers performed with SEM indicates that the novel a-PbO layers possess a significantly higher packing density, in comparison to poly-PbO. The improved density and the absence of voids in the layer offer a high bulk X-ray stopping power – one of the main advantages of PbO for direct conversion X-ray detectors. Amorphous PbO is stable at ambient conditions and undergoes gradual crystallization toward orthorhombic PbO only at elevated temperatures. This property is expected, since amorphous state is fundamentally metastable with respect to the crystalline structure. Compositional analysis with XPS reveals that perfect stoichiometry of the a-PbO layers is maintained through the layer. This is an important advantage over poly-PbO, which is over-oxidized at the surface and oxygen deficient in the bulk. Such oxygen deficiency and suboptimal stoichiometry are common problems in all metal oxides grown using

conventional deposition in an atmosphere of neutral oxygen. Indeed, electrically neutral oxygen molecules do not react deliberately with other elements. The utilization of an ion source to disturb this charge neutrality makes the oxygen more reactive and provides a natural low-cost solution to oxygen deficiency, layer porosity and stability problems.

In addition, the advances in the deposition process combats the major obstacle of PbO for applications in real-time large-area imaging detectors – signal lag. Optimization of the ion-assisted deposition technique permitted the growth of a-PbO layers with essentially no lag and represents a breakthrough in PbO technology, and for direct conversion X-ray detectors in general. Indeed, signal lag was suppressed to values achieved only with CsI indirect conversion detectors, which have a number of disadvantages inherent to the indirect conversion scheme. The evaluation of the transport and X-ray properties of both poly- and a-PbO layers allow us to conclude that lag elimination is due to suppressed injection in a-PbO, resulting in superior temporal performance of amorphous lead oxide over its polycrystalline counterpart.

The X-ray sensitivity measurements with the X-ray photocurrent method showed that at an electric field  $F = 10 \text{ V}/\mu\text{m}$  an electron-hole creation energy  $W_{\pm}$  of a-PbO is  $\sim 22 \text{ eV}/\text{ehp}$ . Such a value is superior to CsI detectors and about a half the a-Se value, which is currently the only wide-bandgap photoconductor used commercially in the direct conversion detectors for low X-ray energy clinical applications (i.e., in x-ray mammography). The  $W_{\pm}$  values obtained on a-PbO are in a good agreement to those measured on the polycrystalline material, when corrected for charge injection. This is a very peculiar finding since it suggests that X-ray charge generation processes in both materials are similar despite pronounced differences in the crystal structure.

Overall, with ion assisted deposition, PbO becomes the first and currently the only high-Z material that can be directly deposited onto a large area detector imager array and possesses

appropriate temporal performance (in terms of lag) for real time imaging applications. It should be noted that the proposed low-cost modifications of the deposition process applied here to improve PbO performance can potentially be applied to other materials (polycrystalline layers of Cd(Zn)Te, HgI<sub>2</sub>, PbI<sub>2</sub>), which currently suffer from similar problems as polycrystalline PbO (suboptimal packing density, signal lag, etc). Thus, application of ion assisted deposition has the potential to pave the way for many prospective materials with practical application in commercial devices.

## **6.2. Future work**

### *6.2.1. Investigation of charge transport in a-PbO*

Transition from a more-ordered to a less-order crystal structure is traditionally accompanied with degradation of material performance, due to various defects developed at grain boundaries and the disorder of its electronic structure. While the transition from polycrystalline to amorphous structure of PbO layers did not result in degradation of its X-ray performance (rather improved it), it might affect the charge transport mechanism. Therefore, as a part of future work, the charge transport mechanism of a-PbO should be investigated in a similar fashion to poly-PbO reported in this study. Such investigation is especially important, considering that peculiarities of the layer structure which were shown to govern hole transport in poly-PbO. Indeed, while both carriers conduct electrical current in the dispersive regime, only the dispersion of electrons can be explained by energetic disorder typical of polycrystalline and amorphous structures. In contrast, dispersion of holes was related to spatial rather than energetic disorder (linked to the inhomogeneity of polycrystalline PbO layers) - an unusual result which has not been observed so far. Moreover, the inhomogeneous structure of the material reduced the recombination of photo-generated carriers, compared with the spatially homogeneous systems of a-Se and a-Si:H. The effect of homogeneity of the carrier recombination has to be further investigated. Transport and recombination

measurements are suggested to be performed with charge extraction by linearly increasing voltage (CELIV) technique, which was shown to be a reliable tool for characterization of disordered materials. Recent extension of the CELIV theoretical background to account for the dispersive nature of charge transport makes this technique a tool-of-choice for the investigation of charge transport in various non-crystalline media.

### *6.2.2. Reduction of the dark current*

The current challenge with a-PbO is the relatively high dark current (DC). The measurements, performed in the dark on the samples rested overnight after X-ray measurements, indicate that DC in a-PbO grows with applied field in a linear or exponential manner, depending on the sample. In addition, under a constant applied electric field, the DC was found to decrease over time, normally reaching  $\sim 120$  pA/mm<sup>2</sup> at 10 V/ $\mu$ m 30 s after application of the electric field. Although such a value of the dark current is lower than that reported for poly-PbO ( $\sim 250$  pA/mm<sup>2</sup> at 3.5 V/ $\mu$ m [1]), it is still higher than the upper limit for medical imaging applications ( $\sim 10$  pA/mm<sup>2</sup> [2]).

Reduction of the dark current is a complex task, which requires a comprehensive approach, (similar to that applied here to combat signal lag) focussed on: (1) finding the fundamental cause of the dark current; (2) develop the necessary technological solutions for DC improvement.

### *6.2.3. Development of a-PbO detector prototype*

Once dark current is successfully reduced, a detector prototype should be constructed and evaluated. For this purpose, a-PbO will be deposited over a TFT imager, used in conventional medical imaging detectors. As a first attempt, a limited size detector prototype of  $\sim 6 \times 6$  cm<sup>2</sup> is sufficient.

Evaluation of the imaging performance of a-PbO detector (rather than just a-PbO material) will be performed in terms of a modulation transfer function (MTF), noise power spectra (NPS) and detective quantum efficiency (DQE) [1,3]. These three parameters are the fundamental characteristics of any detector. Thus, MTF provides information on the spatial resolution of the detector and it is normally measured by masking part of the detector with slanted slit/edge target during uniform exposure of the detector. Spatial resolution is derived by mapping the signal on exposed and unexposed pixels under the target. NPS is measured at different X-ray exposures relevant for fluoroscopy, i.e. from 0.1  $\mu\text{R}$  up to 10  $\mu\text{R}$  per frame in order to establish the influence of system noise on the detector performance. Finally, DQE is calculated from the MTF and NPS and compared with theoretical predictions. DQE is probably the most important parameter of the detector, since it accounts for multiple factors (i.e. attenuation, charge yield, etc.) and provides global data on how efficiently the X-rays are used. The MTF, NPS and DQE data will be analyzed to determine the optimal detector thickness and applied electric field for practical applications and will be used for the development of a clinical detector prototype. For this purpose, a-PbO will be deposited over a large area cardio-size detector  $\sim 18 \times 18 \text{ cm}^2$  imaging active matrix plate, as was previously done for poly-PbO by Simon [1,3]. Qualitative image evaluation will be performed with a-PbO detector as a part of clinical system. We believe that novel a-PbO detector with low dark current, rapid response and high X-ray sensitivity will open a new page in radiographic and fluoroscopic X-ray detectors.

## References

1. Simon, M. et al. Analysis of lead oxide (PbO) layers for direct conversion X-ray detection. *IEEE Trans. Nucl. Sci.* **52**, 2035-2040 (2005).

2. Kasap, S. O. et al. Amorphous and polycrystalline photoconductors for direct conversion flat panel X-Ray image sensors. *Sensors* **11**, 5112-5157 (2010).
3. Simon, M. et al. PbO as direct conversion X-ray detector material. *Proc. SPIE* **5368**, 188-199 (2004).